Fakultät für Medizin

Cancer associated metabolic changes in tissues
studied by multimodal spatial *omics*

Thomas Kunzke

Vollständiger Abdruck der von der Fakultät für Medizin der Technischen Universität München zur Erlangung des akademischen Grades eines

Doktors der Naturwissenschaften (Dr. rer. nat.)

genehmigten Dissertation.

Vorsitz: Prof. Dr. Stefan Lichtenthaler

Prüfer*innen der Dissertation:

1. Prof. Dr. Gil G. Westmeyer

2. Prof. Dr. Bernd Reif

3. Prof. Dr. Dr. Matthias Kroiß

Die Dissertation wurde am 30.05.2022 bei der Technischen Universität München eingereicht und durch die Fakultät für Medizin am 21.02.2023 angenommen.

Abstract

Spatial metabolomics by mass spectrometry (MS) imaging has significantly improved the study of challenging biological systems like cancer tissues with unprecedented detail. Pathological conditions in tissues are inherently linked with the changed metabolome in the affected cells, which can be exclusively studied *in situ* by spatial metabolomics. However, there is often a need for a multimodal approach to detect affected cells using spatial metabolomics combined with other spatially resolved tissue modalities. Therefore, spatial metabolomics offers great potential to be improved multimodally to address unmet clinical needs in cancer therapy and provides new insights into the cancer metabolism of patients.

An improved method for multimodal spatial metabolomics was developed to access spatially resolved tissue data at different molecular layers. This improved method enabled the examination of the cancer metabolism in patient tissues locally at the primary site and systemically at distant organs to serve answers to unsolved clinical questions for patient diagnosis and targeted anti-cancer therapies.

This cumulative thesis proves the potential for multimodal spatial metabolomics in a clinical and preclinical setting by including four publications. Two publications reveal the methodological requirements for enabling multimodal spatial metabolomics. The subsequent publication describes the application of the method to improve the understanding of drivers of cancer pathophysiology and programmed cell death ligand-1 (PD-L1) expression. Finally, the last publication revealed the potential of the developed method for a systemic view of cancer metabolism in a preclinical setting.

The presented thesis makes a significant contribution to the applicability of spatial metabolomics in clinical diagnostics and preclinical research. The publications reveal the unexploited potential for using spatial metabolomics for clinical decision-making.

Contents

Contents

Appendix 99

Acknowledgments 103

List of Figures

List of Abbreviations

ACC	Acetyl coenzyme A carboxylase
AKT	Proteinkinase B
AMPK	Adenosine monophosphate-activated kinase
ATP	Adenosine triphosphate
CE-MS	Capillary electrophoresis-mass spectrometry
DCK	Deoxycytidine kinase
DNA	Deoxyribonucleic acid
ERK	Extracellular signal-regulated kinase
FAD	Flavin adenine dinucleotide
FT-ICR	Fourier transform ion cyclotron resonance
GC-MS	Gas chromatography-mass spectrometry
Grb2	Growth factor receptor-bound protein 2
HER2	Human epidermal growth factor receptor 2
IHC	Immunohistochemistry
iNOS	Inducible nitric oxide synthase
LC-MS	Liquid chromatography-mass spectrometry
MALDI	Matrix-assisted laser desorption/ionization
MAPK	Mitogen-activated protein kinase
MS	Mass spectrometry
NAD	Nicotinamide adenine dinucleotide
NGS	Next-generation sequencing
NMR	Nuclear magnetic resonance
NSCLC	Non-small-cell lung cancer
p53	Tumor suppressor protein 53
PD-1	Programmed cell death-1
PD-L1	Programmed cell death ligand-1
PI3K	Phosphoinositide 3-kinase
PKM2	Pyruvate kinase M2
PTEN	Phosphatase and tensin homolog

List of Abbreviations

RNA	Ribonucleic acid
ROI	Regions of interest
RRM1, RRM2	Ribonucleotide reductases
SAM	S-adenosylmethionine
Shc	Proto-oncogene tyrosine-protein kinase Src homology 2 domain containing transforming protein
SPACiAL	Spatial correlation image analysis
TK1	Thymidine kinase 1

1. Publication Record

This publication-based cumulative dissertation consists of the following peer-reviewed first-author publications:

IF = Impact Factor

1. Huber K*, **Kunzke T***, Buck A, Langer R, Luber B, Feuchtinger A, Walch A. Multimodal analysis of formalin-fixed and paraffin-embedded tissue by MALDI imaging and fluorescence *in situ* hybridization for combined genetic and metabolic analysis, *Lab Invest.* 2019, 99(10), 1535-1546.
   IF: 4.197 (2019)

2. Prade VM*, **Kunzke T***, Feuchtinger A, Rohm M, Luber B, Lordick F, Buck A, Walch A. *De novo* discovery of metabolic heterogeneity with immunophenotype-guided imaging mass spectrometry, *Mol. Metab.* 2020, 36, 100953.
   IF: 7.422 (2020)

3. **Kunzke T***, Prade VM*, Buck A, Sun N, Feuchtinger A, Matzka M, Fernandez IE, Wuyts W, Ackermann M, Jonigk D, Aichler M, Schmid RA, Eickelberg O, Berezowska A, Walch A. Patterns of carbon-bound exogenous compounds in patients with lung cancer and association with disease pathophysiology, *Cancer Res.* 2021, 81(23), 5862-5875.
   IF: 12.701 (2020)

4. **Kunzke T**, Buck A, Prade VM, Feuchtinger A, Prokopchuk O, Martignoni ME, Heisz S, Hauner H, Janssen KP, Walch A, Aichler M. Derangements of amino acids in cachectic skeletal muscle are caused by mitochondrial dysfunction, *J. Cachexia Sarcopenia Muscle* 2020, 11(1), 226-240.
   IF: 12.910 (2020)

   *) Authors contributed equally to this work.

1. Publication Record

Additional peer-reviewed first-author publications:

1. **Kunzke T**, Balluff B, Feuchtinger A, Buck A, Langer R, Luber B, Lordick F, Zitzelsberger H, Aichler M, Walch A. Native glycan fragments detected by MALDI-FT-ICR mass spectrometry imaging impact gastric cancer biology and patient outcome, *Oncotarget* 2017, 8(40), 68012-68025.
   IF: 5.168 (2016)

2. Sun N*, **Kunzke T***, Sbiera S, Kircher S, Feuchtinger A, Aichler M, Herterich S, Ronchi CL, Weigand I, Schlegel N, Waldmann J, Fragoso MCV, Whitsett TG, Gill AJ, Fassnacht M, Walch A, Kroiss M. Prognostic relevance of steroid sulfation in adrenocortical carcinoma revealed by molecular phenotyping using high resolution mass spectrometry imaging, *Clin Chem.* 2019. 65(10), 1276-1286.
   IF: 7.292 (2019)

3. **Kunzke T**, Hölzl FT, Prade VM, Buck A, Huber K, Feuchtinger A, Ebert K, Zwingenberger G, Geffers R, Hauck SM, Haffner I, Luber B, Lordick F, Walch A. Metabolomic therapy response prediction in pretherapeutic tissue biopsies for trastuzumab in patients with HER2-positive advanced gastric cancer, *Clin Transl Med.* 2021, 11(9), e547. (peer-reviewed letter to editor)
   IF: 11.492 (2020)

Publications as a co-author:

1. Aichler M, **Kunzke T**, Buck A, Sun N, Ackermann M, Jonigk D, Gaumann A, Walch A. Molecular similarities and differences from human pulmonary fibrosis and corresponding mouse model - MALDI imaging mass spectrometry in comparative medicine, *Lab Invest.* 2018, 98(1), 141-149.
   IF: 3.684 (2018)

2. Sun N, Wu Y, Nanba K, Sbiera S, Kircher S, **Kunzke T**, Aichler M, Berezowska S, Reibetanz J, Rainey WE, Fassnacht M, Walch A, Kroiss M. High resolution tissue mass spectrometry imaging reveals a refined functional anatomy of the human adult adrenal gland, *Endocrinology* 2018, 159(3), 1511-1524.
   IF: 3.800 (2018)

3. Murakami M*, Rhayem Y*, **Kunzke T**, Sun N, Feuchtinger A, Ludwig P, Strom TM, Gomez-Sanchez C, Knösel T, Kirchner T, Williams TA, Reincke M, Walch A, Beuschlein F. In situ metabolomics of aldosterone-producing adenomas, *JCI Insight* 2019, 4(17), e130356.
   IF: 6.205 (2019)

   *) Authors contributed equally to this work..

4. Ebert K, Mattes J, **Kunzke T**, Zwingenberger G, Luber B. MET as resistance factor for afatinib therapy and motility driver in gastric cancer cells, *PLoS One* 2019, 14(9), e0223225.
IF: 2.740 (2019)

5. Sun N, Meyer LS, Feuchtinger A, **Kunzke T**, Knösel T, Reincke M, Walch A, Williams TA. Mass spectrometry imaging establishes 2 distinct metabolic phenotypes of aldosterone-producing cell clusters in primary aldosteronism, *Hypertension* 2020, 75(3), 634-644.
IF: 10.190 (2020)

6. Blutke A, Sun N, Xu Z, Buck A, Harrison L, Schriever S, Pfluger PT, Wiles D, **Kunzke T**, Huber K, Schlegel J, Aichler M, Feuchtinger A, Matiasek K, Hauck SM, Walch A. Light sheet fluorescence microscopy guided MALDI-imaging mass spectrometry of cleared tissue samples, *Sci Rep.* 2020, 10(1), 14461.
IF: 4.379 (2020)

7. Heid I, Karakaya S, Münch C, Lueong SS, Winkelkotte AM, Liffers ST, Godfrey L, Cheung PFY, Savvatakis K, Topping GJ, Englert F, Kritzner L, Grashei M, **Kunzke T**, Sun N, Walch A, Tannapfel A, Viebahn R, Wolters H, Uhl W, Vangala D, Smeets EMM, Aarntzen EHJG, Rauh D, Hoheisel JD, Hellerschmied D, Hahn SA, Schilling F, Braren R, Trajkovic-Arsic M, Siveke JT. Functional metabolic phenotyping of human pancreatic ductal adenocarcinoma (not peer-reviewed, on pre-print server), *bioRxiv* 2021, doi: 10.1101/2021.07.23.452145

8. Sun N*, Trajkovic-Arsic M*, Li F*, Wu Y, Münch C, **Kunzke T**, Feuchtinger A, Steiger K, Schlitter AM, Weichert W, Esposito I, Siveke JT, Walch A. Native glycan fragments detected by MALDI Mass Spectrometry Imaging are independent prognostic factors in Pancreatic Ductal Adenocarcinoma, *EJNMMI Res.* 2021, 11(1), 120.
IF: 3.138 (2020)

9. Buck A*, Prade VM*, **Kunzke T**, Feuchtinger A, Kröll D, Feith M, Dislich B, Balluff B, Langer R, Walch A. Metabolic tumor constitution is superior to tumor regression grading for evaluating response to neoadjuvant therapy of esophageal adenocarcinoma patients, *J Pathol.* 2022, 256(2), 202-213.
IF: 7.996 (2020)

*) Authors contributed equally to this work.

10. Prade VM*, Sun N*, Shen J, Feuchtinger A, **Kunzke T**, Buck A, Schraml P, Moch H, Schwamborn K, Autenrieth M, Gschwend JE, Erlmeier F, Hartmann A, Walch A. The synergism of spatial metabolomics and morphometry improves machine learning-based renal tumour subtype classification, *Clin Transl Med.* 2022, 12(2), e666. (peer-reviewed letter to editor)
    IF: 11.492 (2020)

11. Sato S*, Dyar KA*, Treebak JT*, Jepsen SL, Ehrlich AM, Ashcroft SP, Trost K, **Kunzke T**, Prade VM, Small L, Basse AL, Schönke M, Chen S, Samad M, Baldi P, Barrès R, Walch A, Moritz T, Holst JJ, Lutter D, Zierath JR, Sassone-Corsi P. Atlas of Exercise Metabolism Reveals Time-Dependent Signatures of Metabolic Homeostasis, *Cell Metab.* 2022, 34(2), 329-345.
    IF: 27.287 (2020)

12. Wang Q*, Sun N*, **Kunzke T**, Buck A, Shen J, Prade VM, Stöckl B, Wang J, Feuchtinger A, Walch A. A simple preparation step to remove excess liquid lipids in white adipose tissue enabling improved detection of metabolites via MALDI-FTICR imaging MS, *Histochem Cell Biol.* 2022, 157(5), 595-605.
    IF: 4.3 (2020)

13. Wang J, **Kunzke T**, Prade VM, Shen J, Buck A, Feuchtinger A, Haffner I, Luber B, Liu DHW, Langer R, Lordick F, Sun N, Walch A. Spatial metabolomics identifies distinct tumor-specific subtypes in gastric cancer patients, *Clin Cancer Res.* 2022, (Online ahead of print).
    IF: 12.531 (2020)

14. Erlmeier F*, Sun N*, Shen J, Feuchtinger A, Buck A, Verena VM, **Kunzke T**, Schraml P, Moch H, Autenrieth M, Weichert W, Hartmann A, Walch A. MALDI Mass Spectrometry Imaging-Prognostic Pathways and Metabolites for Renal Cell Carcinomas, *Cancers (Basel)* 2022, 14(7), 1763.
    IF: 6.639 (2020)

15. Shen J*, Sun N*, Zens P, **Kunzke T**, Buck A, Prade VM, Wang J, Wang Q, Hu R, Feuchtinger A, Berezowska S, Walch A. Spatial metabolomics for evaluating response to neoadjuvant therapy in non-small cell lung cancer patients, *Cancer Commun (Lond)* 2022, 42(6), 517-535.
    IF: 10.392 (2020)

    *) Authors contributed equally to this work.

Patent applications:

1. Walch A, Huber K, Buck A, **Kunzke T**. IN-VITRO METHOD FOR DIAGNOSIS AND PROGNOSIS OF A DISEASE (2020), Luxemburg Patent Application LU101032, published 2020-06.

2. Walch A, Prade VM, **Kunzke T**, Buck A, Feuchtinger A. METHOD FOR AN AUTOMATIC, SEMANTIC-BASED, FUNCTIONAL TISSUE ANNOTATION OF HISTOLOGICAL AND CELLULAR FEATURES IN ORDER TO IDENTIFY MOLECULAR FEATURES IN TISSUE SAMPLES (2021), Luxemburg Patent Application LU101644, published 2021-08.

2. Introduction

The following chapter comprises two parts, a biological and technical introduction.

The first biological part introduces the reader to fundamental cancer-associated metabolic changes which play a role in the embedded publications [1, 2, 3, 4] (see chapter 3 - First Author Publications).

The second part of this chapter introduces the technical background of spatial metabolomics. With this, this thesis presents the topic of spatial metabolomics step-wise. Therefore, this thesis starts by introducing the commonly used bulk metabolomics, including essential definitions associated with metabolomic analysis. Subsequently, bulk metabolomics is compared with spatial metabolomics, and the advantages of using the spatially resolved metabolomics method are highlighted.

The end of the chapter includes the objectives of this thesis.

2.1. Cancer and metabolism

2.1.1. Metabolic changes in cancer tissues

Cancer development requires alterations in expression or mutations of genes, leading to deranged metabolism within cells [5]. Today, there is an increasing awareness that cancer is more of a metabolic than a genetic disease (Figure 1) [6]. Cellular metabolism is heavily affected by oncogenes and tumor suppressors [7]. Massive metabolic changes were described in cancer cells compared to non-cancerous cells [8]. Due to the enhanced proliferation rates in cancer cells, there is a need for elevated adenosine triphosphate (ATP) production and the continuous synthesis of building blocks such as amino acids, nucleic acids, and lipids [8]. Cancer cells are generally shifting from a catabolic to a more anabolic state [9]. Challenging aspects such as hypoxic environments, survival in circulation, and colonizing new metastatic niches are often followed by adapting the cancer cell metabolism [8]. The term "cancer metabolism" usually indicates a shared set of changed pathways in highly proliferative tumors or cancer cells [10].

2. Introduction

In the following, important changes in cancer metabolism are introduced, related to the embedded publications in this thesis [1, 2, 3, 4] (see chapter 3 - First Author Publications).
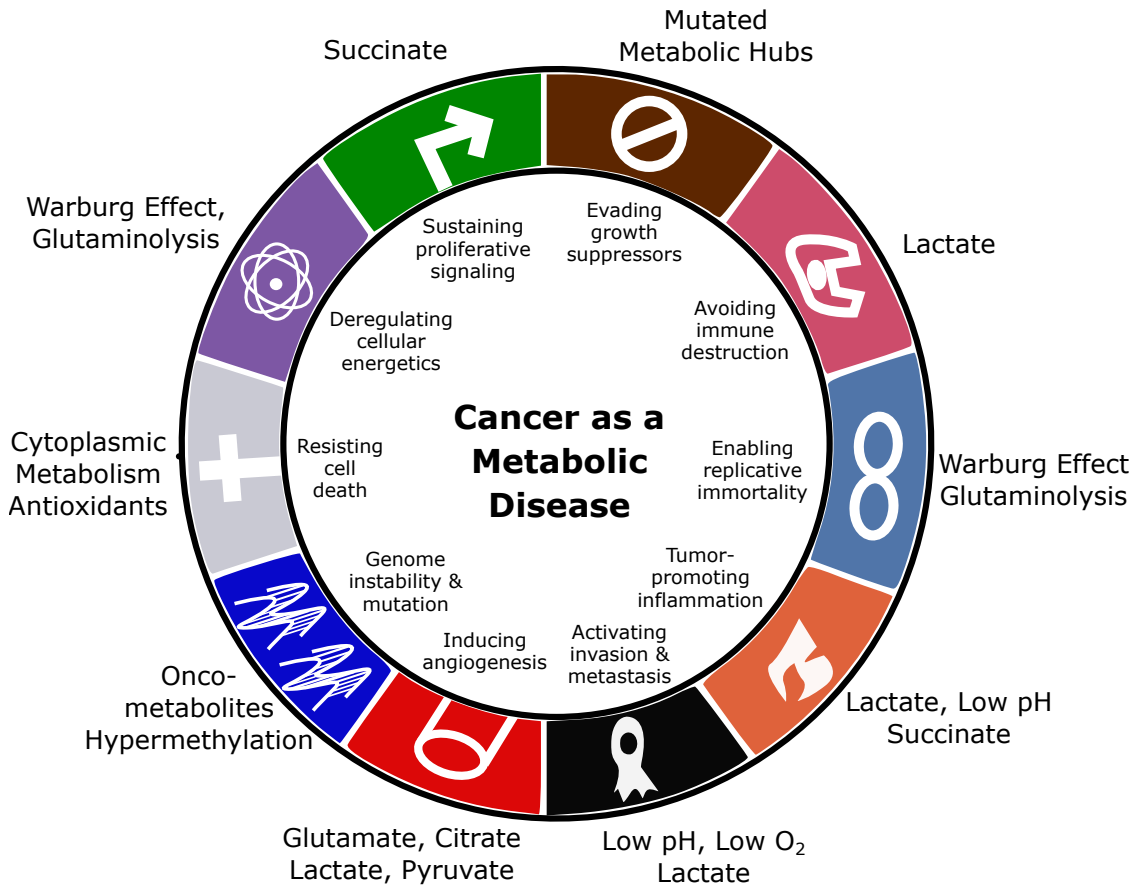

Figure 1. Cancer as a metabolic disease. A review of the Hallmarks of Cancer and the impact of a variety of metabolites or metabolic processes on each of these oncogenic features. The hallmarks are in the inner circle, while the corresponding metabolic processes or metabolites are outside of the circle. In accordance with [9]

Glycolysis

Glycolysis is the starting point in glucose metabolism and consists of nine reactions involving nine enzymes. Hexokinase, phosphofructokinase, and pyruvate kinase are rate-limiting and highly regulated enzymes, and all were revealed as altered in cancer [5, 11]. In addition, the uptake of glucose is increased in cancer by a factor of 200 [5, 12]. In non-cancer cells, the produced pyruvate from glucose by glycolysis enters the pyruvate dehydrogenase complex for the tricarboxylic acid cycle to be further oxidized to carbon dioxide [5]. During the steps of glycolysis and tricarboxylic acid cycle, oxidized nicotinamide adenine dinucleotide (NAD) is converted to reduced NAD and can be reoxidized in the oxygen-dependent electron transport chain to produce ATP. In

contrast, glucose in cancer cells feeds more the aerobic glycolysis for ATP production rather than oxidative phosphorylation, including the electron transport chain [8]. This is a central feature of a metabolic reprogramming of cancer cells, the Warburg effect (Figure 1). Cancer cells also reduce a much higher percentage of pyruvate to lactate to reoxidize NAD [5, 12]. Specific changes, such as the extracellular signal-regulated kinase (ERK) dependent phosphorylation of pyruvate kinase M2 (PKM2) and nuclear translocation of pSer37-PKM2 promote the Warburg effect [13]. The G protein-coupled receptor 55, among others, is modulating glycolysis by changing the translocation of pSer37-PKM2 [13]. In our publication [2], we investigated the possible metabolic fate of glucose depending on the spatial relationship to a protein targeted by trastuzumab therapy. A ligand of the G protein-coupled receptor 55 was revealed as a possible product of glucose depending on the spatial relationship to the targeted protein, which could be a driver of the Warburg effect (see chapter 3.2 for details). Furthermore, lactate dehydrogenase is an enzyme for reducing pyruvate to lactate and is often increased in cancer cells [14]. The secretion of lactate is also elevated in cancer cells, which is associated with an inhibited immune response (Figure 1) [15, 16].

Fatty acids

Just as glycolysis, fatty acids can also provide fuel to address the demanding resources for high proliferative cancer cells. On the one hand, fatty acid synthesis is described to be increased in cancer cells [17]. Hereby, the synthesis of fatty acids involves the repeated addition of two-carbon subunits [5]. Acetyl coenzyme A produced by ATP citrate lyase illustrates the starting point in this synthesis [5]. The first activation step of acetyl coenzyme A in the fatty acid synthesis is facilitated by the enzyme acetyl coenzyme A carboxylase (ACC) and is regulated by the cellular sensor of energy status adenosine monophosphate-activated kinase (AMPK) [18]. ACC is associated with a higher expression in multiple tumor types and is burdened with several tumorigenic mutations [18]. In our publication [1], we raised the question if ligand depending activation of AMPK is important for patient prognosis (see chapter 3.1 for details). The fatty acid synthesis is localized at the enzyme fatty acid synthase, which is also highly expressed in numerous cancers [5]. Previous studies revealed an association between fatty acid synthase and response to targeted cancer therapies such as trastuzumab in breast cancer [19]. The fatty acid synthase enzyme is able to synthesize 16-carbon long fatty acids, which can be further modified or elongated by additional enzymes [5]. The activation and appendix of coenzyme A to the synthesized fatty acid is facilitated by the acyl coenzyme A synthetase family, whereby some of these enzymes are reported as increased in certain cancer types [20]. On the other hand, fatty acid degradation is also changed in cancer cells. Beta-oxidation is a process that cleaves two carbons from fatty acids

until only acetyl coenzyme A remains. In each cleavage step, reduced NAD and reduced flavin adenine dinucleotide (FAD) are produced. Although cancer cells increase their lipid content, a lack of ATP can also enhance beta-oxidation [5]. In particular, cancer cells often increase their ATP content for developing metastasis [20, 21]. Our publication [3] indicates that in lung cancer, exogenous metabolites are co-drivers for cancer cell associated changes of the fatty acid profile (see chapter 3.3).

One carbon metabolism

"One carbon metabolism" is also essential for building up nucleotides, proteins, lipids and balancing redox potential through glutathione synthesis [9]. The pathway "one carbon metabolism" is often upregulated in cancer cells [22]. In our publication, we investigated the association of glutathione, a product of the "one carbon metabolism", with other metabolites in patients with lung cancer [3] (see chapter 3.3 for details). At all, this pathway focuses on the chemical reactions of folate compounds [5]. Folic acid belongs to the family of B vitamins and can be obtained from the diet or the production by the microbiome and will be reduced to synthesize tetrahydrofolate in cells [5]. One carbon derived from folic acid is transferred over several steps to homocysteine to produce S-adenosylmethionine (SAM) [5]. SAM is a crucial cosubstrate for methyl group transfers for modifying histones, nucleic acids, and phospholipids [23]. Therefore, SAM illustrates a fuel in cancer cells for several pathobiochemical reactions.

DNA and RNA synthesis

High proliferative cancer cells also require a sufficient supply of nucleotides to facilitate the increased demand for deoxyribonucleic acid (DNA) and ribonucleic acid (RNA) synthesis. Two basic pathways are available to produce nucleotides: salvage and *de novo* synthesis pathways [24]. The salvage pathway involves the recycling of existing nucleosides and nucleobases [24]. In contrast, the *de novo* synthesis builds up new nucleotides using amino acids and other small molecules [24]. Proliferative cells, such as cancer cells, use the *de novo* synthesis pathway more dominantly to produce nucleotides [25, 26]. Cytosolic and mitochondrial enzymes catalyze pyrimidine synthesis; in contrast, purine synthesis is localized in the cytoplasm [24]. The synthesized ribonucleoside triphosphates are further reduced to deoxyribonucleoside triphosphates by ribonucleotide reductases (RRM1, RRM2) for DNA synthesis [24]. The molecular changes driving *de novo* synthesis in cancer cells are not fully understood. One associated genetic modification is found for the tumor suppressor protein 53 (p53), as its mutated form was revealed to enhance RRM1, RRM2, deoxycytidine kinase (DCK), and thymidine kinase

1 (TK1) expression [27]. All of these enzymes are involved in nucleotide metabolism [24]. Interestingly, we found in all embedded publications [1, 2, 3, 4] associations between nucleotides and cancer biology.

Oncometabolites

From another point of view, metabolites can also trigger direct effects in cancer biology. Oncometabolites are endogenous metabolites that initiate or sustain tumorigenesis (Figure 1) [28, 9]. The past decades have unveiled several metabolites as oncogenic: fumarate, succinate, L-2-hydroxyglutarate, cystathionine, hypotaurine, sarcosine, and certain secondary bile acids [9]. It appears that these metabolites can modify hypermethylation, gene mutations, epigenetic changes, key signaling proteins, apoptosis, and induce metabolic reprogramming in cells [9]. Therefore, these metabolites can directly influence the fate of physiological cells to become cancer cells. Several oncometabolites were measured *in situ* in our publication [4] (see chapter 3.4).

However, finding general metabolic changes in cancer cells is challenging for several reasons. First, cancer cells depend mainly on the same metabolic pathways as the corresponding non-cancerous cell [10]. Only a few metabolic activities can clearly be assigned to cancer cell metabolism. Second, it becomes apparent that human tumors are metabolically heterogeneous, whereby cancer cells are metabolic different depending on their tissues of origin [29]. Even within the same solid tumor, the metabolic heterogeneity of cancer cells is apparent [29]. Third, metabolic changes are related to cancer progression. In more detail, cancer cells from metastatic tumors reveal another metabolic phenotype as cancer cells from preoplastic lesions [10]. After all, describing metabolic changes in cancer cells requires a more detailed view concerning cancer origin and cancer progression state. Advanced technologies are needed to overcome heterogeneity and detect metabolic changes sensitively.

2.1.2. Systemic metabolic changes - cancer cachexia

Metabolic changes are not limited to cancer tissues in cancer disease. In fact, cancer is a systemic disease and is associated with several metabolic changes in multiple tissues [30]. Cachexia, a multi-organ metabolic disorder, typically occurs in patients suffering from aggressive cancers such as gastrointestinal and lung cancer [31]. Eighty percent of patients with advanced cancer are suffering from cachexia [32]. Furthermore, cachexia is responsible for the death of at least 22 percent of individuals who have cancer [33].

2. Introduction

An international consensus defined cancer cachexia as

"a multi-factorial syndrome characterized by an ongoing loss of skeletal muscle mass, with or without a loss of fat mass, that cannot be fully reversed by conventional nutritional support and leads to progressive functional impairment". [34]

In a clinical setting, the definition for cancer cachexia diagnosis changed over time [35]. Most recently, an expert panel defined cancer cachexia diagnosis regarding three criteria. One criterion to diagnose a patient as cachectic is a weight loss >5 percent over the past 6 months in the absence of simple starvation. The second criterion for the diagnosis of cachexia includes patients revealing a body mass index <20 and a weight loss >2 percent. The last criterion for cachexia includes patients with an appendicular skeletal muscle index consistent with sarcopenia (males <7.26 kg/m^2; females <5.45 kg/m^2) and a weight loss >2 percent [34].

The treatment of cachexia is challenging because of the complexity of this multi-factorial metabolic disorder and the lack of definitive therapies [36]. Current therapies against cachexia are more related to palliation of symptoms instead of cure [37]. Nowadays, there exists no usual intervention for cancer cachexia, and some experts suggest that cachexia is refractory once established [38]. Considering the high complexity, experts recommend a multimodal intervention to treat cancer cachexia [38]. Nutritional therapies to increase energy and protein intake, drug therapies to stimulate appetite and decrease inflammation, and physical exercises are being developed to prevent cachexia [38].

Understanding why cachexia is occurring is an unmet need in cancer biology and medicine. Despite advanced-stage cancer disease, some patients maintain or gain weight and skeletal muscle mass [39, 40]. However, it is clear that cancer cachexia is driven by inflammatory processes triggered by the underlying cancer disease [31]. Possible triggers of cachexia are introduced in the literature. One study revealed that the presence of the primary tumor is a basic requirement for ongoing cancer cachexia [41]. The authors showed that removing the primary tumor can even reverse cachexia [41]. Specific humoral factors are involved in the maintenance of cachexia. Cachexia-associated humoral factors originate from tumor cells, non-tumor cells in the tumor microenvironment, or distant organs [32]. Evidence for humoral factors involved in cachexia is presented by a study in which the circulation of rats was surgically connected. In this experiment, pro-cachectic circulating factors could be transferred via circulation [42]. Pro- and anti-inflammatory cytokines, metal ions, hormones, and growth factors were highlighted as cachexia-associated humoral factors [32].

12

Muscle wasting and adipose tissue depletion mainly account for weight loss associated with cancer cachexia [31], whereby muscle wasting is the leading cause of functional impairment and death in cancer cachexia [31]. Compared to muscle wasting in cachexia, sarcopenia is an age-associated decrease of muscle mass, whereby muscle synthesis is hampered, but protein degradation is unchanged [36]. In cachexia, muscle wasting in patients influences anti-cancer treatment, survival outcomes, medical costs, and quality of life [43, 33]. For this reason, causes and important metabolic changes in cancer cachexia-associated muscle wasting are illuminated in the following sections.

Specific cachexia-associated biochemical changes in muscle cells are described in the literature. Being the primary site of protein storage in the body, one key fact of cachexia is that myofibrillar proteins are decreased in muscle tissues [44, 45]. Deranged metabolism in muscle cells is described as decreased protein synthesis, increased protein degradation, increased apoptosis, and changed amino acid metabolism [46]. One consequence of the before mentioned biochemical alterations in cachexia is a negative nitrogen balance in muscle cells [33]. Therefore, more nitrogen is excreted than ingested in cachectic skeletal muscle tissues. Protein loss in muscle cells is mainly mediated by ubiquitin-mediated proteasome degradation and calcium-activated protease calpains [47]. Pro-cachectic humoral factors were described to change lipolysis, proteolysis, glycolysis, and mitochondrial oxidative phosphorylation in muscle cells [48]. Precise molecular changes are responsible for muscle wasting. For example, a futile cycle between fructose 6-phosphate and fructose 1,6-biphosphate in myotubes was described [44]. This futile cycle is associated with a lower ATP level and muscle tissue wasting. In our publication [4], we showed for the first time *in situ* that the energy charge is significantly decreased in skeletal muscle tissues in cachexia (see chapter 3.4). Two possible mechanisms are responsible for triggering cachexia through circulating factors. First, humoral factors can directly enhance muscle cell catabolism or suppress protein synthesis by changing pathways [49, 50]. Second, the metabolism of other organs can be altered by humoral factors, which can also trigger muscle wasting [51].

Increased protein breakdown in cancer cachexia raises the question of the metabolic fate of released amino acids from proteins. The amino acid profile is changed in cachectic skeletal muscle tissues [52] and in the circulation of affected individuals [53]. Released amino acids can remain in muscle cells for other purposes instead of protein synthesis. It has been described that specific amino acids can be used to provide fuel for the citric acid cycle by cachectic skeletal muscle cells [52]. However, a significant part of the amino acids was released and recycled in other organs [54]. In our publication [4], we addressed the question of the fate of amino acids in cancer cachexia by analyzing *in situ* the

amino acid and protein content in skeletal muscle tissues simultaneously (see chapter 3.4).

Mitochondria play a prominent role in amino acid metabolism and general biochemical changes in cachectic skeletal muscle tissues; however, there is no consent regarding changes in mitochondrial content [53]. Mitochondrial density and size were unchanged in the study of Puig-Vilanova and colleagues regarding 18 patients [55]. Another study revealed a decrease in the number of mitochondria in skeletal muscle tissues by analyzing four patients [56]. In addition, the morphology of mitochondria was reported as changed in cachectic patients [57]. Animal models regarding cancer cachexia often provided complementary information. Multiple animal model based studies revealed evidence for mitochondrial dysfunction in cachectic skeletal muscle tissues [53]. In more detail, metabolic flux throughout the citric acid cycle and important enzyme complexes in the mitochondrial oxidative pathway are decreased [58, 53]. These biochemical changes are also associated with a lower ATP content in skeletal muscle cells and could play an important role in ongoing muscle wasting [53]. Our publication [4] revealed a linkage between mitochondrial dysfunction and altered amino acid metabolism in cancer cachexia (see chapter 3.4).

In conclusion, changes in protein synthesis/degradation and amino acid metabolism in skeletal muscle tissues are considered as crucial for the outcome of late-stage cancer patients. There is a need for a more comprehensive view provided by advanced *omics* technologies to investigate these changes and the reasons for these changes in more detail. Especially the multimodal combination of proteomics and metabolomics is of the highest interest in cancer cachexia since protein degradation and changed amino acid metabolism were reported as mainly altered in skeletal muscle tissues, and these molecular layers are inherently linked together. Until now, many aspects of the molecular fate of amino acids as building blocks in cancer cachexia are unclear. Therefore, advanced technologies are needed to provide a multimodal *omics* view of skeletal muscle tissues in cancer cachexia.

2.1.3. Cancer metabolism and therapy

In recent years, besides the in-depth study of cancer-associated metabolic changes, more attention was drawn to metabolic changes in response to anti-cancer therapies [59]. It will be an important insight if the cancer cell metabolism reflects the antitumoral effect of a treatment [59]. In addition, it would also be important if a metabolic constitution in cancer tissue before treatment is associated with anti-cancer therapy response. These insights could create the basis for new personalized therapeutic options and combination treatments [59]. Especially the interaction of host and cancer, mediated mainly by the immune system, is reflected in metabolites. The success of many anti-cancer therapies depends on the constitution of the host immune system [60]. The analysis

of metabolites following cancer drug administration has already provided important translational observations [61]. Therefore, metabolomics has a great potential to stratify patients into subgroups related to anti-cancer therapy response.

Metabolic reprogramming is already illustrating an important issue in chemotherapy resistance. Changes in glutamine metabolism were demonstrated as an influencing factor in gemcitabine treatment in pancreatic cancer [62]. In addition, alterations in amino acyltransfer RNA, glutathione metabolism, phenylalanine, tyrosine and tryptophan biosynthesis, and glycerophospholipid metabolism is associated with cisplatin resistance [63]. Van Gastel and colleagues reveal that residual acute myeloid leukemia cells exhibit transient metabolic adaptations that enable their survival after chemotherapy [64]. Chemotherapy persisting cells preferentially utilized glutamine, fueling pyrimidine and glutathione generation, but not the mitochondrial citric acid cycle. It can be assumed that changes in the cancer cell metabolism are also a crucial factor in targeted cancer therapies.

Targeted cancer therapies utilize the fact that cancer development and progression are driven by the accumulation of molecular features that allow cancer cells to survive, proliferate and evade immune surveillance, and promote their adaptability in a hostile environment [65]. The identification of molecular maps of cancers has led to the development of targeted cancer therapies that specifically inhibit the altered genes and signaling pathways that determine the malignant phenotype [65]. In particular, protein kinases can be targeted very sensitively by personalized medicine and play a prominent role in cell signaling. Inhibition of protein kinases is often relatively well tolerated by non-cancer cells [59].

The human epidermal growth factor receptor 2 (HER2) encoded by the *c-erbB2* proto-oncogene located on chromosome 17q21 illustrates an important example of a tyrosine kinase protein [66]. HER2 is often overexpressed in cancer, which is reflected by an aggressive phenotype and short patient survival [67]. HER2 belongs to the ErbB family of receptor tyrosine kinases along with three other members, including epithelial growth factor receptor, ErbB3, and ErbB4 [68]. Current data suggest that HER2 receptors form homo- and heteromers independent of ligand binding [68]. Subsequently, specific tyrosine residues in cytoplasmic domains are auto-phosphorylated or trans-phosphorylated to activate various intracellular signaling pathways [68]. After phosphorylation, several downstream effectors, such as growth factor receptor-bound protein 2 (Grb2) and proto-oncogene tyrosine-protein kinase Src homology 2 domain containing transforming protein (Shc), can bind to HER2 [68]. These effectors play an important role in regulating the mitogen-activated protein kinase (MAPK) signaling pathway [68]. Several metabolites are involved in the MAPK pathway and, therefore, this pathway is reflected in the

metabolome of cancer cells [69].

Trastuzumab, a monoclonal antibody targeted against the HER2 receptor, was developed. In 1989, trastuzumab was isolated from mice exposed to the HER2 receptor and later humanized [70, 71]. Several mechanisms have been proposed for the mode of action of trastuzumab; however, the mechanisms are still not fully understood [68]. Trastuzumab was revealed to inhibit HER2 heterodimerization, activate phosphorylation of HER2, inhibit MAPK / phosphoinositide 3-kinase (PI3K) / proteinkinase B (AKT) signaling pathways, inhibit the cell cycle, and activate antibody-dependent cell-mediated cytotoxicity [68].

From a clinical point of view, trastuzumab represents a crucial milestone in the therapy of HER2-positive breast cancer that profoundly altered the course of this disease [72]. Targeting HER2 by trastuzumab leads to a 40 percent improved overall survival in patients with HER2-positive breast cancer [59]. In addition, the treatment of patients with gastric cancer by trastuzumab revealed success. Trastuzumab in a combined therapy improves survival outcomes of patients with advanced HER2-positive gastric cancer [73].

To identify patients likely responding to trastuzumab, the analysis of pretherapeutic patient biopsies by immunohistochemical staining for the HER2 protein is state-of-the-art. Therefore, the quantity of the drug target HER2 is usually used to stratify patients into trastuzumab responders and non-responders. However, there is a clinical need for more accurate trastuzumab response classification in patients. A significant fraction of HER2-positive breast cancer patients has no benefit from trastuzumab treatment and relapse within 5 years [74, 75]. In addition, more than half of the patients with advanced gastric cancer are revealing no benefit from trastuzumab therapy despite having HER2 overexpressing tumors [76]. Other molecular biomarkers may reveal the great potential to tailor trastuzumab therapy to the individual patient in a more precise way [65]. A multimodal consideration combining different molecular layers in biomarkers may serve as a more accurate prediction.

Resistance mechanisms to trastuzumab may play an important role in these new molecular classification systems to stratify patients into trastuzumab responders and non-responders. So far, several mechanisms have been suggested to clarify how cancer cells are resistant to trastuzumab treatment. Activating mutations in the p110alpha subunit of PI3K and/or inactivating mutations in phosphatase and tensin homolog (PTEN) were considered crucial for trastuzumab resistance through sustained activation of the PI3K/AKT signaling pathway [68]. Mutations in PI3K and PTEN reveal a tremendous effect on cell metabolism since a single DNA base change in a particular gene can lead

to a 10,000-fold shift in the level of endogenous metabolites [9].

The metabolic analysis could serve as a surrogate for the quantity of the drug target HER2 and simultaneously detect the before mentioned resistance mechanisms. These associated changes may illustrate a better possibility to predict trastuzumab response in contrast to the quantity of the drug target protein. For example, the expression of the enzyme glutamine synthetase is associated with HER2 protein quantity and, therefore, could act as a surrogate for the HER2 quantity [77]. A multimodal analysis may even offer the possibility to measure both drug target and metabolites. However, utilizing metabolites as predictive biomarkers for trastuzumab treatment is an emerging field of application. A first study revealed promising potential as the metabolic and circulating biomarkers spermidine and tryptophan can stratify good and poor responders to trastuzumab-paclitaxel neoadjuvant therapy in HER2 positive breast cancer patients [78].

Besides HER2-targeted anti-cancer therapies, immune-checkpoint inhibitors become crucial in treating diverse tumor entities. Immune checkpoint inhibitors stimulate and induce therapeutic antitumor immunity more comprehensively, albeit these compounds can also be regarded as molecularly targeted agents because they bind selectively to specific targets, such as programmed cell death-1 (PD-1) and PD-L1 [79]. The inhibitory PD-1-PD-L1 pathway is important for regulating T cell activation and is used by tumor cells to avoid antitumor responses [80]. Several anti-PD1 and anti-PD-L1 monoclonal antibodies were approved for advanced non-small-cell lung cancer (NSCLC) [80]. Meta-analyses in advanced NSCLC indicate that patients with higher tumor PD-L1 expression respond better to anti-PD-1 and anti-PD-L1 agents than patients with lower PD-L1 expression [80]. Very similar to HER2, it can be assumed that metabolites can also indicate response to immune-checkpoint inhibitors. Especially for immune-checkpoint inhibitors, the constitution of the host immune system plays a crucial role in therapy response. Metabolites reflect the constitution of the host immune system. We showed for the first time in our publication [3] that PD-L1 expression is associated with the *in situ* abundance of metabolites in lung cancer (see chapter 3.3).

In conclusion, metabolites reveal promising potential to serve as new predictive biomarkers for targeted cancer therapy response. However, it remains challenging since the clinical setting clearly defines the analysis material. The metabolic investigations must be implemented in the clinical gold standard, pretherapeutic biopsies, or accessible patient materials.

2.2. Metabolomics

The following part of the thesis introduces the technical background of spatial metabolomics, while bulk metabolomics is explained first. This part provides an overview of technical possibilities for obtaining metabolic data from tissues.

2.2.1. Bulk metabolomics

Metabolomics can be used to analyze cancer-associated metabolic changes in tissues and is a fast-developing area of life sciences in which advanced analytical techniques are used in combination with sophisticated statistical methods to fully characterize the metabolome [9]. Metabolomics is defined as the measurement of all the metabolites in a given system under a given set of conditions [81]. The metabolome is usually described as the entire collection of metabolites, or small molecule chemicals, found in a given organelle, cell, organ, biofluid, or organism [9]. A metabolite can be defined as any small molecule with a molecular mass of less than 1,500 Da [9]. Next to endogenous metabolites, this molecule group also comprises more exotic, xenobiotic compounds derived from food or the environment, such as chemical contaminants, pollutants, and herbicides [9]. These xenobiotic molecules are frequently termed exogenous metabolites and are grouped into a single entity called the exposome [9]. The exposome is highly variable, depending strongly on the dietary habits, environmental influences, and even the intestinal microflora of an organism [9].

Performing metabolomics means measuring an enormous number of compounds [82]. The absolute number of metabolites remains unknown in humans. One common metabolite database lists 220,945 metabolites which is only a fraction of human metabolites [83]. Experts estimate 1,000,000 metabolites from over 300 chemical classes as an expectable value for the total amount of metabolites in humans [9]. By comparing the total amount of metabolites to the human genome (approximately 20,300 genes) or the human proteome (about 620,000 protein species), the metabolome is both larger and much more challenging to measure [9]. The chemical complexity arising from approximately 300 different chemical classes means that metabolomic measurements need a much wider variety of equipment than genomic or proteomic measurements, focusing on two chemical classes, nucleobases and amino acids [9].

The metabolomics workflow typically begins with a biological sample, such as a tissue biopsy, metabolically quenched with liquid nitrogen (Figure 2) [9]. For non-spatial tissue-based approaches, the sample is consequently extracted or homogenized to obtain a liquid mixture containing hundreds to thousands of metabolites [9]. The biofluid can be measured through one or more analytical chemistry platforms such as liquid

chromatography-mass spectrometry (LC-MS), gas chromatography-mass spectrometry (GC-MS), capillary electrophoresis-mass spectrometry (CE-MS), ion mobility spectrometry- MS, or nuclear magnetic resonance (NMR) systems [9]. Although this bulk metabolomics method is broadly accepted and can successfully detect changes in metabolism in an organism, it is impossible to precisely determine the localization of metabolites in specific organelles, cells, anatomically or histologically defined parts of tissues or organs [84]. This is followed by the fact that the biological interpretation of metabolomics data is challenging and difficult to assign general metabolic changes to a specific tissue, organ, or spatially restricted abnormality such as a tumor [84].
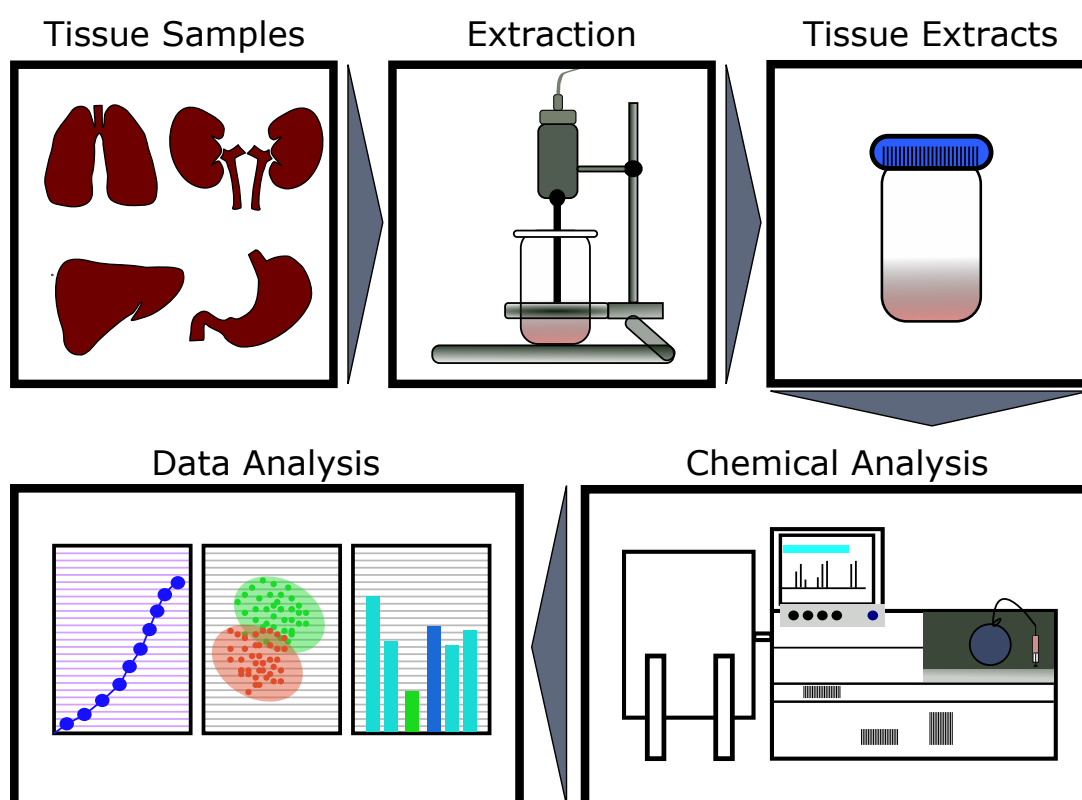

Figure 2. Scheme presenting the typical workflow of a non-spatial metabolomics experiment of a tissue sample. Tissues can be isolated and extracted. Samples are chemically analyzed utilizing gas chromatography-mass spectrometry (GC-MS), liquid chromatography-mass spectrometry (LC-MS), Fourier transform ion cyclotron resonance mass spectrometry (FT-ICR-MS), or nuclear magnetic resonance spectroscopy (NMR), and the resulting spectra are processed to provide long lists of significant compounds or features.

In general, there are different types of metabolomics experiments: 1) targeted metabolomics, 2) untargeted metabolomics, and 3) fluxomics [9]. Untargeted metabolomics includes LC-MS, GC-MS, or CE-MS in an attempt to characterize as many metabolites or putative metabolites as possible (often over 10,000 features) [9]. In MS-based

metabolomics, the expression "feature" typically means a unique m/z ratio and chromato-graphic retention/elution time [9]. In general, untargeted metabolomics is a semi-quantitative method and is ideal for metabolite discovery and hypothesis generation [9].

MS is unique among analytical methods since it can directly analyze single molecular species in complex samples, making a significant contribution to the understanding of biological molecules [85]. The quest to gain new biological insights has also pushed the development of novel MS instruments [85]. Several MS techniques have been developed and used to assess the structure of different metabolites based on their ion mass-to-charge ratio (m/z) [86]. MS is frequently coupled with separation techniques (e.g., chromatography) to better separate and detect metabolites based on their physicochemical properties [86]. However, certain MS techniques can be used without coupling with chromatography for metabolite measurement [86]. These techniques include matrix-assisted laser desorption/ionization (MALDI)-time of flight MS, direct infusion MS, Orbitrap MS, Fourier transform ion cyclotron resonance (FT-ICR) MS, and secondary ion MS [86].

Mass spectrometers with high mass resolution are a prerequisite in metabolomics analysis [82]. This enables to differentiate metabolites at the parts per billion to parts per million level. The FT-ICR and Orbitrap are superior to any commonly used mass spectrometer in absolute resolving power [82]. FT-ICR is proven to be one of the best-performing mass analyzers in resolving power, mass accuracy, and sensitivity [82].

The technical development of the FT-ICR started in the late 1920s when Ernest O. Lawrence invented the cyclotron, which uses electric and magnetic fields to accelerate protons along a spiral path to high speeds before colliding with their target [82]. In a subsequent study, it was also shown that in ICR, the angular frequency of the orbital motion of ions species is independent of the radius on which they move [82]. John A. Hipple used this principle to construct the first ICR mass spectrometer [82]. However, the major breakthrough in this technique was in 1974 when Alan Marshall and Melvin Comisarow applied FT to ICR [82].

Charged ions are one prerequisite for MS analysis. Individual ionization techniques were coupled with mass spectrometers to produce charged ions. With the implementation of ionization techniques, including electrospray ionization [87] and MALDI [88], the area of MS has grown rapidly driven by the application of MS to biological molecules [85]. The success of the ionization technique MALDI began with biotyping, a popular method for identifying microorganisms in clinics. Biotyping is facilitated by measuring mostly ribosomal proteins of bacterial colonies between a mass range of 2,000 - 15,000 m/z using

MALDI time of flight MS. The obtained data is matched with a mass spectra library from well-characterized clinically relevant microorganisms [89]. MALDI has been implemented for research purposes in the metabolite mass range. Since the laser energy is indirectly transferred to the sample analytes via the UV-ionized matrix, MALDI is regarded as a soft ionization that results in low ion fragmentation [90]. MALDI enables high sensitive measurements of biological metabolites in pico- or femtomolar concentrations [82].

By analyzing the mass-to-charge ratio (m/z) of ionized molecules or their ionized molecular fragments and matching this information to other MS reference spectra of identified chemical structures, it is often possible to conclude the identity of a particular structure [9]. Large databases, including MS reference spectra of pure chemical structures, must be consulted to determine which peaks in these spectra correspond to which chemical compound [9]. However, it is still challenging to link the amount of known chemical structures with the data received by mass spectrometers in metabolomics experiments. Only about 2 percent of spectra can be annotated in an untargeted metabolomics experiment [91]. This means the vast majority of information obtained by metabolomics remains uncharacterized. The lack of signal identification at a molecular level is caused by the structural diversity (isobars and isomers) and dynamic range of metabolites, as well as the missing availability of analytical standards [91]. Therefore, some m/z values remain "features" instead of "metabolites with defined chemical structures".

Non-targeted metabolomics data are usually characterized by huge tables containing tens to hundreds of individual patients concatenated with tens to hundreds of metabolites or features and the corresponding relative abundance of each metabolite or feature [9]. The data processed by statistical approaches, such as a metabolite set enrichment analysis or biological network modeling, can enable key insights into how individual metabolites contribute to specific biological processes or crucial physiological phenomena [9].

Next to MS, NMR spectroscopy is a technique that can reveal specific metabolic pathways, while global metabolic analysis is used to determine the structure of metabolites [86]. In contrast to MS, NMR is a non-destructive method [9]. The advantages of MS over NMR are higher sensitivity, real-time measurement of a wide range of metabolites, and only the need for a small sample volume in the pico-mole range for the analysis [86].

2.2.2. Spatial metabolomics

Humans are able to recognize relevant information from complex systems by processing visual information [85]. Novel technologies for acquiring images of biological specimens have served a key role in maturing our modern understanding of biology [85]. One of

these novel technologies is MS imaging, which can perform spatial metabolomics directly from biological specimens to produce chemical and spatially-resolved information and images [85]. Spatial metabolomics is a technology that enables the mapping of hundreds to thousands of metabolites within tissues.

The principle of spatial metabolomics differs from the classical bulk metabolomics workflow. The preparation of the sample and acquisition of the MS data must be done in such a way that the spatial integrity of the biological sample is maintained [85]. Instead of homogenizing, the tissue will be sectioned into 3 - 20 µm thick sections and mounted on glass slides for preserving tissue architecture [85]. The subsequent remaining procedure is very similar to a classical non-targeted metabolomics approach (Figure 3).
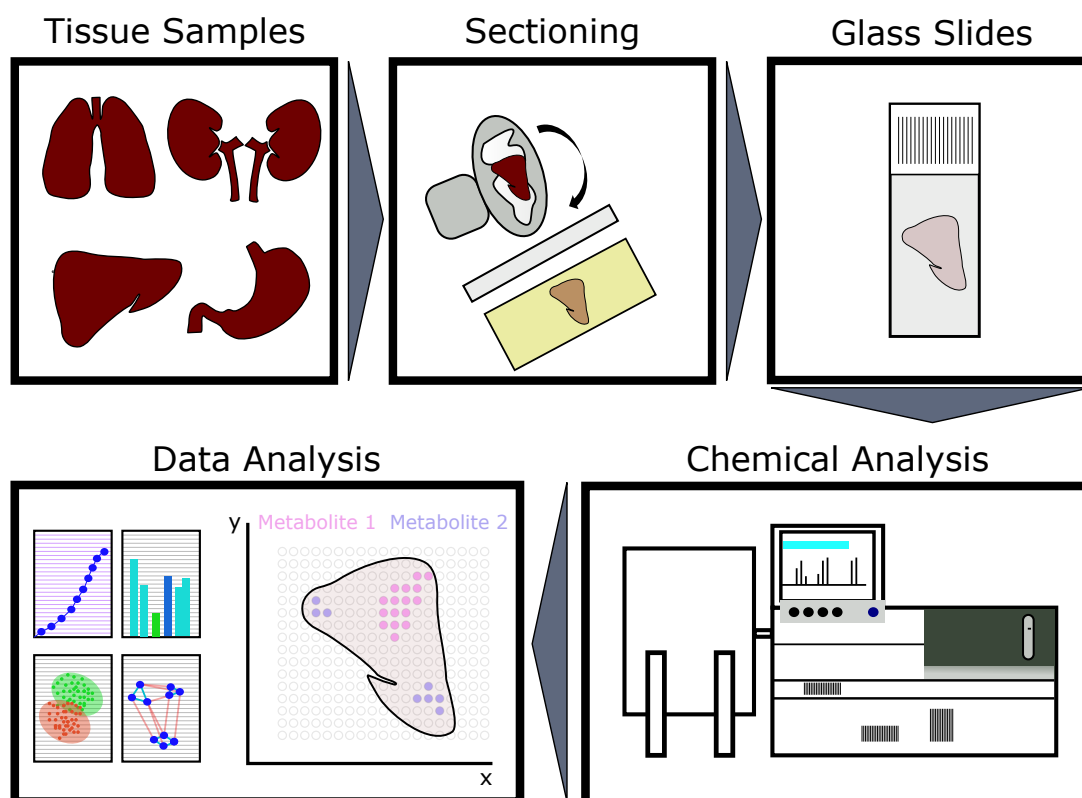

Figure 3. Scheme presenting the typical workflow of a spatial metabolomics experiment. Tissue architecture is preserved by sectioning the tissues instead of extracting the metabolites into a liquid phase. Samples are mounted on glass slides and chemical analyzed utilizing mass spectrometers. The resulting spectra are analyzed to examine the spatial distribution of compounds or features in the tissue and to provide long lists of significant compounds or features.

Several different spatial metabolomics methods are available. However, the basic imaging process is shared by all platforms [85]. The ionization source scans over the tissue section in X, and Y coordinates, while a mass spectrometer acquires a mass

spectrum for each position [92]. The images are constructed by visualizing the intensities of a particular ion on a coordinate system corresponding to the relative position of the mass spectral acquisition in the tissue [85]. The resulting data can be seen as a hyperspectral image containing multiple ion images or channels, where each ion channel corresponds to one m/z value and represents the relative intensities of the ions with that m/z value [84]. The implementation of different ionization techniques and instrumentation varies for each specific spatial metabolomics experiment [85].
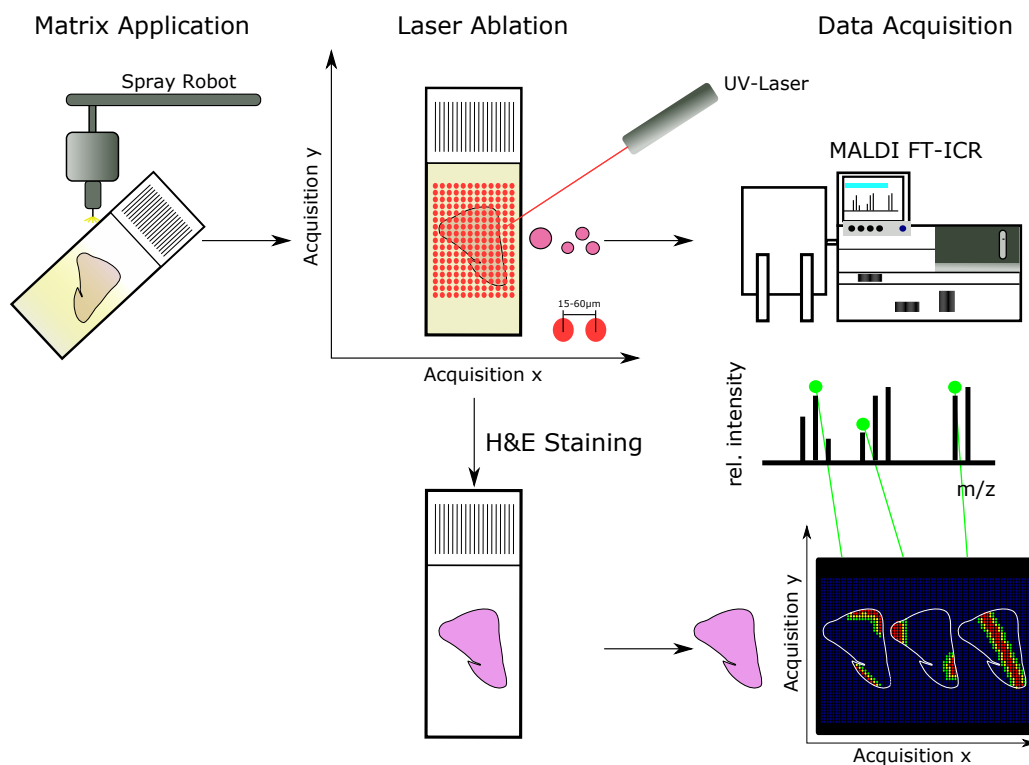

Figure 4. Workflow for matrix-assisted laser desorption/ionization (MALDI) based spatial metabolomics. A conventional tissue section is covered with a matrix to extract molecules from the tissue. The sample is then analyzed in a predefined raster in the mass spectrometer, yielding spatially resolved mass spectra, while the UV laser only hits the matrix crystals without affecting the tissue section. Following spatial metabolomics, histological staining is performed, allowing a histologically oriented mass spectra evaluation.

MALDI-based spatial metabolomics is an example of a metabolomics experiment and uses a laser to desorb and ionize metabolites mixed with a matrix [85]. The matrix is applied to the tissue section mounted on a glass slide via sublimation, spraying with an artistic airbrush, an automated sprayer, or through a fine stainless steel sieve [85, 90]. The matrix solution extracts the analytes from the sample and thus supports desorption/ionization [85]. The selection of the matrix is crucial since the success of the analysis of a particular molecule class depends on this choice [85]. For negative

ion mode analysis of metabolites, 9-aminoacridine is typically used [93]. After matrix application, the laser shoots into the matrix layer in a predefined raster only [94, 85]. The underlying tissue is kept intact, allowing histological examination after measurement in the very same tissue section [94]. The spatial resolution of the spatial metabolomics experiment is defined by the ablation area of the laser and the distance between the laser ablation points (pitch) [93]. While the detailed mechanism of ion formation in MALDI remains controversial, the simplest description of the procedure is to imagine that laser irradiation causes an "explosion" at the surface of the sample under the beam [92]. This explosion produces a plume of material in the gas phase directly above the tissue surface, containing a mixture of metabolites, matrix ions, and neutral species [92]. The plume of desorbed material is then accelerated from the source into the mass analyzer by applying an electric field [92].

Spatial metabolomics can also be merged with other imaging modalities to yield additional, complementary, and multimodal information about the tissue. For instance, many cell types and functional cell states are particularly well suited for analysis by dedicated methods such as immunostaining, and their integration can significantly improve the molecular specificity of spatial metabolomics [93]. Brightfield microscopy and histological stains, including hematoxylin and eosin, are commonly used in pathology to evaluate the integrity, health, and disease of tissues [93]. Following spatial metabolomics, the very same tissue section can be stained, e.g., with hematoxylin and eosin or immunostaining, and coregistered with the mass spectrometric analysis [94]. The combination of stainings and spatial metabolomics allows assigning the visualization of individual metabolites to specific tissue compartments (e.g., tumor cells and tumor stroma). The combination also enables the generation of cell type specific molecular signatures [94]. In principle, this works in the same way as tissue microdissection [94]. In contrary to tissue microdissection, spatial metabolomics conducts microdissection "virtually" by defining regions of interest (ROI) and extracting mass spectrometric profiles within these ROI [94].

One of the major assets of spatial metabolomics is that there is only the need for relatively minimal sample preparation in contrast to more traditional bioassay-based workflows [90]. Time demanding and error-prone extraction procedures of bulk metabolomics can be skipped using spatial metabolomics. Second, in comparison to bulk metabolomics, spatial metabolomics allows assigning metabolic changes to particular organelles and cells within tissues [84]. This eases the biological interpretation of the metabolomic data. Third, spatial metabolomics can detect metabolites without labeling or otherwise structurally modifying them [85]. This prevents potential problems if the labeling reagent affects or alters the physical, chemical, or biological function of the

metabolite [85]. Fourth, only a very small amount of tissue is required. One thin tissue section of a pretherapeutic biopsy is sufficient for performing spatial metabolomics [95].

Taken together, throughout the introduction of this thesis, several challenges were highlighted for studying metabolic changes in tissues associated with cancer disease. In particular, there is a need for advanced *omics* technologies to overcome tissue heterogeneity, high sensitive detection of metabolic changes, multimodality, and handling small tissue biopsies. Spatial metabolomics addresses all these issues. Since the possibility of virtual microdissection, tissue heterogeneity can be overcome. The MALDI approach reveals high sensitivity for metabolic changes, and multimodality is given since a multitude of imaging approaches can use the same tissue section. In addition, a recent study revealed the potential of spatial metabolomics for pretherapeutic tissue biopsies [95]. These are the reasons for using spatial metabolomics to study cancer-associated metabolic changes in tissues.

2.3. **Aims of this dissertation**

Spatial metabolomics enables a new insight into the cancer metabolism derived from patient tissues with a so-far unrivaled grade of detail. Metabolomic analysis of cancer cells can be exclusively performed *in situ* by spatial metabolomics. However, it can be challenging to find degenerated cells because of the high complexity of tissues. A multimodal approach combining spatial metabolomics with other spatially resolved tissue analytics is often needed to detect altered cells.

This thesis aims to address unmet clinical needs in cancer therapy and provide new insights into cancer metabolism by initially developing [1, 2] and extensively applying [3, 4] an improved spatial metabolomics method. The enhanced spatial metabolomics method will integrate metabolomics, genetics, and protein expression of the same tissue section while preserving spatial information. As a result, the integration will allow the analysis of the metabolome of pathologically changed cells selectively and reveal a whole new insight into cancer metabolism in tissues by simultaneously considering several molecular layers.

This enhanced spatial metabolomics method will be applied to improve diagnosis and enable targeted anti-cancer therapies. HER2 and PD-1/PD-L1 were frequently targeted for anti-cancer therapy; however, not all patients benefit from the treatment. In addition, so far there is no definitive therapy available against cancer cachexia. For these reasons, this thesis focuses on developing this improved metabolomics method [1, 2] and on applying this method for enhancing diagnosis and enabling options for targeted anti-cancer therapies by analyzing tissues of patients with the aforementioned pathological conditions [1, 2, 3, 4].

3. First Author Publications

The next chapter provides the peer-reviewed first author publications that comprise my work during my doctoral studies and makes this thesis eligible for credit as a cumulative dissertation. The first two publications [1, 2] focus mainly on developing the improved spatial metabolomics method, while the last two publications [3, 4] provide in-depth insights into the cancer metabolism by applying the improved spatial metabolomics method. Before each embedded publication, a short introduction resuming the respective work is given, and my individual contributions are mentioned.

3.1. Multimodal analysis of formalin-fixed and paraffin-embedded tissue by MALDI imaging and fluorescence *in situ* hybridization for combined genetic and metabolic analysis

The publication entitled "Multimodal analysis of formalin-fixed and paraffin-embedded tissue by MALDI imaging and fluorescence *in situ* hybridization for combined genetic and metabolic analysis" [1] represents the beginning of my work to enable an improved spatial metabolomics method for the multimodal investigation of several molecular layers to provide new insights into cancer-associated metabolic changes in tissues. We were interested in the idea of combining spatial metabolomics with *in situ* hybridization to access the information of gene copy number and metabolomics simultaneously. The *HER2* gene copy number assessment is an already established clinical procedure for predicting anti-HER2 therapy response in patients with gastric cancer. We aimed to add a new layer of a molecular class onto the established clinical prediction system to increase the accuracy of the anti-HER2 therapy response prediction. This work presents the proof-of-principle that a multimodal analysis with spatial metabolomics and *in situ* hybridization is possible in the very same tissue section. Furthermore, this work revealed for the first time that the synergism of metabolomics and *HER2* gene copy number improves the prognostic effect of biomarkers in patients with intestinal tumors. Therefore this work illustrates an important steppingstone for further developing a multimodal integration method that preserves the spatial information of each molecular layer. Furthermore, this publication underlines the metabolic heterogeneity of cancer

cells despite similar HER2 expression, which could be crucial for anti-HER2 therapy response prediction.

I am sharing the first authorship with my former colleague Katharina Huber. Specifically, I processed the data using R programming and calculated all statistics included in this manuscript. Furthermore, I interpreted the data, wrote the original draft of the manuscript, and prepared all figures together with Katharina Huber. After peer-review, I was responsible for editing the manuscript and performing new experiments according to reviewers' suggestions. In addition, I co-designed this study together with Katharina Huber and Axel Walch.

We aim to protect the idea behind the presented publication [1] by the following patent application:

- Walch A, Huber K, Buck A, **Kunzke T**. IN-VITRO METHOD FOR DIAGNOSIS AND PROGNOSIS OF A DISEASE (2020), Luxemburg Patent Application LU101032, published 2020-06.

USCAP

TECHNICAL REPORT

Multimodal analysis of formalin-fixed and paraffin-embedded tissue by MALDI imaging and fluorescence in situ hybridization for combined genetic and metabolic analysis

Katharina Huber[1] · Thomas Kunzke[1] · Achim Buck[1] · Rupert Langer[2] · Birgit Luber[3] · Annette Feuchtinger[1] · Axel Walch[1]

Abstract

Multimodal tissue analyses that combine two or more detection technologies provide synergistic value compared to single methods and are employed increasingly in the field of tissue-based diagnostics and research. Here, we report a technical pipeline that describes a combined approach of HER2/CEP17 fluorescence in situ hybridization (FISH) analysis with MALDI imaging on the very same section of formalin-fixed and paraffin-embedded (FFPE) tissue. FFPE biopsies and a tissue microarray of human gastroesophageal adenocarcinoma were analyzed by MALDI imaging. Subsequently, the very same section was hybridized by HER2/CEP17 FISH. We found that tissue morphology of both, the biopsies and the tissue microarray, was unaffected by MALDI imaging and the HER2 and CEP17 FISH signals were analyzable. In comparison with FISH analysis of samples without MALDI imaging, we observed no difference in terms of fluorescence signal intensity and gene copy number. Our combined approach revealed adenosine monophosphate, measured by MALDI imaging, as a prognostic marker. HER2 amplification, which was detected by FISH, is a stratifier between good and poor patient prognosis. By integrating both stratification parameters on the basis of our combined approach, we were able to strikingly improve the prognostic effect. Combining molecules detected by MALDI imaging with the gene copy number detected by HER2/CEP17 FISH, we found a synergistic effect, which enhances patient prognosis. This study shows that our combined approach allows the detection of genetic and metabolic properties from one very same FFPE tissue section, which are specific for HER2 and hence suitable for prognosis. Furthermore, this synergism might be useful for response prediction in tumors.

Introduction

The present work describes a combined method for the multimodal analysis of one very same tissue section. The

These authors contributed equally: Katharina Huber, Thomas Kunzke

Supplementary information The online version of this article (https://doi.org/10.1038/s41374-019-0268-z) contains supplementary material, which is available to authorized users.

✉ Axel Walch
   axel.walch@helmholtz-muenchen.de

1 Research Unit Analytical Pathology, Helmholtz Zentrum München, German Research Center for Environmental Health, Neuherberg, Germany

2 Institute of Pathology, University of Bern, Bern, Switzerland

3 Institute of Pathology, Technische Universität München, Munich, Germany

addition of two or more technologies enables a new way of analysis, which adds further information for diagnosis, treatment, and monitoring [1, 2]. It has been demonstrated that the addition of a further modality can drastically enhance information gain in tissue-based analysis [3]. In clinical research, there are numerous developments especially in the field of multimodal molecular imaging, which promise to improve treatment strategy, targeted therapy, and personalized medicine [1].

In this study, MALDI imaging is added as a further modality to the genetic FISH analysis.

MALDI imaging is an emerging tool for the investigation of proteins, peptides, lipids, metabolites, small molecules, and many other classes in a spatially resolved manner [4–6]. Meanwhile, MALDI imaging is a technology suitable for diagnostics and for predictive approaches, which is unique in providing molecular information with spatial resolution [7]. Previously matrix-assisted laser desorption ionization (MALDI) imaging was established

SPRINGER NATURE

for the metabolic analysis of formalin-fixed and paraffin-embedded (FFPE) tissues [8]. This achievement enables analysis of the metabolic content of large tissue banks and clinical samples, which are usually preserved and stored as paraffin blocks.

The employment of a further measurement modality without further need of tissue, but in just using one very same tissue section for several analyses, seems meaningful, especially in the context of limited human diagnostic material. Although method combination with MALDI imaging seems promising, there are only few studies, which have already used MALDI imaging for multimodal approaches. An example is the proteomic analysis by MALDI imaging combined with receptor staining by immunohistochemistry using one very same tissue section for both modalities [7].

In cancer treatment, the examination of drug targets is an important tool for estimation of drug efficiency and therapy response [9]. The human epithelial growth factor receptor 2 (HER2) is a receptor, which is overexpressed in several cancer types such as breast cancer and gastroesophageal adenocarcinoma [9, 10]. Thus, HER2 serves as a drug target and the binding antibody, known as Trastuzumab, is in wide use as a cancer therapeutic [10]. As targeting HER2 is only successful when overexpressed, HER2 testing by immunohistochemistry (IHC) and fluorescence in situ hybridization (FISH) is a routine method in diagnosing the respective cancer diseases [11].

State of the art in HER2 diagnosis is immunohistochemical staining and in situ hybridization [12]. The immunohistochemical staining, directly labeling HER2, is scored as 0, 1+, 2+, or 3+. Score 0 and 1+ are defined as HER2 negative, which means anti-HER2 treatment is not considered at all, and 3+ is HER2 positive, an outcome, which recommends anti-HER2 treatment. The score 2+ represents an intermediate state, which requires further testing. In this case in situ hybridization is performed as fluorescence or chromogenic in situ hybridization. Hereby the signals of labeled gene copies are counted in at least 20 tumor cell nuclei and a ratio of gene copy number and chromosome number is calculated and defined as amplified when the ratio is ≥2. Samples with a ratio of 2 or more are then also defined as HER2 positive and this leads to an HER2 directed treatment [11–13].

In HER2 testing, FISH is an FDA approved method for the enumeration of the absolute HER2 gene copy number in breast cancer and gastroesophageal adenocarcinoma [11, 14–16]. Nonetheless, there is still potential for improving diagnostics and response prediction for HER2 directed treatments. There is a subgroup of HER2-positive cancer patients, which do not respond to anti-HER2 treatment and hence the patients do not profit from yet very cost intensive medication but undergo the risk of side effects [17–21].

Thus, the integration of additional metabolic markers may lead to a better prognosis. Tumor growth and progression is an energy demanding process, consuming high amounts of adenosine triphosphate (ATP) [22]. If ATP supply is not sufficient, adenosine monophosphate levels rise and activate adenosine monophosphate-activated kinase (AMPK), which induces catabolic pathways to support ATP production [22]. High AMP levels are described to activate AMPK, which further activates pathways that are involved in tumor growth, autophagy, and metabolism [23–25]. Hence, the AMP level may reflect AMPK activation.

HER2-positive breast cancer cells were shown to display AMPK activation and in 2015 AMPK was found to regulate HER2 activity [26, 27]. Therefore we focus on measuring the adenosine monophosphate (AMP) level in the tumor areas of gastroesophageal adenocarcinomas. So far no in situ method is suitable for the detection of AMP, this is a domain of mass spectrometry, more specifically mass spectrometry imaging. Previous studies showed the feasibility for measuring AMP by MALDI imaging in different kind of tissues [28–31]. Buck et al. [8] verified the detection of AMP in FFPE tissues by MSMS experiments. In addition, a successful analysis was also formerly been performed liquid based for AMP in FFPE tissues [32]. Thus, we used MALDI imaging as a further modality to increase the information received from FISH analysis and hence to get an enhanced disease prognosis.

In the present study, we combined metabolic information from MALDI imaging data with genetic information from HER2 FISH analysis of the very same tissue sections and found that HER2 status testing by FISH and AMP levels detected by MALDI imaging have a synergistic effect for prognosis.

Materials and methods

Human tissue samples

At all, 74 human gastroesophageal adenocarcinoma patient samples were analyzed.

Sixty-nine tissue samples of gastroesophageal adenocarcinoma were collected between 1993 and 2010 at the Department of Surgery, Klinikum Rechts der Isar, Munich, Germany. This study was approved by the local Ethics Committees.

Tissue samples were fixed for 12–24 h in 10% neutral buffered formalin whereafter specimen were embedded in paraffin using standardized automated procedures. Prior to

embedding in molten paraffin, the samples were dehydrated in increasing ethanol series and cleared using xylene. The resulting paraffin blocks from the cohort collected in Munich were then used for the preparation of a tissue microarray (TMA).

Five biopsies of human gastroesophageal adenocarcinoma, collected at the Institute of Pathology, University of Bern, Bern, Switzerland, were chosen for the establishment and validation of the workflow due to the previously found HER2 gene amplification. The usage of archival FFPE tissue for research was approved by the local ethics commission (Kantonale Ethikkommission Bern, Switzerland, 200/14).

Multimodal tissue analysis by MALDI imaging and fluorescence in situ hybridization (FISH)

The goal of this methodic work is the combination of two modalities: metabolites by MALDI imaging and gene copy number by fluorescence in situ hybridization (FISH) using one very same formalin-fixed and paraffin-embedded (FFPE) tissue section for all imaging modalities. The workflow is depicted in Fig. 1, starting with the MALDI imaging measurement followed by H&E staining. For performing the second modality, FISH, the coverglass was removed and a special washing procedure was carried out to ensure the complete elimination of mounting medium from the tissue. As a last step, data gained from MALDI imaging

Fig. 1 The workflow of MALDI imaging with H&E staining, followed by a FISH analysis on the very same tissue section

and FISH were fused in order to enhance prognosis prediction in the patient cohort (Fig. 1).

Tissue preparation

Tissue sections of 4 µm thickness were cut using CM1950 cryostat (Leica Microsystems, Wetzlar, Germany) and mounted onto indium-tin-oxide (ITO) coated glass slides (Bruker Daltonik GmbH, Bremen, Germany), which were previously covered with 1:1 poly-L-lysine (Sigma-Aldrich; Taufkirchen, Germany) and 0.1% Nonidet P-40 (Sigma-Aldrich; Taufkirchen, Germany). For deparaffinization, sections were incubated at 70 °C for 1 h and washed twice in xylene for 8 min. Prior MALDI matrix application, tissue sections were air-dried on a heating plate at 35 °C for 1 min and scanned using a flatbed scanner in order to acquire digital tissue images for co-registration purposes. Subsequently, the samples were covered with 10 mg/mL 9-aminoacridine matrix (Sigma-Aldrich) in 70% methanol (purity ≥99.9%), using a SunCollect sprayer (Sunchrom, Friedrichsdorf, Germany) according to Ly et al. [33]. In detail, the following preferences were applied for the automatic sprayer: vial distance of 0.50 mm for the X direction and 2.00 mm for the Y direction, 20 mm Z-position and offset of the spray head, and medium X/Y speed. The matrix was deposited in eight layers using variable increasing spray rates. Following spray rates were used: Layer 1: 10 µl/min, layer 2: 20 µl/min, layer 3: 30 µl/min, layer 4–8: 40 µl/min. At all, the whole procedure is resulting in a total amount of 0.16 mg/cm^2 9-aminoacridine.

MALDI imaging

MALDI imaging was performed using a Solarix 7 T FT-ICR mass spectrometer (Bruker Daltonik GmbH, Bremen, Germany) at a spatial resolution of 60 µm in negative ion mode in the mass range of m/z 50–1000, whereby 50 laser shots were accumulated for each position measured. The software packages FlexImaging 4.0 and SolarixControl 3.0 (Bruker Daltonik GmbH, Bremen, Germany) were applied for data generation and visualization as previously described [33, 34].

After MALDI measurement, matrix was removed by a washing step in 70% ethanol for 1 min and subsequently stained with histological hematoxylin and eosin staining as described previously. Coverglass was mounted using Pertex mounting medium (Medite GmbH, Burgdorf, Germany).

For digitalization slides were scanned at 20x objective magnification with a slide scanner (Mirax Desk, Carl Zeiss MicroImaging GmbH, Jena, Germany). For co-registration with MALDI imaging data, the images were imported into the FlexImaging 4.0 software (Bruker Daltonik GmbH, Bremen, Germany).
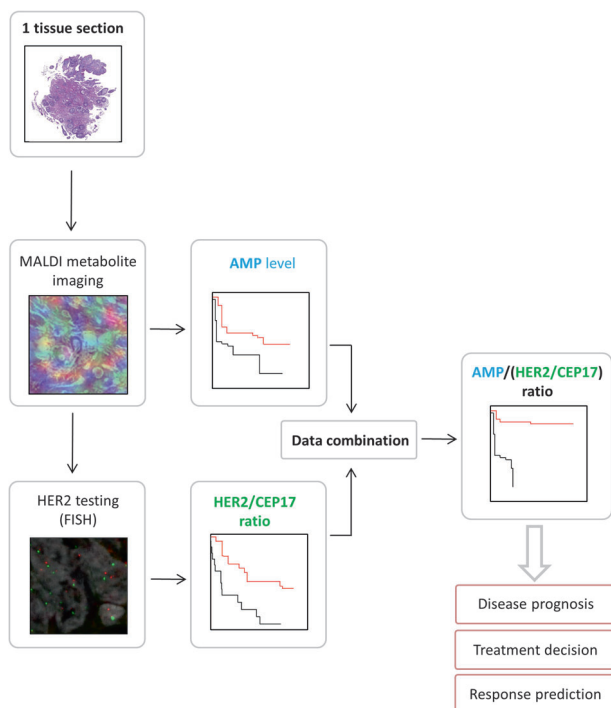
FISH experiment

The FISH experiment was performed using the tissue sections, which were stained with hematoxylin and eosin after the MALDI imaging measurement (Fig. 1).

Slides were incubated in xylene at room temperature for 12 h before coverglass was removed. Subsequently further washing steps in xylene and isopropyl alcohol, each for the duration of 1 h, were carried out. This washing procedure was followed by a series of decreasing ethanol concentrations from 100% down to 50%, whereas the sections were immersed for 5 min at each step before they were transferred into demineralized water.

After incubating for 5 min in PBS (Sigma-Aldrich; Taufkirchen, Germany) at room temperature, the sections were boiled in citrate buffer containing 0.1 M citric acid (Sigma-Aldrich; Taufkirchen, Germany) and 0.1 M sodium citrate (Sigma-Aldrich; Taufkirchen, Germany) for 20 min using a microwave oven at 350 W. Afterwards the sections were washed in PBS and incubated in Pronase E 0.05 % (Sigma-Aldrich; Taufkirchen, Germany) for 5 min at 37 °C. Again one washing step in PBS was performed before the sections were dehydrated in ascending alcohol series, 5 min in each concentration, at −20 °C. The sections were then air-dried at room temperature and heated on a heat plate at 37 °C for 1 min.

HER2-CEP17 probes (PathVysion HER2 DNA Probe Kit II, Abbott, Illinois, USA) were added to the slide, still placed on a 37 °C heat plate, covered with Fixogum rubber cement (Marabu) and stored in the dark. Denaturation happened simultaneously by increasing the temperature of the heat plate to 75 °C for 8 min. For hybridization, slides were kept in a humid atmosphere at 37 °C for 16 h. After the incubation, slides were washed by short immersion in 2x SSC (Sigma-Aldrich; Taufkirchen, Germany) containing 0.3% Nonidet P-40 at room temperature and for 2 min in 2x SSC containing 0.3% Nonidet P-40 at 73 °C. After air-drying, slides were stained using Hoechst (Sigma-Aldrich; Taufkirchen, Germany) at room temperature and air-dried again. Coverglasses were mounted using Vectashield mounting medium (Biozol, Eching, Germany).

The kit consists of directly labeled, fluorescent DNA probes specific for the HER2 gene locus (17q11.2-q12) and a DNA probe specific for the α-satellite DNA sequence at the centromeric region of chromosome 17 (17p11.1-q11.1).

FISH analysis of the biopsy sections without previous MALDI imaging was performed in equal manner at Bern University in Switzerland.

Evaluation of the FISH experiment included counting of the fluorescent labels for gene copy numbers and centromeric region. Therefore a Z1 ZEISS Axioimager microscope (Zeiss, Jena, Germany) with a x63 magnification water objective was used.

Data analysis

For processing of the MALDI imaging data a MATLAB script using the bioinformatics and image processing toolboxes (v.7.10.0, MathWorks, Natick, MA, USA) was employed. Spectra which were exported by the FlexImaging 4.0 software (Bruker Daltonik GmbH, Bremen, Germany) underwent baseline subtraction, resampling, and smoothing as described previously [8, 34]. A signal-to-noise threshold of 2 was used and isotope peaks were excluded automatically. Human Metabolome Database (HMDB, Version 4.0, 114,098 metabolites included) was employed for the identification of m/z species with a mass tolerance of 3 ppm. The resulting peak intensity of AMP was exported to Microsoft Excel for data fusion with the FISH results.

The HER2 FISH approach was evaluated according to the recent guidelines [11]. The signals for HER2 gene loci and CEP17 centromere of 20 non-overlapping tumor cell nuclei were counted manually. The ratio HER2/CEP17 was calculated using Excel, whereas a HER2/CEP17 ratio ≥ 2.0 was considered as HER2 amplification [11]. Samples displaying a HER2/CEP17 ratio < 2.0 were classified as non-amplified. Furthermore, we differentiated the non-amplified samples into two groups. A HER2/CEP17 ratio ≥ 1.1 and < 2 was classified as low-level copy number gain, whereas a HER2/CEP17 ratio < 1.1 shows the status of a normal diploid nucleus [13, 35].

Kaplan–Meier survival tests were performed using R statistics software and Prism was used for correlation plotting.

Results

Nuclear morphology of formalin-fixed and paraffin-embedded (FFPE) tissue is unaffected after MALDI imaging

Human gastroesophageal adenocarcinoma biopsies, in the form of formalin-fixed and paraffin-embedded (FFPE) tissues, were used for validation of the fluorescence in situ hybdridization (FISH) analysis either following MALDI imaging measurement or without a previous MALDI imaging measurement. One section of each biopsy sample was processed for MALDI FT-ICR metabolite imaging. Molecule visualizations resulting from the MALDI imaging approach are displayed in Fig. 2. The molecule signals follow the tissue morphology and, after co-registration with the H&E staining, it is possible to precisely allocate mass signals with tissue structures (Fig. 2). The overlay of MALDI imaging and H&E enables the identification and evaluation of specific tissue structures, e.g., tumor cell regions.

Fig. 2 Biopsies of gastroesophageal adenocarcinoma patients were measured using MALDI FT-ICR imaging for the analysis of metabolites followed by H&E staining. The MALDI visualization of Hex-P (hexose phosphate), GDP (guanosine diphosphate), AMP (adenosine monophosphate), and further molecules are depicted using heatmap coloring in the first block. The MALDI imaging heatmap pictures are displayed as merged figures with the H&E stainings as background to enable morphologic correlation. FISH analysis of both biopsies was performed subsequent to the MALDI imaging procedure. Both biopsies showed HER2 amplification when detected after the MALDI imaging workflow or when performed exclusively. For validation, consecutive sections of the very same biopsies were analyzed by FISH exclusively
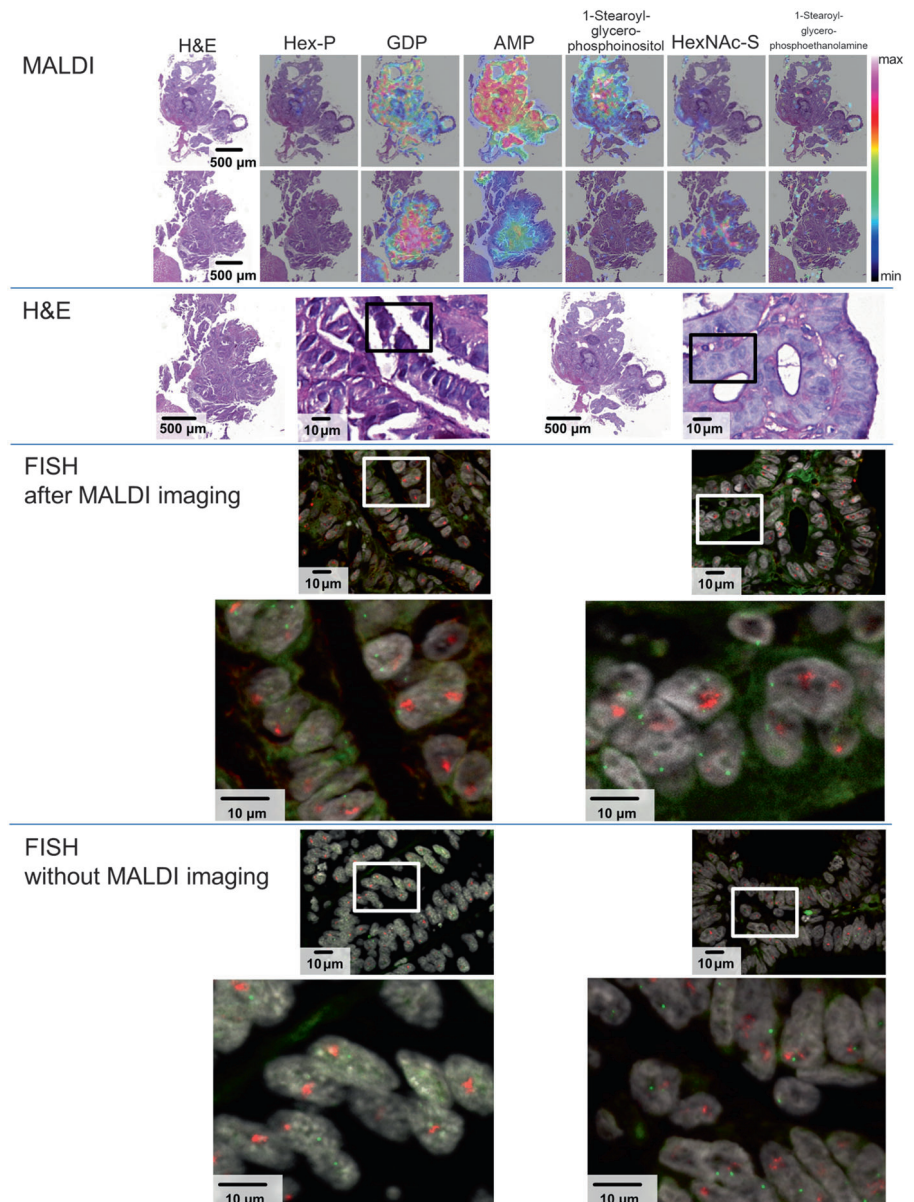
After analysis of the combined MALDI imaging, the coverglass was removed and FISH analysis was performed in order to detect HER2 gene amplification (Fig. 1). Figure 2 shows the direct allocation of tissue structures, precisely identifiable in the H&E staining, with the fluorescence microscopy image of the FISH analysis. In FISH analysis, nuclei are the only cell components, which are stained (gray) (Fig. 2). The HER2 gene loci and the centromere region of chromosome 17 are fluorescent labeled by hybridization with red fluorescent probe (HER2) and green fluorescent probe (CEP17), which enables counting of signal numbers and thusly calculating the HER2/CEP17 signal ratio. There are two major preconditions for reliable HER2 testing. Nuclei must be stained clearly in order to allocate all signals belonging to each

nucleus and fluorescence signals for both, HER2 probe and centromere probe CEP17, have to be clearly visible to enable distinct recognition of single signals.

The FISH analysis was evaluable even after the MALDI imaging procedure. Single fluorescence signals, even in non-amplified tissues were clearly visible and enumeration was possible just as in tissues, which were not used for the MALDI imaging procedure. The nuclear morphology was clear and completely unaffected by MALDI imaging. The Hoechst nuclear staining allowed the detection of tumor areas and even cytomorphological details of the nuclear structure remained unchanged after MALDI imaging.

The ratios of HER2 gene locus (red) and centromeric region of chromosome 17 (green) signals were calculated, whereas a ratio ≥2.0 was designated as HER2 amplification

[11]. In the FISH experiment we found high-level amplification of HER2 gene copy number in both biopsies (Fig. 2). The FISH experiment that was performed after MALDI imaging and H&E staining resulted in excellent signals, which allowed a very precise detection of gene amplifications (Fig. 2).

HER2 testing by FISH after MALDI imaging and without MALDI imaging reveals equal results

In order to validate the findings from the samples, which underwent the MALDI imaging pipeline, consecutive reference sections of five biopsies were analyzed by FISH as a reference, not undergoing the procedure of MALDI imaging and H&E staining. The FISH experiment was evaluated identically for the sections, which underwent the MALDI imaging protocol as for those reference sections

without previous MALDI imaging procedure. All biopsies after MALDI imaging showed HER2 amplification. The quantitative evaluation of the approaches is displayed in Fig. 3. Signal counts of HER2 and CEP17 of five biopsies were compared after the MALDI workflow and without previous MALDI and the HER2/CEP17 signal ratio was calculated. For biopsy 1, an average of 8.0 HER2 signals was detected after MALDI and 10.0 signals without MALDI workflow. CEP17 signal count revealed 1.6 and 1.5 signals per nucleus, respectively. The resulting HER2/CEP17 signal ratios were 5.0 and 6.7. Biopsy 2 showed HER2 amplification with a mean HER2 signal count of 16.8 after MALDI and 15.4 without MALDI. With a CEP17 number of 2.0 and 1.8, the resulting HER2/CEP17 signal ratios were 8.4 and 8.6. The results for biopsy 3, 4, and 5 were also equal after MALDI imaging and were shown in Table 1. Additional exemplary pictures of FISH analysis for
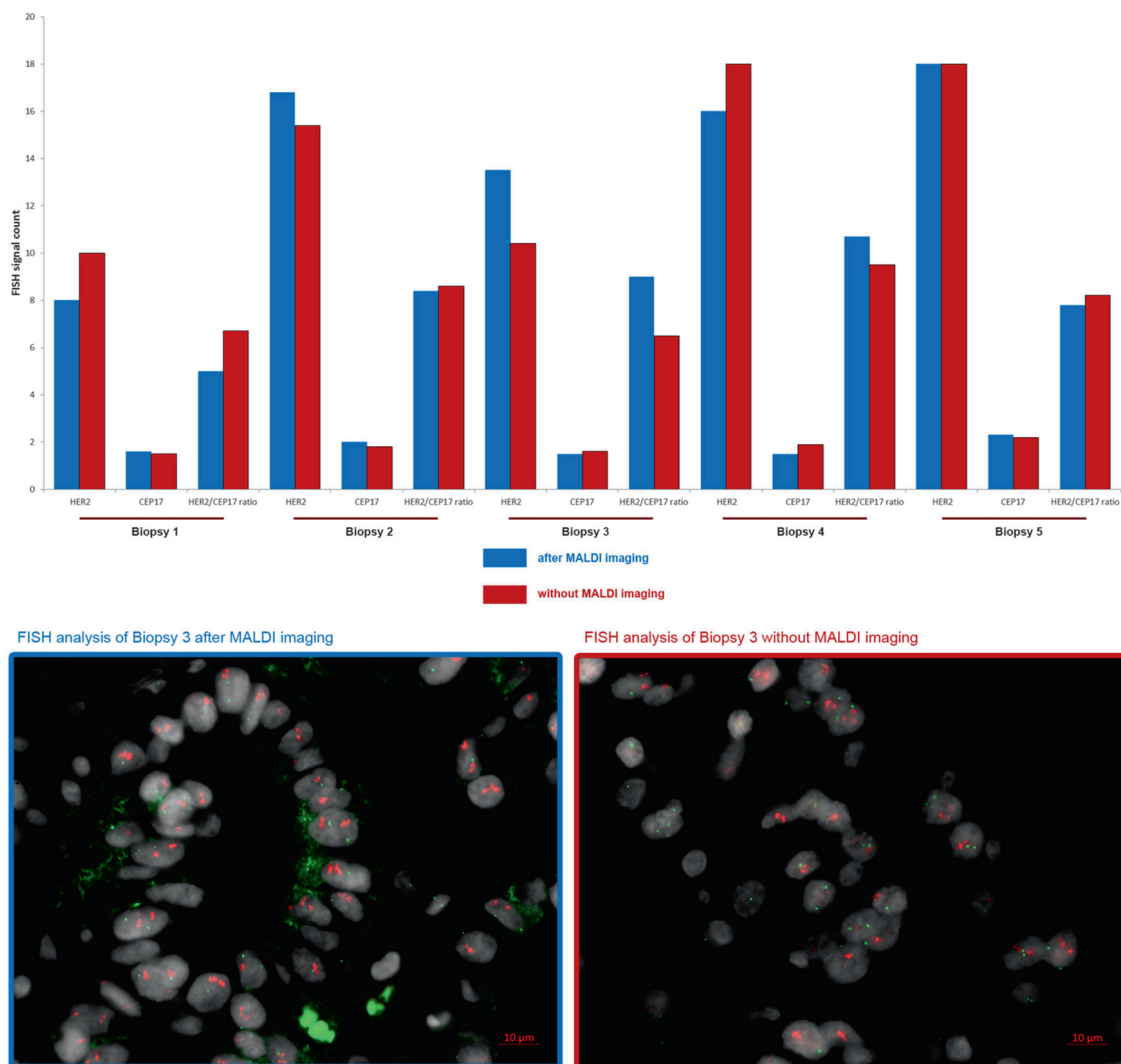

Fig. 3 HER2 signals, CEP17 signals, and HER2/CEP17 ratios derived from FISH analysis of five human gastroesophageal cancer biopsies. FISH signals from 20 tumor cell nuclei were enumerated manually in biopsies, which were analyzed by FISH after the MALDI imaging procedure or without previous MALDI imaging, respectively. The shown examples for FISH are referring to Biopsy 3

Table 1 Comparison of FISH results after and without MALDI imaging

Characteristic	After MALDI imaging	Without MALDI imaging
Biopsy 1		
HER2 [mean signals]	8.0	10.0
CEP17 [mean signals]	1.6	1.5
HER2/CEP17 ratio	5.0	6.7
Biopsy 2		
HER2 [mean signals]	16.8	15.4
CEP17 [mean signals]	2.0	1.8
HER2/CEP17 ratio	8.4	8.6
Biopsy 3		
HER2 [mean signals]	13.5	10.4
CEP17 [mean signals]	1.5	1.6
HER2/CEP17 ratio	9.0	6.5
Biopsy 4		
HER2 [mean signals]	16.0	18.0
CEP17 [mean signals]	1.5	1.9
HER2/CEP17 ratio	10.7	9.5
Biopsy 5		
HER2 [mean signals]	18.0	18.0
CEP17 [mean signals]	2.3	2.2
HER2/CEP17 ratio	7.8	8.2

all biopsies can be seen in Supplementary Fig. 1. Comparing the quality of the tissue after the combined workflow with the tissue that underwent only the FISH experiment, there is no difference in quality and evaluability.

HER2 testing after MALDI imaging allows accurate disease prognosis prediction

A tissue microarray containing 69 human gastroesophageal adenocarcinoma patient samples was analyzed using the established pipeline of MALDI imaging followed by FISH. Figure 4 displays the distribution of several molecules measured by MALDI imaging. As established for the biopsies, the TMA underwent FISH after the MALDI imaging procedure following the same workflow as described above. The results from the FISH analysis are presented in Fig. 5. Tissue cores in Fig. 5a, b showed low/medium level HER2 amplifications, while the core in Fig. 5c was a highly amplified sample. The samples in Fig. 5d, e, f were found to be not HER2 amplified.

In all, nine tissue cores were found to be HER2 amplified, while 60 were not amplified. In the group of non-amplified cores, 18 were found to show low-level copy number gain while 42 where diploid without copy number

gain. Average HER2 signal counts varied from 0.8 to 15.4, the average HER2 signal count of all observed cases was 2.4 signals per nucleus.

The FISH evaluation of the tissue microarray was analyzed statistically using the Kaplan–Meier survival test (Fig. 6). Hereby a significant ($p = 0.0350$) difference in patient survival was found, outlining HER2/CEP17 signal ratio as a marker for patient survival (Fig. 6a).

Adenosine monophosphate is a prognostic factor in gastroesophageal adenocarcinoma

In the MALDI imaging approach, the H&E staining was used for the determination of tumor regions. Thus, it was possible to extract mass spectra specifically from the tumor areas for analysis. We focused on the peak intensity of adenosine monophosphate (AMP, m/z 346.0570), which we expected to serve as prognostic marker. AMP signal intensity allowed significant prediction of patient survival ($p = 0.00206$). Hereby the mass intensity was found to be higher in the good prognosis group, while signal intensity was weak in the poor prognosis group (Fig. 6b). In general, average AMP peak intensities varied between 0 and 7.59. In 39 cases mean AMP intensity was found to be below 1.0 and 2 cases showed an intensity of >5. The intensity of 28 cases was in the medium range between 1.0 and 5.0. The overall average AMP intensity is 1.42. In the samples, which were stratified as poor survivers (Fig. 6b), AMP signal intensity was below 0.15.

Data combination of FISH and MALDI has a synergistic effect on prognosis

According to our hypothesis, we combined the data revealed from both approaches, AMP signal intensity by MALDI imaging and gene amplification by FISH, using the ratio of the mass intensity and the HER2/CEP17 signal ratio, lead to an improvement in the significance of survival analysis with $p = 0.000002875$. The patients in the good prognosis group show a higher AMP/FISH ratio than the patients in the poor prognosis group. The calculated threshold to stratify patient survival was 0.22 (Fig. 6c).

In Supplementary Fig. 2, AMP signal intensities from MALDI imaging were plotted against the HER2 signal count revealed from FISH in order to detect whether there is a correlation of the abundance of both features. Each datapoint represents a single patient. The random distribution of the datapoints in the plot depicts the fact that both parameters do not correlate with each other ($p = 0.5020$). In addition, the HER2/CEP17 ratio was also tested for correlation and reached not a significant level (Supplementary Fig. 3, $p = 0.2183$).
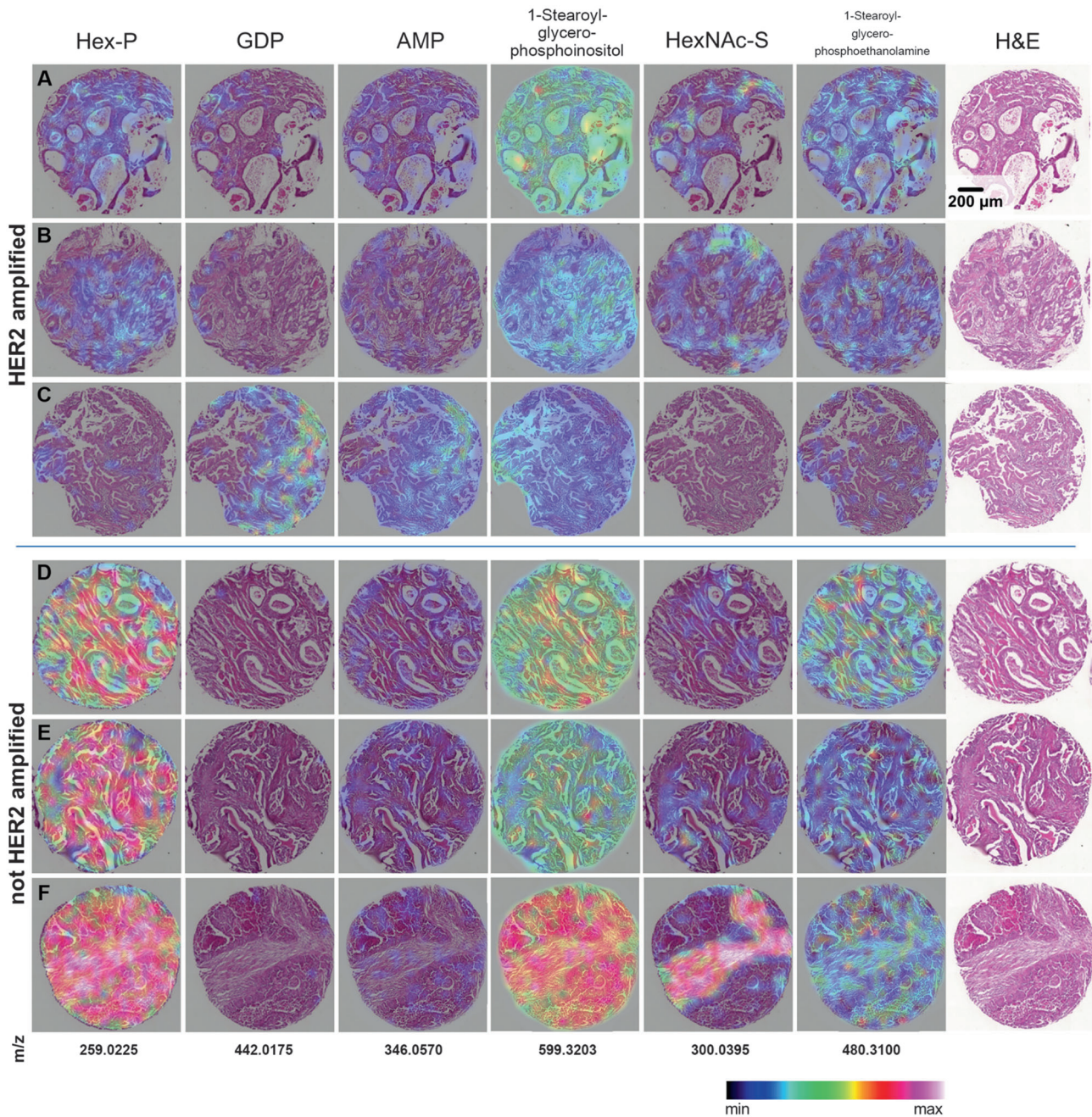
Fig. 4 A tissue microarray (TMA) containing 69 human gastro-esophageal adenocarcinoma samples was measured by MALDI FT-ICR metabolome imaging. Molecules, e.g., Hex-P (hexose phosphate), GDP (guanosine diphosphate), AMP (adenosine monophosphate), are visualized exemplarily on six tissue cores in heatmap coloring according to the biopsies, which are displayed in Fig. 2. The samples are either HER2 amplified (upper panel) or non-amplified (lower panel). Measured *m/z* values of the metabolites can be obtained from the last row. The panels **a**–**f** refer to the same tissue cores as shown in Fig. 5

Discussion

In this study, we developed a novel combined approach which, for the first time, allows the direct correlation of findings from MALDI imaging experiments and essential histological staining with the outcome of FISH analysis on the very same tissue section.

As example for the additional value of the method combination, we focused on measuring the AMP levels using MALDI metabolite imaging as a surrogate marker for the activity of AMP-activated kinase (AMPK), which is known to be stimulated by high AMP levels, which appear due to a lack of ATP in tumor metabolism [22]. AMPK is described to impact HER2 and has major influence on
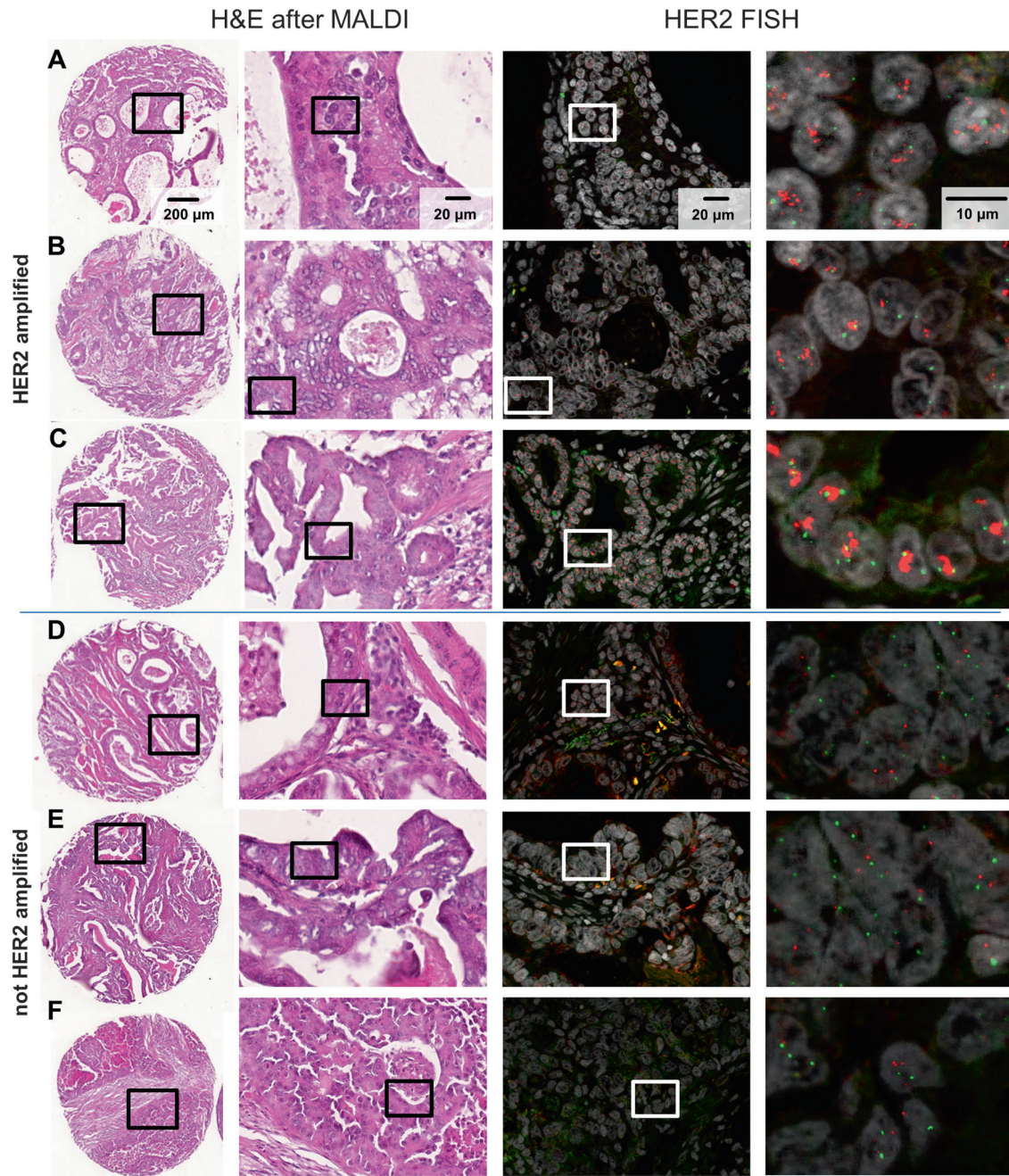
Fig. 5 After H&E staining, FISH analysis was performed on the very same TMA section. The HER2 gene locus carries a red fluorescence label, while the centromeric region of chromosome 17 is marked with a green fluorescence label. The nuclei are stained using Hoechst (gray). The cores shown in **a**, **b** show medium level HER2 gene amplification, whereas the core in **c** is a high-amplified tissue sample. The cores displayed in **d**, **e**, **f** are not amplified

tumor growth and progression [23, 27]. Jhaveri et al. [27] described a decreased activation of HER2 and EGFR caused by AMPK in human breast cancer cell lines and xenograft tumors. The mechanistical study in breast cancer cell lines showed that AMPK directly inhibits the activity of HER2 via phosphorylation. As AMPK is activated by an increased cellular AMP level [36], it could be, that an increased level of AMP can serve as a surrogate marker for

AMPK activity and thus it might also work as a predictor for tumor cell progression by indirectly reflecting the activity of HER2. Of note, our results are not able to provide a causal explanation of an impact of AMP to HER2 signaling.

As HER2 gene amplification and AMP mass intensity both have the ability to differ significantly between good and poor prognosis group in the Kaplan–Meier analysis

Fig. 6 a Kaplan–Meier survival analysis was performed using the parameters HER2/CEP17 signal ratio from FISH analysis. The image on the top right corner shows a HER2/CEP17 FISH sample with a non-amplified diploid state (image with red border) representative for good prognosis and on the lower right corner a sample with a HER2 gene amplification (image with blue border) for poor prognosis. **b** AMP mass signal intensity from the MALDI imaging approach is able to separate patient samples as a prognostic factor. Ion distribution maps showing localization of AMP in tissue cores representative for low-mass intensity (image with red border) and high-mass intensity (image with blue border). **c** The ratio of the mass intensity of AMP and the HER2/CEP17 signal ratio lead to significant improvement of survival analysis
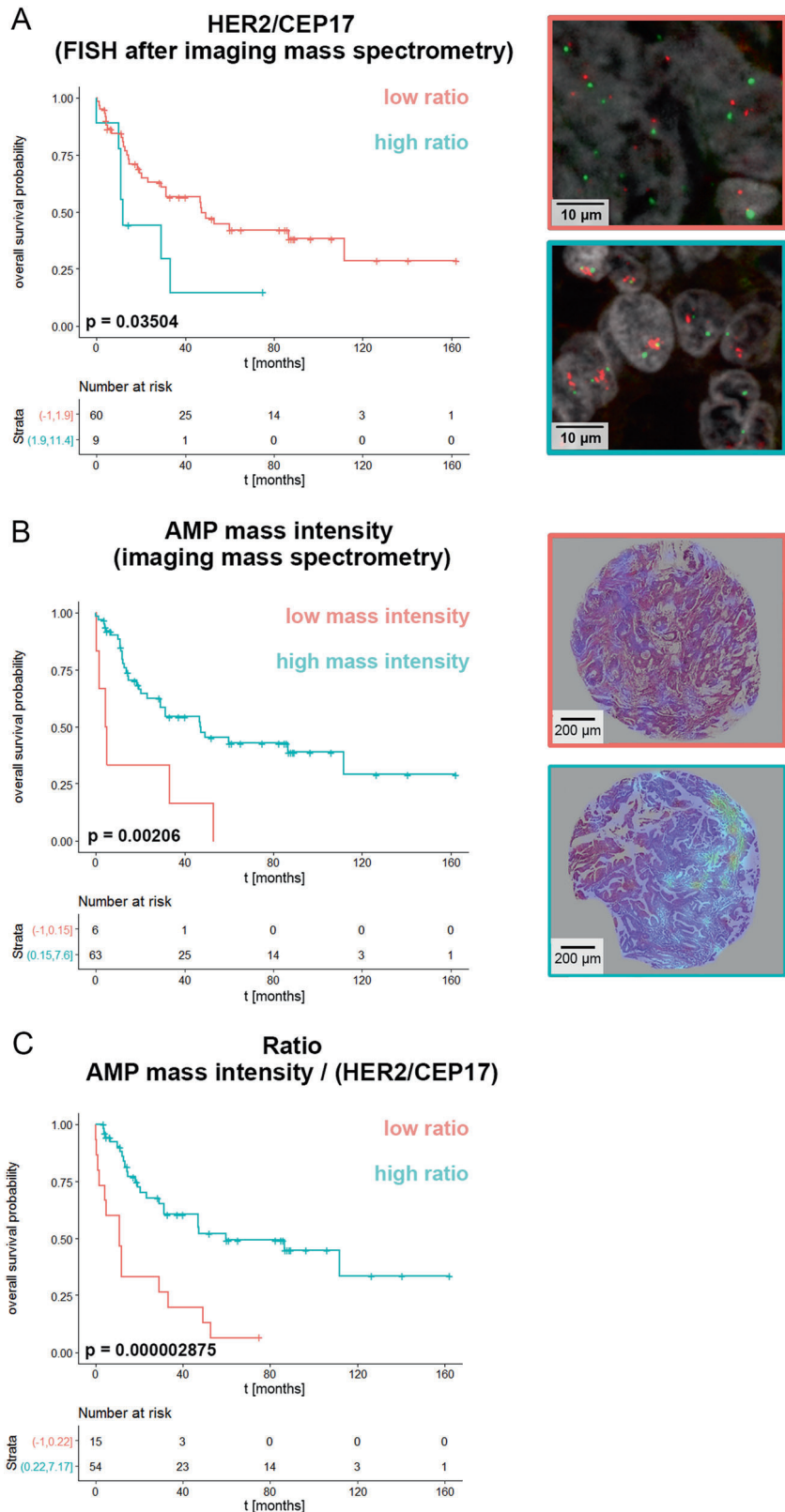
while not correlating to each other, the information of both parameters was combined as a ratio. Using this ratio it is possible to increase the significance level of the survival analysis to $p = 0.000002875$. Hereby it becomes obvious, that the information from the gene amplification analysis and the mass spectrometry imaging approach together sum

up to a very precise prognosis, which is strikingly better than each method alone. The correlation plot depicted in Supplementary Fig. 2 shows that HER2 signal count and AMP level do not correlate with each other. Another possibility might be the analysis of further molecules, which are involved in this or even other pathways of tumor progression. As MALDI imaging is widely used for the detection of proteins, it is another opportunity to combine protein measurements with FISH analysis in future studies.

This approach was established and validated using human gastroesophageal adenocarcinoma biopsies. A comparison of a FISH analysis after MALDI imaging with a reference FISH analysis without previous MALDI imaging using consecutive sections of the same biopsies was performed (Fig. 3 and Table 1). Hereby the results from both approaches revealed were similar. Most notably, after the performance of the whole protocol, cell structure is still preserved and FISH results remain as correct and reliable as when performed exclusively. This result highlights the robustness of well-prepared FFPE tissues, which proved to be an outstanding source of information.

Hence, we claim that our MALDI imaging protocol leaves the tissue intact and does not influence the outcome of subsequent FISH experiments.

We demonstrate that our protocol does not only keep the tissue structure intact, but, most remarkably, it even leaves the DNA structure unimpaired and thus the FISH approach remains unaffected by the foregoing procedure.

Our results are concordant with the work of Kazdal et al. [37], which shows the combination of MALDI imaging with digital PCR, although describing the robustness of the DNA structure even after undergoing the MALDI ionization procedure. Regarding the fact, that the molecules are ionized from the tissue by an UV laser beam, it is a notable finding that the DNA is still intact to allow reliable FISH results. A combination of IR spectroscopic imaging and MALDI imaging was recently described by Neumann et al. [38], enabling more advanced tissue analysis. Here, MALDI imaging measurement were carried out before the very same tissue was analyzed by IR spectroscopic imaging, as the gently ionization method did not destroy the tissue [38]. Owing to these findings and because we expect a loss of metabolites during the washing steps of the FISH protocol, we aimed to develop a protocol, which enables the performance of FISH analysis after the MALDI imaging procedure.

The described combined tissue analysis approach is established for tissue biopsies. As biopsies represent the standard material used in clinical diagnostics and our approach does not require further sections of the anyways limited material, our combined method is very suitable for the use in the clinical setting [39]. MALDI imaging was described as a promising tool for clinical diagnostics, as well as for clinical research [40, 41].

Our workflow consists of a new multimodal procedure of tissue analytics, which allows molecular feature extraction by mass spectrometry imaging, and phenotypic and cytogenetic feature extraction by digital image analysis, resulting in highly improved prognosis estimation. Thus, the overall information that can be gained from one tissue section is extended, and, in combination with clinical data, including survival and response, this combined workflow represents a promising tool for further biomarker research. Additionally, the present work shows the prognostic value of MALDI imaging. As disease prognosis is significantly improved by the addition of MALDI imaging data, the described multimodal method might have potential to improve response prediction as well.

Compliance with ethical standards

Conflict of interest The authors declare that they have no conflict of interest.

Publisher's note: Springer Nature remains neutral with regard to jurisdictional claims in published maps and institutional affiliations.

References

1. Wu M, Shu J. Multimodal molecular imaging: current status and future directions. Contrast Media Mol Imaging. 2018;2018:1382183.
2. Kircher MF, Mahmood U, King RS, Weissleder R, Josephson L. A multimodal nanoparticle for preoperative magnetic resonance imaging and intraoperative optical brain tumor delineation. Cancer Res. 2003;63:8122–5.
3. Takakusagi Y, Naz S, Takakusagi K, Ishima M, Murata H, Ohta K, et al. A multimodal molecular imaging study evaluates pharmacological alteration of the tumor microenvironment to improve radiation response. Cancer Res. 2018;78:6828–37.
4. Buchberger AR, DeLaney K, Johnson J, Li L. Mass spectrometry imaging: a review of emerging advancements and future insights. Anal Chem. 2018;90:240–65.
5. Schulz S, Becker M, Groseclose MR, Schadt S, Hopf C. Advanced MALDI mass spectrometry imaging in pharmaceutical research and drug development. Curr Opin Biotechnol. 2019;55: 51–9.
6. Buck A, Aichler M, Huber K, Walch A. In situ metabolomics in cancer by mass spectrometry imaging. Adv Cancer Res. 2017;134:117–32.
7. Kriegsmann K, Longuespee R, Hundemer M, Zgorzelski C, Casadonte R, Schwamborn K, et al. Combined immunohistochemistry

after mass spectrometry imaging for superior spatial information. Proteomics Clin Appl. 2019;13:e1800035.

8. Buck A, Ly A, Balluff B, Sun N, Gorzolka K, Feuchtinger A, et al. High-resolution MALDI-FT-ICR MS imaging for the analysis of metabolites from formalin-fixed, paraffin-embedded clinical tissue samples. J Pathol. 2015;237:123–32.

9. Boekhout AH, Beijnen JH, Schellens JH. Trastuzumab. Oncologist. 2011;16:800–10.

10. Lote H, Valeri N, Chau I. HER2 inhibition in gastro-oesophageal cancer: A review drawing on lessons learned from breast cancer. World J Gastrointest Oncol. 2018;10:159–71.

11. Bartley AN, Washington MK, Colasacco C, Ventura CB, Ismaila N, Benson AB, et al. HER2 testing and clinical decision making in gastroesophageal adenocarcinoma: guideline from the College of American Pathologists, American Society for Clinical Pathology, and the American Society of Clinical Oncology. J Clin Oncol. 2017;35:446–64.

12. Lordick F, Al-Batran SE, Dietel M, Gaiser T, Hofheinz RD, Kirchner T, et al. HER2 testing in gastric cancer: results of a German expert meeting. J Cancer Res Clin Oncol. 2017;143: 835–41.

13. Rauser S, Weis R, Braselmann H, Feith M, Stein HJ, Langer R, et al. Significance of HER2 low-level copy gain in Barrett's cancer: implications for fluorescence in situ hybridization testing in tissues. Clin Cancer Res. 2007;13:5115–23.

14. Hagemann IS. Molecular testing in breast cancer: a guide to current practices. Arch Pathol Lab Med. 2016;140:815–24.

15. Sauter G, Lee J, Bartlett JM, Slamon DJ, Press MF. Guidelines for human epidermal growth factor receptor 2 testing: biologic and methodologic considerations. J Clin Oncol. 2009;27:1323–33.

16. Burandt E, Sauter G. HER2-ASCO-guidelines. Der Pathologe. 2010;31:285–91.

17. Fu X, Zhang Y, Yang J, Qi Y, Ming Y, Sun M, et al. Efficacy and safety of trastuzumab as maintenance or palliative therapy in advanced HER2-positive gastric cancer. Onco Targets Ther. 2018;11:6091–100.

18. Suter TM, Procter M, van Veldhuisen DJ, Muscholl M, Bergh J, Carlomagno C, et al. Trastuzumab-associated cardiac adverse effects in the herceptin adjuvant trial. J Clin Oncol. 2007;25:3859–65.

19. de Azambuja E, Procter MJ, van Veldhuisen DJ, Agbor-Tarh D, Metzger-Filho O, Steinseifer J, et al. Trastuzumab-associated cardiac events at 8 years of median follow-up in the Herceptin Adjuvant trial (BIG 1-01). J Clin Oncol. 2014;32:2159–65.

20. Gomez-Martin C, Lopez-Rios F, Aparicio J, Barriuso J, Garcia-Carbonero R, Pazo R, et al. A critical review of HER2-positive gastric cancer evaluation and treatment: from trastuzumab, and beyond. Cancer Lett. 2014;351:30–40.

21. Van Cutsem E, Bang YJ, Feng-Yi F, Xu JM, Lee KW, Jiao SC, et al. HER2 screening data from ToGA: targeting HER2 in gastric and gastroesophageal junction cancer. Gastric Cancer. 2015;18:476–84.

22. DeBerardinis RJ, Chandel NS. Fundamentals of cancer metabolism. Sci Adv. 2016;2:e1600200.

23. Shackelford DB, Shaw RJ. The LKB1-AMPK pathway: metabolism and growth control in tumour suppression. Nat Rev Cancer. 2009;9:563–75.

24. Mihaylova MM, Shaw RJ. The AMPK signalling pathway coordinates cell growth, autophagy and metabolism. Nat Cell Biol. 2011;13:1016–23.

25. Lin SC, Hardie DG. AMPK: sensing glucose as well as cellular energy status. Cell Metab. 2018;27:299–313.

26. Baumann J, Kokabee M, Wong J, Balasubramaniyam R, Sun Y, Conklin DS. Global metabolite profiling analysis of lipotoxicity in HER2/neu-positive breast cancer cells. Oncotarget. 2018;9:27133–50.

27. Jhaveri TZ, Woo J, Shang X, Park BH, Gabrielson E. AMP-activated kinase (AMPK) regulates activity of HER2 and EGFR in breast cancer. Oncotarget. 2015;6:14754–65.

28. Benabdellah F, Touboul D, Brunelle A, Laprevote O. In situ primary metabolites localization on a rat brain section by chemical mass spectrometry imaging. Anal Chem. 2009;81:5557–60.

29. Miyamoto S, Hsu CC, Hamm G, Darshi M, Diamond-Stanic M, Decleves AE, et al. Mass spectrometry imaging reveals elevated glomerular ATP/AMP in diabetes/obesity and identifies sphingomyelin as a possible mediator. EBioMedicine. 2016;7:121–34.

30. Wang X, Han J, Hardie DB, Yang J, Pan J, Borchers CH. Metabolomic profiling of prostate cancer by matrix assisted laser desorption/ionization-Fourier transform ion cyclotron resonance mass spectrometry imaging using Matrix Coating Assisted by an Electric Field (MCAEF). Biochim Biophys Acta Proteins Proteom. 2017;1865:755–67.

31. Liu H, Li W, He Q, Xue J, Wang J, Xiong C, et al. Mass spectrometry imaging of kidney tissue sections of rat subjected to unilateral ureteral obstruction. Sci Rep. 2017;7:41954.

32. Cacciatore S, Zadra G, Bango C, Penney KL, Tyekucheva S, Yanes O, et al. Metabolic profiling in formalin-fixed and paraffin-embedded prostate cancer tissues. Mol Cancer Res. 2017;15:439–47.

33. Ly A, Buck A, Balluff B, Sun N, Gorzolka K, Feuchtinger A, et al. High-mass-resolution MALDI mass spectrometry imaging of metabolites from formalin-fixed paraffin-embedded tissue. Nat Protoc. 2016;11:1428–43.

34. Kunzke T, Balluff B, Feuchtinger A, Buck A, Langer R, Luber B, et al. Native glycan fragments detected by MALDI-FT-ICR mass spectrometry imaging impact gastric cancer biology and patient outcome. Oncotarget. 2017;8:68012–25.

35. Hicks DG, Tubbs RR. Assessment of the HER2 status in breast cancer by fluorescence in situ hybridization: a technical review with interpretive guidelines. Hum Pathol. 2005;36:250–61.

36. Hardie DG. AMP-activated protein kinase: an energy sensor that regulates all aspects of cell function. Genes Dev. 2011;25:1895–908.

37. Kazdal D, Longuespee R, Dietz S, Casadonte R, Schwamborn K, Volckmar AL, et al. Digital PCR after MALDI-mass spectrometry imaging to combine proteomic mapping and identification of activating mutations in pulmonary adenocarcinoma. Proteomics Clin Appl. 2019;13:e1800034.

38. Neumann EK, Comi TJ, Spegazzini N, Mitchell JW, Rubakhin SS, Gillette MU, et al. Multimodal chemical analysis of the brain by high mass resolution mass spectrometry and infrared spectroscopic imaging. Anal Chem. 2018;90:11572–80.

39. Longuespee R, Casadonte R, Schwamborn K, Reuss D, Kazdal D, Kriegsmann K, et al. Proteomics in pathology. Proteomics. 2018;18:1–7.

40. Kriegsmann J, Kriegsmann M, Casadonte R. MALDI TOF imaging mass spectrometry in clinical pathology: a valuable tool for cancer diagnostics (review). Int J Oncol. 2015;46:893–906.

41. Addie RD, Balluff B, Bovee JV, Morreau H, McDonnell LA. Current state and future challenges of mass spectrometry imaging for clinical research. Anal Chem. 2015;87:6426–33.

3.2. *De novo* discovery of metabolic heterogeneity with immunophenotype-guided imaging mass spectrometry

The next publication, entitled "*De novo* discovery of metabolic heterogeneity with immunophenotype-guided imaging mass spectrometry" [2], reveals the improved spatial metabolomics method. This publication presents the spatial correlation image analysis (SPACiAL) pipeline. The previous embedded publication in this thesis (see chapter 3.1) [1] illustrated the proof-of-principle for performing spatial metabolomics and *in situ* hybridization on the very same tissue section. However, there is so far no tool for integrating both modalities in a spatially resolved manner. Instead of averaging the information about gene copy number and metabolite quantities of one tissue specimen as presented in the previous publication (see chapter 3.1) [1], the SPACiAL pipeline improves this approach by providing a platform for the multimodal integration of spatially resolved data in the same tissue specimen by keeping the spatial information intact. The SPACiAL pipeline can integrate most spatially resolved data of a tissue section. For this publication, we have chosen multiplex immunohistochemistry (IHC) to demonstrate the advantages of the SPACiAL pipeline. We revealed for the first time the spatially resolved metabolic heterogeneity considering metabolites related to HER2 protein expression *in situ* in gastric cancer tissues. The presented SPACiAL pipeline illustrates an essential tool for all subsequent publications in this thesis [3, 4] and enables predictive biomarkers for anti-HER2 and anti-PD-1/PD-L1 therapy by allowing spatial information in different molecular layers (e.g., genomics, proteomics, metabolomics).

I am sharing the first authorship with my former colleague Verena M. Prade. I introduced the basic principle for combining the individual spatially resolved data sets of spatial metabolomics and immunohistochemical staining. I prepared figures and implemented the algorithms together with Verena M. Prade. In addition, I wrote the original draft of the manuscript together with Verena M. Prade and Achim Buck, and I co-designed this study together with Verena M. Prade, Achim Buck, and Axel Walch.

We also try to protect the idea behind this publication [2] by the following patent application:

- Walch A, Prade VM, **Kunzke T**, Buck A, Feuchtinger A. METHOD FOR AN AUTOMATIC, SEMANTIC-BASED, FUNCTIONAL TISSUE ANNOTATION OF HISTOLOGICAL AND CELLULAR FEATURES IN ORDER TO IDENTIFY MOLECULAR FEATURES IN TISSUE SAMPLES (2021), Luxemburg Patent Application LU101644, published 2021-08.

MOLECULAR
METABOLISM

De novo discovery of metabolic heterogeneity with immunophenotype-guided imaging mass spectrometry

Verena M. Prade [1,5], Thomas Kunzke [1,5], Annette Feuchtinger [1], Maria Rohm [2], Birgit Luber [3], Florian Lordick [4], Achim Buck [1,**], Axel Walch [1,*]

ABSTRACT

Background: Imaging mass spectrometry enables *in situ* label-free detection of thousands of metabolites from intact tissue samples. However, automated steps for multi-omics analyses and interpretation of histological images have not yet been implemented in mass spectrometry data analysis workflows. The characterization of molecular properties within cellular and histological features is done via time-consuming, non-objective, and irreproducible definitions of regions of interest, which are often accompanied by a loss of spatial resolution due to mass spectra averaging.

Methods: We developed a new imaging pipeline called *Spatial Correlation Image Analysis* (SPACiAL), which is a computational multimodal workflow designed to combine molecular imaging data with multiplex immunohistochemistry (IHC). SPACiAL allows comprehensive and spatially resolved *in situ* correlation analyses on a cellular resolution. To demonstrate the method, matrix-assisted laser desorption-ionization (MALDI) Fourier-transform ion cyclotron resonance (FTICR) imaging mass spectrometry of metabolites and multiplex IHC staining were performed on the very same tissue section of mouse pancreatic islets and on human gastric cancer tissue specimens. The SPACiAL pipeline was used to perform an automatic, semantic-based, functional tissue annotation of histological and cellular features to identify metabolic profiles. Spatial correlation networks were generated to analyze metabolic heterogeneity associated with cellular features.

Results: To demonstrate the new method, the SPACiAL pipeline was used to identify metabolic signatures of alpha and beta cells within islets of Langerhans, which are cell types that are not distinguishable via morphology alone. The semantic-based, functional tissue annotation allows an unprecedented analysis of metabolic heterogeneity via the generation of spatial correlation networks. Additionally, we demonstrated intra- and intertumoral metabolic heterogeneity within HER2/neu-positive and -negative gastric tumor cells.

Conclusions: We developed the SPACiAL workflow to provide IHC-guided *in situ* metabolomics on intact tissue sections. Diminishing the workload by automated recognition of histological and functional features, the pipeline allows comprehensive analyses of metabolic heterogeneity. The multimodality of immunohistochemical staining and extensive molecular information from imaging mass spectrometry has the advantage of increasing both the efficiency and precision for spatially resolved analyses of specific cell types. The SPACiAL method is a stepping stone for the objective analysis of high-throughput, multi-omics data from clinical research and practice that is required for diagnostics, biomarker discovery, or therapy response prediction.

© 2020 The Author(s). Published by Elsevier GmbH. This is an open access article under the CC BY-NC-ND license (http://creativecommons.org/licenses/by-nc-nd/4.0/).

1. INTRODUCTION

Computational automation of routine tasks and artificial intelligence guided analyses rapidly gain significance with the increasing amount of data generated from single tissue samples [1]. With the rise of digital pathology, a major objective for precision medicine is the integration of morphological and molecular imaging data from multi-omics studies [2]. Matrix-assisted laser desorption-ionization (MALDI) imaging mass spectrometry (IMS) can be used for *in situ* imaging of metabolites from frozen or formalin-fixed, paraffin-embedded (FFPE) tissue samples [3].

[1]Research Unit Analytical Pathology, Helmholtz Zentrum München — German Research Center for Environmental Health, Ingolstädter Landstraße 1, Neuherberg, 85764, Germany [2]Institute for Diabetes and Cancer, Helmholtz Zentrum München — German Research Center for Environmental Health, Ingolstädter Landstraße 1, Neuherberg, 85764, Germany [3]Institute of Pathology, Technische Universität München, Trogerstraße 18, München, 81675, Germany [4]University Cancer Center Leipzig (UCCL), University Medicine Leipzig, Liebigstraße 20, Leipzig, 04103, Germany

[5] Verena M. Prade and Thomas Kunzke contributed equally to this work.

*Corresponding author. E-mail: axel.walch@helmholtz-muenchen.de (A. Walch).

**Corresponding author. E-mail: achim.buck@helmholtz-muenchen.de (A. Buck).

Providing spatially resolved and label-free detection of hundreds to thousands of molecules within a single tissue section, MALDI imaging has proven to be an invaluable tool for digital histopathology. However, the spatial resolution of molecule distributions is often not fully utilized. For instance, cell- and tissue-specific structures, such as tumors, are frequently analyzed by manually annotating the respective areas on whole-slide images to mark so-called regions of interest (ROIs) [4]. The spatially resolved mass spectra in these regions are lost because only the mean or representative spectrum of each ROI is used for subsequent calculations. Such segmentation approaches fail to preserve molecular heterogeneity and spatial distribution, while whole-sample-based classifications fail for tissue sections comprised of cells belonging to different classes [5]. With the availability of tissue samples from large-scale clinical cohort studies, manual preprocessing steps can easily take weeks or months of work. Furthermore, manually annotating tumor regions is not only time-consuming, non-objective, and irreproducible, but also requires extensive histology knowledge that only expert pathologists possess. Additionally, it only permits the annotation of regions and cell types that are histologically distinguishable, while molecular alterations often do not manifest morphologically. Current efforts to utilize machine learning algorithms to automatically distinguish cell types [6] based on nothing more than hematoxylin and eosin tissue staining may work, for example, on tumor and stroma cells, but are not able to identify morphologically indistinguishable tumor subtypes.

Traditionally, when morphology alone is not sufficient, even clinical pathologists resort to immunohistochemistry (IHC) to localize proteins or peptides in a single tissue section [7]. Compared to efforts to define ROIs or distinguish cell types based on molecular distributions [8—10], immunostainings represent a method to precisely label specific cell types [11]. The technique is currently used to classify tumors or to perform structural tissue analyses to help pathologists establish a diagnosis [7]. IHC staining is commonly used for cell type labeling [12], but their potential for automated, semantic-based, functional tissue annotation and spatially resolved molecular analyses of heterogeneity is not fully utilized. In recent years, imaging mass spectrometry data and immunohistochemical staining have been successfully combined to increase the resolution of MALDI images [13] or to characterize individual dissociated cells [14], but no *in situ* tissue analysis with automatic identification of ROIs and data integration has been presented. While there is some software available for tissue image analysis, there currently is no method that integrates and analyzes the comprehensive molecular data from imaging mass spectrometry in combination with morphological, proteomic, and genetic information from other omics fields. The translation of imaging mass spectrometry into experimental clinical applications requires time-efficient data post-processing and comprehensive analyses of spatially resolved molecular information by avoiding expensive manual annotations or loss of resolution due to the generation of mean or representative spectra. In research, the use of immunostainings in combination with molecular data represent a significant improvement in scientific quality by solving the problem of time-consuming and irreproducible user-defined ROIs. In particular, the analysis of metabolic heterogeneity is hampered by pseudoheterogeneity originating from inaccuracies during manual annotation or by the use of consecutive tissue sections. The analysis of metabolic heterogeneity in tissues requires a strict coherence to consistent tissue and data preprocessing.

Here, we present our Spatial Correlation Image Analysis (SPACiAL) pipeline, a computational multimodal workflow to integrate molecular imaging mass spectrometry data with multiplex IHC staining from the very same tissue section to provide automated and reliable annotations and allow comprehensive and pixel-accurate correlation analyses of heterogeneity to combine data from multi-omics studies. The pipeline represents a starting point for the objective analysis of high-throughput data from clinical research and practice, which is required for tissue-based diagnostics and research.

To demonstrate the versatility and analytical power of the SPACiAL method, we deliberately chose two examples of molecular heterogeneity in both a physiological and a pathophysiological application: First, we performed a high-resolution analysis of islets of Langerhans in mouse pancreases. Phenotypic and functional beta cell heterogeneity has been shown to provide pancreatic islets with functional flexibility to adapt to physiological changes in the environment [15]. The metabolomic analysis of islet and islet cell heterogeneity requires *in situ* analyses of intact islets within tissue slices [16,17] and it has been insufficiently studied in their natural histological context. With SPACiAL, we distinguish alpha and beta cells and investigate the heterogeneity of different islets within one animal. Second, an analysis of tissue samples from patients with gastric cancer was carried out. The metabolomic, intratumoral, heterogeneous nature of the human epidermal growth factor receptor 2 (HER2/neu) is insufficiently studied *in situ*—especially in relation to gastric cancer—even though it is highly relevant for diagnostics and response to HER2/neu-based treatment. The SPACiAL pipeline was applied on tissue resection specimens and on a tissue microarray to distinguish HER2/neu-positive and -negative tumor cells and to investigate the molecular intra- and intertumoral heterogeneity. The multimodal approach utilizes pixel-wise molecular information to investigate metabolic heterogeneity via spatial correlation networks from cell populations automatically identified by multiplex immunohistochemical analysis.

2. METHODS

2.1. Tissue specimens and Fourier-transform ion cyclotron resonance (FTICR) MALDI IMS analysis

Pancreas/islets of Langerhans were obtained from a C57BL/6 N mouse and the sample was flash frozen in liquid nitrogen until measurement. The animal was provided *ad libitum* access to food and water. All animal studies were conducted in accordance with German animal welfare legislation and approved by the government of Upper Bavaria. FFPE tissue patient samples of gastric cancer were collected between 1995 and 2018 at the University of Leipzig and at the Department of Surgery, Klinikum Rechts der Isar, Munich, Germany. The resection specimens were processed in a highly standardized manner and fixed for 12—24 h in 10% neutral buffered formalin, followed by tissue dehydration and paraffin embedding with fully automated systems. The study was approved by the local Ethics Committees. All patients provided informed, signed consent.

Tissue preparation steps for MALDI imaging analysis was performed as previously described [3,18,19]. In brief, frozen (12 μm, Leica Microsystems, CM1950, Germany) and FFPE sections (4 μm, Microm, HM340E, Thermo Fisher Scientific, USA) were mounted onto indium-tin-oxide (ITO)-coated glass slides (Bruker Daltonik, Bremen, Germany) pretreated with 1:1 poly-L-lysine (Sigma Aldrich, Munich, Germany) and 0.1% Nonidet P-40 (Sigma). The air-dried tissue sections were spray-coated with 10 mg/ml of 9-aminoacridine hydrochloride monohydrate matrix (Sigma—Aldrich, Munich, Germany) in 70% methanol using the SunCollect™ sprayer (Sunchrom, Friedrichsdorf, Germany). Prior matrix application, FFPE tissue sections were incubated additionally for 1 h at 70 °C and deparaffinized in xylene (2 × 8 min). Spray-coating of the matrix was conducted in eight passes (ascending flow rates 10 μl/min, 20 μl/min, 30 μl/min for

layers 1—3, and layers 4—8 with 40 μl/min), utilizing 2 mm line distance and a spray velocity of 900 mm/min.

Metabolites were detected in negative-ion mode on a 7 T Solarix XR FTICR mass spectrometer (Bruker Daltonik) equipped with a dual ESI-MALDI source and a SmartBeam-II Nd: YAG (355 nm) laser. Data acquisition parameters were specified in ftmsControl software 2.2 and flexImaging (v. 5.0) (Bruker Daltonik). Mass spectra were acquired in negative-ion mode covering m/z 75—1,100, with a 1 M transient (0.367 s duration) and an estimated resolving power of 49,000 at m/z 200,000. The laser operated at a frequency of 1,000 Hz utilizing 200 laser shots per pixel with a pixel resolution of 15 μm (islets of Langerhans) and 60 μm (gastric cancer), respectively. ʟ-Arginine was used for external calibration in the ESI mode. On-tissue double mass spectrometry (MS/MS) was conducted on islets of Langerhans from the consecutive mouse pancreatic tissue section using continuous accumulation of selected ions' mode and collision-induced dissociation (CID) in the collision cell (Supplementary Figure 17). MS/MS spectra were analyzed by Bruker Compass DataAnalysis 5.0 (Build 203.2.3586).

2.2. Multiplex fluorescent immunohistochemical staining

After MALDI IMS analysis, 9-aminoacridine matrix was removed with 70% ethanol for 5 min from tissue sections followed by immunohistochemical staining. Pancreatic islets were analyzed by double staining for insulin [Insulin-monoclonal rabbit anti-insulin (1:800), catalog no. 3014, Cell Signaling Technology, Germany; AF750-goat anti-rabbit (1:100), catalog no. A21039, Thermo Fisher Scientific, US] and glucagon [polyclonal guinea pig anti-glucagon (1:3,000), catalog no. M182, Takara, USA; biotinylated goat anti-guinea pig immunoglobulin G (IgG, 1:100), catalog no. BA-7000, Vector Laboratories, US; streptavidin-Cy3, catalog no. SA1010, Thermo Fisher Scientific]. Double staining of human gastric cancer tissue specimens and a tissue microarray was performed using HER2 [polyclonal rabbit anti-human c-erbB-2 oncoprotein (1:300), catalog no. A0485, DAKO, CiteAb Ltd., UK] and pan-cytokeratin [monoclonal mouse pan cytokeratin plus [AE1/AE3+8/18] (1:75), catalog no. CM162, Biocare Medical, US]. Signal detection was conducted using fluorescence-labeled secondary antibodies [Goat Anti-rabbit IgG (H + L)-Cross-Adsorbed Secondary
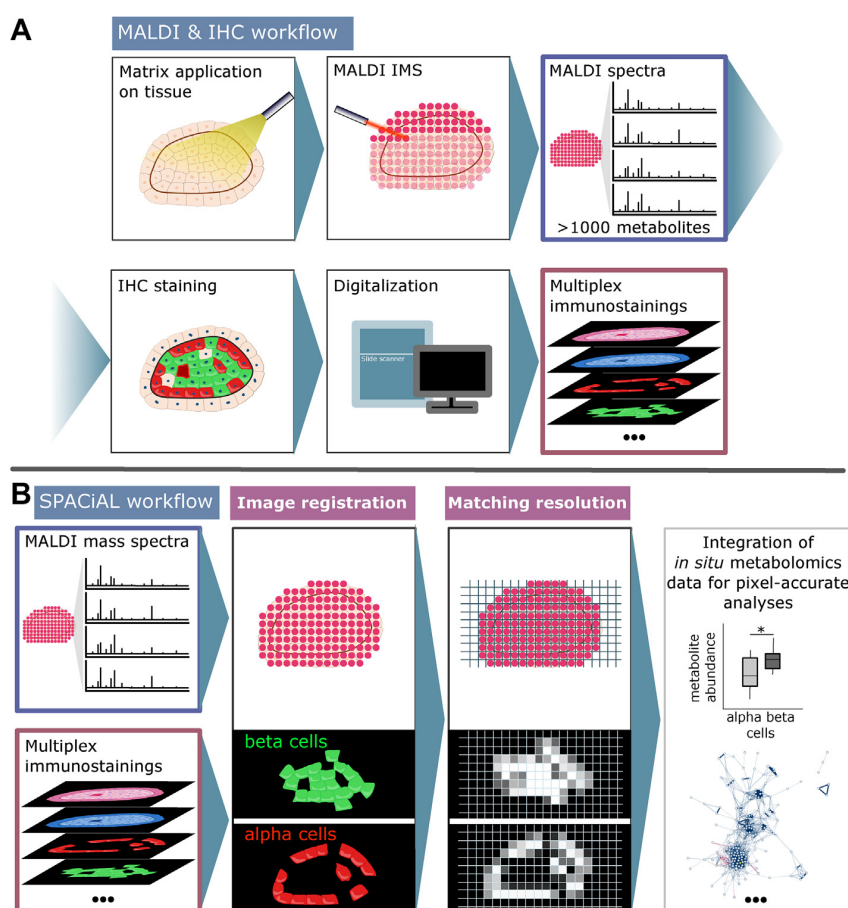

Figure 1: Workflow of immunohistochemistry-guided *in situ* metabolomics using the example of an islet of Langerhans. **A**: MALDI and IHC workflow starting with matrix application on tissue sections, MALDI imaging and data processing including peak picking and annotation. The matrix is then removed for subsequent multiplex immunohistochemical staining of the very same tissue section using DAPI, glucagon, and insulin. The individual stainings are digitized with a slide scanner. **B**: The SPACiAL pipeline integrates molecular MALDI data and immunohistochemical data. The IHC images need to be co-registered to the coordinates of the mass spectra per pixel. The MALDI data file is used to generate an image of the measurement region, which can be used for precise co-registration with the tissue image and tissue stainings. Once co-registered, the staining images are scaled to match the resolution of the measurement and color values per pixel are used for the definition of regions or for pixel-accurate analyses of metabolic correlations or heterogeneity.

Antibody-DyLight 633 (1:200), catalog no. 35563; and Goat Anti-Mouse IgG (H + L)-Cross-Adsorbed Secondary Antibody-Alexa Fluor 750 (1:100), catalog no. A-21037, both Thermo Fisher Scientific]. Nuclei were identified with Hoechst 33342 in all stainings. Fluorescence stainings were scanned with an AxioScan.Z1 digital slide scanner (Zeiss) equipped with a 20x magnification objective and visualized with the software ZEN 2.3 blue edition (Zeiss). Multi-images were exported as TIF files. Additionally, tissue sections were stained with hematoxylin and eosin after MALDI and IHC for internal visual validation.

2.3. Peak picking

The Bruker software flexImaging (v. 5.0) was used to export all root mean square normalized mass spectra as processed imzML files. An in-house python 3 pipeline was written to perform pixel-wise and parallelized peak picking. For each coordinate (i.e., spectrum), the peak picking pipeline began by resampling the mass (m/z) and intensity values between 75 and 1,100 Dalton (Da) with a step size of 0.0005 Da. Intensity values were resampled by choosing the maximum intensity per window. Noise levels were estimated for windows of 10 Da, and all peaks falling below their respective noise level were filtered. The noise level was calculated as 2.2 times the 85th percentile of the intensity values within the window. If fewer than 200 intensities fell within 1 window, which frequently happens in the higher mass range, then their neighboring windows are considered until at least 200 intensities can be used for the calculation. Since the noise level is expected to increase with the m/z value and to avoid extreme noise level fluctuations, the level of the first and last window were used as upper bounds. After noise-filtering, only local maxima were kept as preliminary peaks. Preliminary peaks within each spectrum were merged as previously described [18]. The merged peaks of all coordinates were then aligned, if their distance did not exceed $\left[\left(m/z\right) \times delta\_ppm\right] \div 1,000,000$ with $delta\_ppm = 2$. Peaks that occur in less than 0.5% of the spectra were filtered. Picked peaks were saved as an imzML file. Noise levels and the peak pickings were verified by manual inspection of random sample coordinates.

2.4. Metabolite annotation

The Human Metabolome Database [20] (HMDB, v. 4.0) was used to functionally annotate m/z values. The metabolite XML file was downloaded for offline use and a local PostgreSQL (v. 11) database was set up. Molecules were annotated by allowing M—H, M—H2O—H, M + Na—2H, M + Cl and M + K—2H as negative adducts with a mass tolerance of 4 ppm. A keyword search was performed on the description text to filter compounds with multiple annotations.

Specifically, compounds with indications of being drug-, plant-, food-, or bacteria-specific were filtered stringently.

2.5. Image co-registration

The imzML file of picked peaks was used to create a master image of the MALDI measurement region (imzML-grid). All additional images were precisely co-registered onto this image, allowing an exact integration and correlation of molecular MALDI data with immunostainings. The co-registration was done with the Landmark Correspondences plugin of FIJI ImageJ [21] (v. 1.52p). Alternatively, co-registration is also feasible with Adobe Photoshop CC 2019 or the GNU Image Manipulation Program (GIMP, v.2.10.8). A gray-scale tissue overview image and measurement points were exported with flexImaging (v. 5.0) and then fitted onto the master image. The integration of mass spectra and image data is done by co-registering the tissue scanned subsequent to MALDI imaging mass spectrometry and mapping the matrix ablation marks to the imzML-grid. The 4′,6-diamidino-2-phenylindole (DAPI) staining and all other stainings were finally fitted onto the precisely co-registered tissue image.

2.6. Region inclusion/exclusion criteria

After co-registration, all images had the exact same dimension and resolution. SPACiAL now offers the option to create a mask, where the user can manually label regions that should be excluded from subsequent analyses. Such regions may comprise tissue folds, swept away tissue, artifacts, or regions that are generally of no interest.

To integrate the data from all images, they have to be scaled to the exact MALDI measurement resolution by averaging the color values per x/y-coordinate. The IHC images are then converted into numerical matrices comprised of values corresponding to the lightness values for each pixel. SPACiAL can create images to allow validation of automatically defined ROIs (e.g., HER2/neu-positive tumor regions).

2.7. Pixel-accurate definition of HER2/neu-positive tumor regions

FFPE tissue sections of human gastric cancer samples were used to analyze the metabolic heterogeneity within HER2/neu-positive tumor regions. Tumor cells were annotated via the pan-cytokeratin staining. They were then classified as HER2/neu positive, if they also exhibited a positive signal in the HER2/neu staining. Otherwise, they were classified as HER2/neu-negative.

2.8. Networks

Correlation networks were created with Cytoscape [22] (v. 3.7.1). In all networks, nodes represent metabolites with node sizes corresponding to the mean intensity. Edges represent spatial
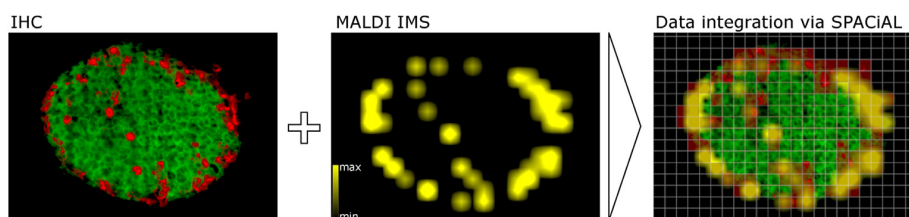

Figure 2: Multi-omics data integration via the SPACiAL method. Left: Islet of Langerhans with immunohistochemical staining (glucagon in red, insulin in green). Middle: Spatial distribution of 3-O Sulfogalactosylceramide (*m/z* 778.5147). Right: Data integration via SPACiAL, utilizing the IHC stainings to automatically identify alpha cells (semi-transparent, pixelated staining in red) and correlating metabolites. Lateral MALDI resolution (pixel): 15 μm.
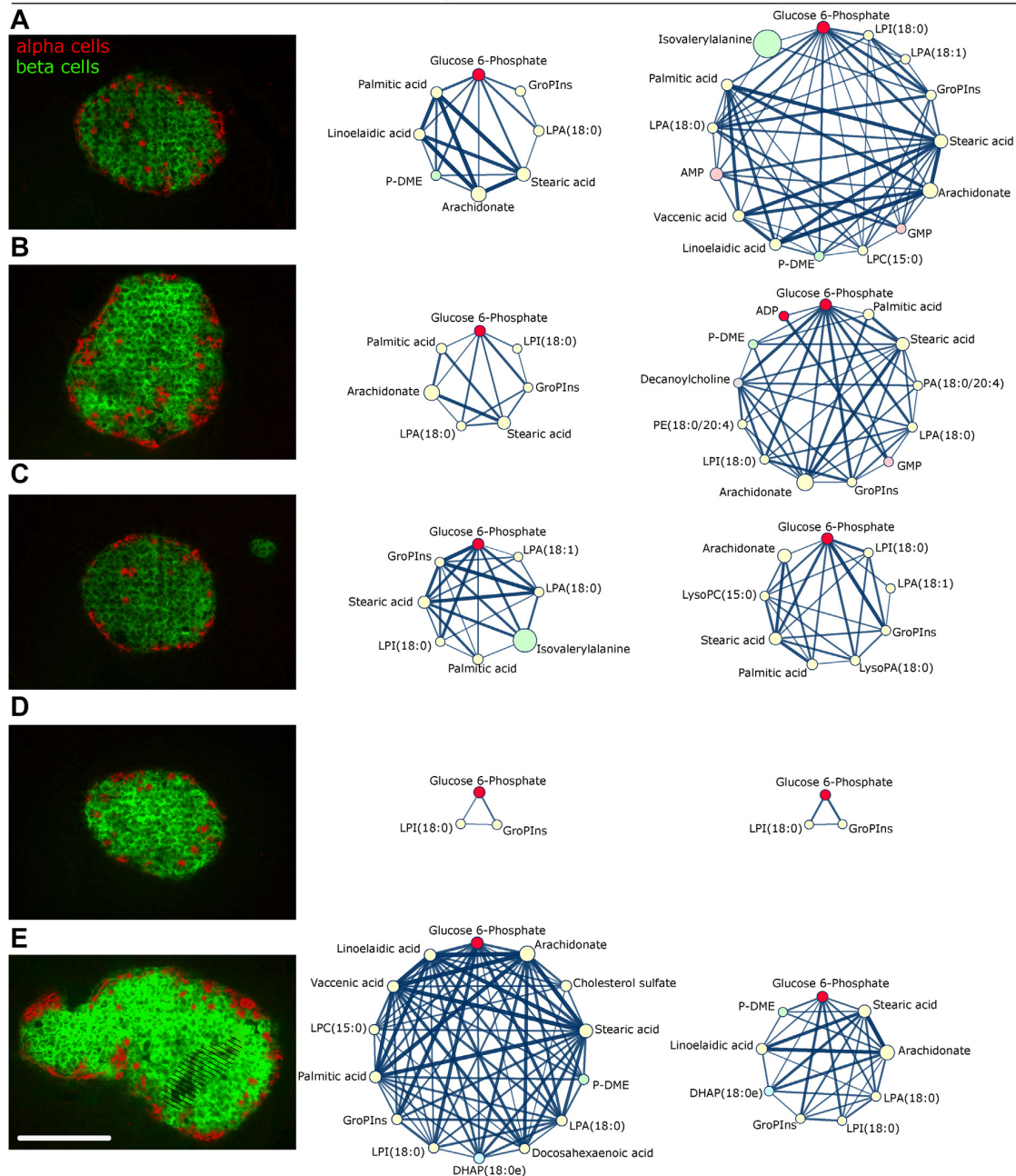
Figure 3: Metabolic heterogeneity within and between islets of Langerhans in a pancreatic tissue section of one mouse (A—E). The column on the left shows multiplex immunostainings after MALDI imaging mass spectrometry. Alpha cells (red) and beta cells (green) are stained with glucagon and insulin, respectively. A tissue fold in the fifth islet (E) was excluded from analyses (dashed). The second and third columns show spatial correlation networks for metabolites in alpha and beta cells, respectively. Nodes and edges represent compounds and their spatial correlation. The networks shown here only include direct neighbors of the glucose 6-phosphate node and edges representing a correlation coefficient of at least 0.7. Scale bar, 150 μm. Abbreviations: adenosine monophosphate (AMP), guanosine monophosphate (GMP), phosphatidic acid (PA), phosphatidylethanolamine (PE), lysophosphatidic acid (LPA), lysophospholipid (LPC), lysophosphatidylinositol (LPI), dihydroxyacetone phosphate (DHAP), glycerophosphoinositol (GroPIns), phosphodimethylethanolamine (P-DME).
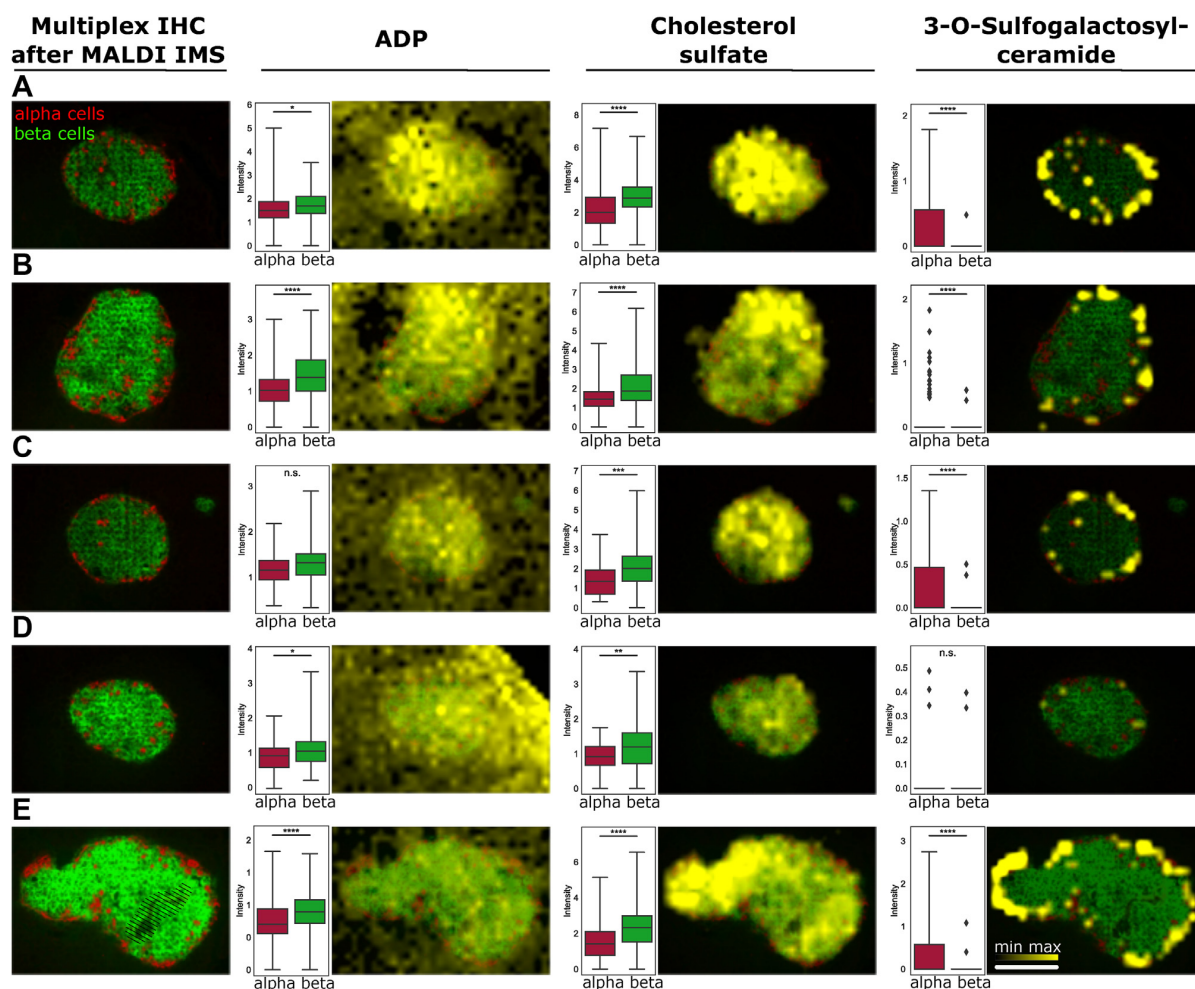
Figure 4: Multiplex immunohistochemistry-guided imaging mass spectrometry on islets of Langerhans to automatically distinguish morphologically indistinguishable cell types (A—E). Alpha and beta cells were stained with glucagon (red) and insulin (green), respectively. The spatial distributions of ADP, cholesterol sulfate and 3-O-sulfo-galactosylceramide (sulfatide) are visualized (yellow). Pixel-wise intensity distributions are shown for alpha (red) and beta cells (green), respectively. See the methods section for details about the statistical analysis. Scale bar, 150 μm.

correlations with line thickness and opacity increasing with the correlation coefficient. Nodes were colored red if their metabolites take part in glycolysis or they were colored depending on the molecule super class defined in HMDB [lipids and lipid-like molecules (yellow); nucleosides, nucleotides, and analogs (light red); organic acids and derivatives (green); organoheterocyclic compounds (lime green); alkaloids and derivatives (pink); organic oxygen compounds (blue); benzenoids (violet); phenylpropanoids and polyketides (orange); others (gray)]. All networks were either visualized using the yFiles circular layout or edge-weighted spring-embedded layout using the absolute value of the correlation coefficient. For the pancreatic islet cells, circular networks were generated by filtering edges with a coefficient smaller than 0.7 and by only visualizing direct neighbors of glucose 6-phosphate. All islets were located on the same tissue slide and were analyzed concurrently. The multiplex staining of the complete tissue is shown in Supplementary Figure 1. All remaining networks were generated by showing metabolites with at least one correlation

coefficient larger than 0.5, but without filtering edges. The complete networks are shown in Supplementary Figures 15 and 16. The multiplex staining of the complete tissues are shown in Supplementary Figures 8, 10, 12, and 14.

2.9. Statistical analyses
For the networks, pairwise Spearman rank-order correlations (Python 3.7, SciPy 1.2.0) were calculated between annotated metabolites using their intensities, and the resulting p-values were adjusted with Benjamini/Hochberg correction (Python 3.7, StatsModels 0.9.0). For the pancreatic islet cells, circular networks were generated by filtering edges with a coefficient smaller than 0.7. Network metrics (Supplementary Tables 1—3) were calculated using Cytoscape's plugin NetworkAnalyzer.

Metabolites localized predominantly on alpha or beta cells in islets of Langerhans were identified by using the Mann—Whitney U-test (Python 3.7, SciPy 1.2.0). The p-values were adjusted with Benjamini/Hochberg correction (Python 3.7, StatsModels 0.9.0). The number of
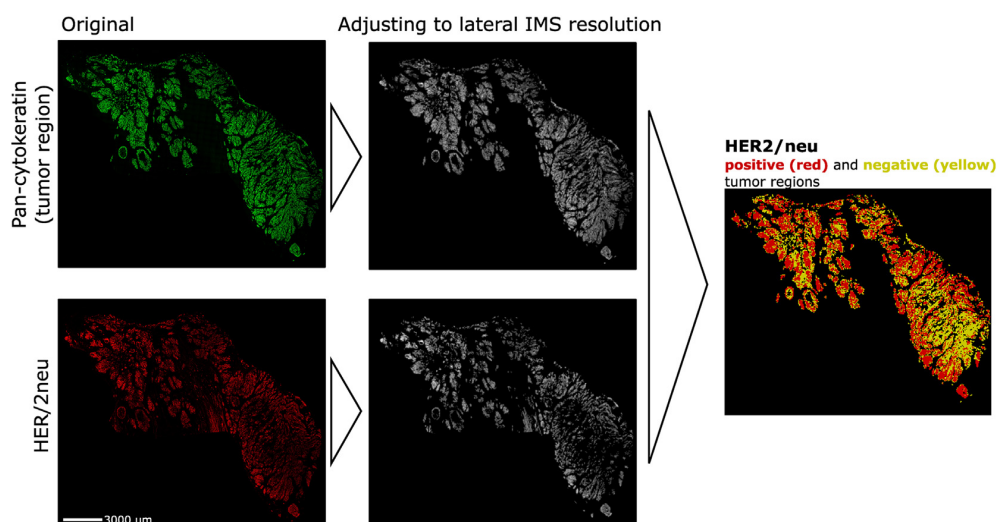
Figure 5: Image processing workflow to define HER2/neu positive and negative tumor regions. Pan-cytokeratin (green) as an epithelial marker to stain tumor cells. HER2/neu positive cells are shown in red. Both stainings are adjusted to match the lateral imaging mass spectrometry resolution (60 μm) and combined to classify HER2/neu positive and negative tumor cells. Scale bar, 3000 μm.

cell-type specific pixels per islet ranges between 59 and 194 for alpha cells and between 112 and 228 for beta cells. The Python 3.7 package NumPy 1.15.4 was used to calculate statistics for the intensity distributions of ADP, cholesterol sulfate, and 3-O-sulfogalactosylceramide in the islets of Langerhans (Supplementary Figures 5—7).

3. RESULTS AND DISCUSSION

3.1. The SPACiAL workflow for immunohistochemistry-guided imaging mass spectrometry

The SPACiAL pipeline comprises a series of MALDI data and image processing steps to combine molecular data with morphological and immunophenotypic information from IHC stainings or other imaging data. Immunostaining following MALDI imaging has previously been shown to be feasible [23,24]; hence the entire workflow works on the very same tissue section. Here, we have demonstrated that even multiplex immunostainings are entirely possible after MALDI imaging of the very same tissue section, which allows automatic data integration of morphological and spatially resolved *in situ* data of thousands of molecules via the SPACiAL method. The entire tissue and data pre-processing workflow preceding the application of the SPACiAL algorithm includes matrix coating of tissue sections, MALDI imaging, peak picking, matrix removal, IHC staining, and image digitalization, which is shown schematically for an islet of Langerhans with glucagon, insulin and DAPI staining (Figure 1A). SPACiAL then uses MALDI imaging files to create a reference image for subsequent co-registration of the molecular data with other image information (Figure 1B). The digitized and co-registered immunostaining images are scaled to match the exact MALDI resolution and then converted into numerical data without loss of spatial resolution. This ultimately allows pixel-accurate, objective tissue annotations based on semantics and function, which is shown here as an example for alpha and beta cells stained with glucagon (red) and insulin (green), respectively, and one metabolite (yellow) co-localizing with alpha cells (Figure 2). The SPACiAL pipeline paves the way for further statistical calculations and for the analysis of

tissue heterogeneity and previously infeasible molecular *in situ* analyses of cell subpopulations within intact tissue sections. To illustrate the versatility and analytical power of the SPACiAL pipeline, it was applied on two datasets; a physiological use case and a pathophysiological use case.

3.2. SPACiAL analysis of metabolic heterogeneity within and between islets of Langerhans

To demonstrate the SPACiAL pipeline, it was applied on islets of Langerhans in the pancreas of a wild-type mouse to distinguish the glucagon-releasing alpha and insulin-releasing beta cells and to investigate the heterogeneity of different islets within one animal. Previous studies highlight heterogeneity as a fundamental characteristic of pancreatic islets [25]. Beta cells are functionally heterogeneous and display different activity patterns in response to glucose stimulation or the ability to secret insulin [26]. The metabolic heterogeneity within automatically detected alpha and beta cells was analyzed in detail for the glucose metabolism. The islets of Langerhans — originating from one tissue section (Supplementary Figures 1—4) — were imaged with both high lateral (15 μm) and high mass resolution. Correlation networks were created to identify functional relationships of metabolites with glucose 6-phosphate and to assess metabolic heterogeneity within and between individual islets of Langerhans (Figure 3, Supplementary Table 1). Glucose 6-phosphate was chosen as a relevant example because it is an important intermediate in the glycolysis, gluconeogenesis, and pentose phosphate pathways.

Clear differences regarding network size were found between the islets and islet cell populations, reflecting differential metabolic states (Figure 3). For example, the alpha and beta cell network of the islet in Figure 3D indicates a low dependency on glucose metabolism, with only two metabolites showing a significant correlation to glucose 6-phosphate. Within networks from other islets, a variety of metabolites, including lipids, nucleotides, amino acid, and analogs, correlate with glucose 6-phosphate (Figure 3). The highest number of correlations were found in beta and alpha cell populations of the islets A and E, respectively, indicating a high dependency on glucose metabolism.
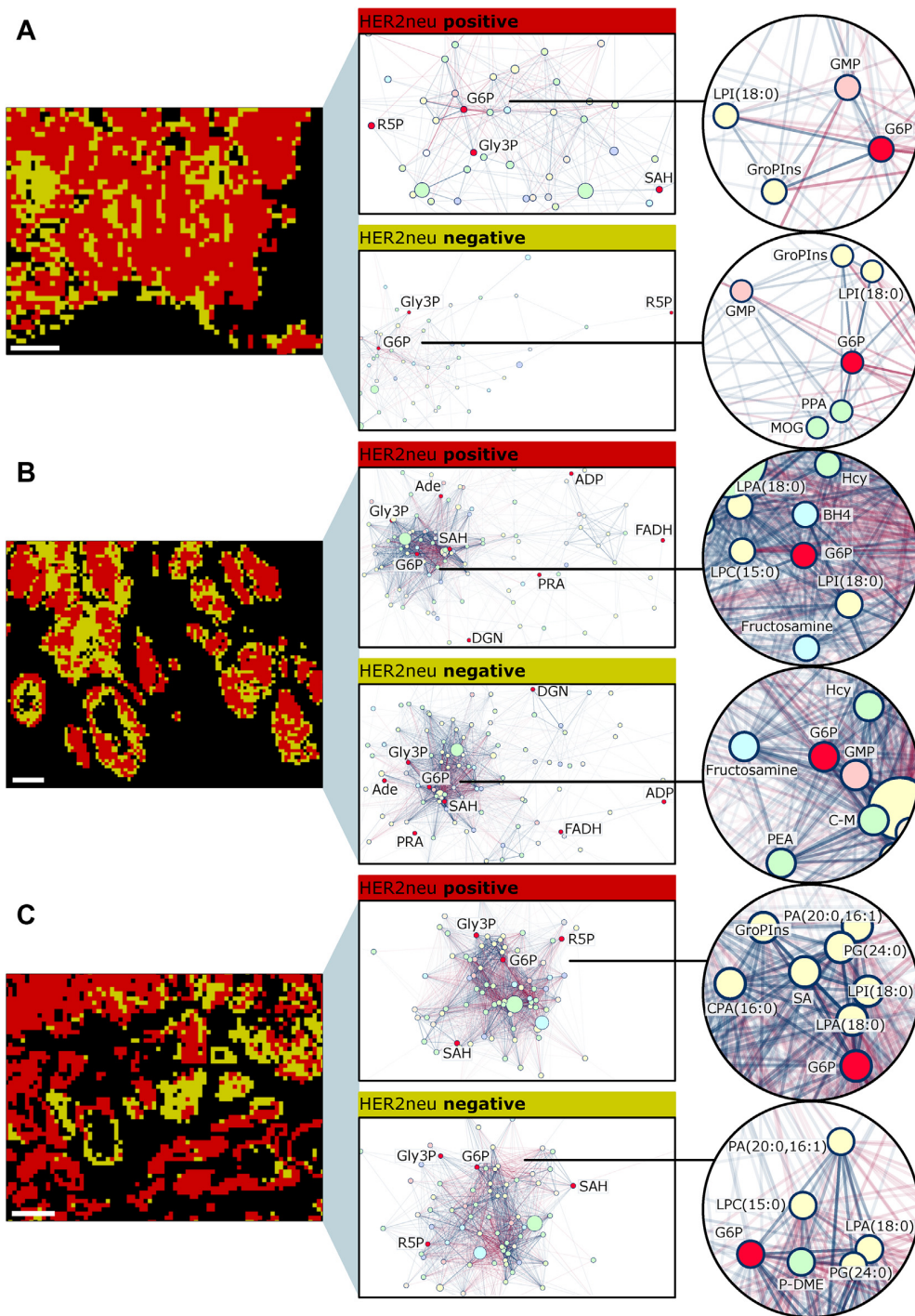
Figure 6: Intratumoral heterogeneity of spatially correlating metabolites in three human gastric cancer tissue sections, visualized via spatial correlation networks (A—C). Left: Close-up of the HER2/neu positive (red) and negative (yellow) tumor regions. Middle: Spatial correlation networks for metabolites. Edges represent positive (blue) and negative (red) spatial correlations between metabolites. Line thickness and transparency correspond to the correlation coefficient. Right: Zoom-in to glucose 6-phosphate. Abbreviations: glucose 6-phosphate (G6P), glycerol 3-phosphate (Gly3P), ribose 5-phosphate (R5P), S-adenosylhomocysteine (SAH), glycerophosphoinositol (GroPIns), adenosine diphosphate (ADP), guanosine monophosphate (GMP), adenine (Ade), 5-phosphoribosylamine (PRA), reduce flavin adenine dinucleotide (FADH), D-glutamine (DGN), cysteinyl-methionine (C—M), homocysteine (Hcy), phosphatidic acid (PA), phosphatidylglycerol (PG), cyclic phosphatidic acid (CPA), lysophosphatidic acid (LPA), lysophospholipid (LPC), lysophosphatidylinositol (LPI), phosphodimethylethanolamine (P-DME), phosphopantothenate (PPA), dimethyl-2-oxoglutarate (MOG), tetrahydrobiopterin (BH4), O-phosphoetha-nolamine (PEA), stearic acid (SA). Scale bar, 600 μm.

Table 1 — Network metrics for the glucose 6-phosphate node. Sample identifiers (A, B and C) correspond to the samples in Figure 6. The degree of a node represents the number of neighbors in the network. The average shortest path length is the average, minimum number of edges between glucose 6-phosphate node and any other node. The clustering coefficient is a measure for the connections between neighboring nodes.

Sample	HER2/neu state	Degree	Average shortest path length	Clustering coefficient
A	positive	27	1.697	0.285
A	negative	22	1.942	0.398
B	positive	54	2.012	0.721
B	negative	55	1.964	0.689
C	positive	62	1.294	0.733
C	negative	41	1.5	0.472

The spatial distribution of lipid-associated compounds, such as palmitic acid, stearic acid, lysophosphatidylinositol (LPI), and lysophosphatidic acid (LPA) were found to be correlated almost consistently. Other compounds, such as phosphodimethylethanolamine (P-DME) or glycerophosphoinositol (GroPIns), were found to inconsistently correlate with glucose 6-phosphate.

Metabolic signatures related to specific cell types and subpopulations can now easily be extracted with SPACiAL. Alpha and beta cells were defined automatically as ROIs, and metabolic differences between alpha and beta cells were assessed. Significant differences were detected for adenosine diphosphate (ADP), cholesterol sulfate, and 3-O-sulfogalactosylceramide (Figure 4). The presence of ADP, cholesterol sulfate, and 3-O-sulfogalactosylceramide was validated via MALDI FTICR on-tissue MS/MS using quadrupole collision-induced dissociation and comparison to standard compounds (Supplementary Figure 17). Not all islets reveal similar significant changes, also reflecting inter- and intra-islet metabolic heterogeneity. For instance, across four of the five measured islets, significantly higher ADP levels were detected in beta cells in comparison to alpha cells. Thus, the SPACiAL pipeline paves the way for *in situ* analyses of individual energy conditions of alpha and beta cells in each islet due to adenine nucleotide measurements. Cholesterol sulfate was found abundantly in beta cells, but it also exhibits a strong heterogeneous distribution between islets and even within cells of the same islet. Cholesterol sulfate is a component of the cell membrane [27] and in pancreatic beta cells, elevated intracellular cholesterol levels have been associated with reduced insulin secretion in mice [27,28]. Correlating with alpha cells, we found the 3-O-sulfogalactosylceramide. Sulfatides are glycosphingolipids which have been described in pancreatic islets with different abundances in alpha and beta cells [29—31].

Finally, pronounced molecular heterogeneity, both within single and between different islets of Langerhans, is reflected by a varying distribution of metabolite abundances (Supplementary Figures 5—7). Between islets and between cell types, the standard deviation of metabolite intensities differs by a factor of between 2.28 and 14.25 (ADP 0.32—0.73, cholesterol sulfate 0.5—1.52; 3-O-sulfogalactosylceramide 0.04—0.57). Hence, even individual cells within one islet exhibit different metabolite compositions, possibly reflecting different metabolic or cell differentiation states.

The *in situ* analysis of metabolic heterogeneity within pancreatic islets is just one potential field of application for the SPACiAL pipeline. Metabolic data together with detailed spatial information can be exploited to assess the extent and modulation of alpha and beta cells *in situ*. Because both insulin and glucagon are dysregulated in pathophysiological conditions, such as diabetes, our pipeline is valuable for future studies. The analysis of different subpopulations of islets of Langerhans can help to illuminate underlying phenotypic mechanisms to expand our knowledge of cell function and develop new therapeutic strategies.

3.3. Intratumoral metabolic heterogeneity in gastric cancer

The SPACiAL strategy has been shown to be powerful for close-to single-cell analyses of the metabolome in tissues of animal models, but it is also valuable for clinically relevant tissue analyses regarding diagnostics, prognosis, and therapy response prediction. For this reason, we applied the SPACiAL pipeline for the analysis of intra- and intertumoral heterogeneity in gastric cancer. While we used glucagon and insulin to stain alpha and beta cells within a frozen pancreatic tissue section, here we used pan-cytokeratin as an epithelial marker to stain tumor cells and HER2/neu for tumor cell classification within human FFPE tissue sections.

In gastric cancer, intratumoral HER2/neu heterogeneity is frequent, but its clinical significance remains open in terms of treatment with trastuzumab-chemotherapy [32—38]. The investigation of HER2/neu heterogeneity in gastric cancer in relation to the metabolic state of tumors is completely unexplored and may contribute to the improvement of treatment success. The SPACiAL pipeline was applied on tissue samples from three patients with gastric cancer to evaluate metabolic heterogeneity depending on the HER2/neu state. SPACiAL automatically determines the HER2/neu-positive and -negative tumor regions in a standardized way by evaluating expression values both in quantity on the basis of pixel intensity and localization by pixel co-localization (Figure 5). Regions displaying both pan-cytokeratin and HER2/neu signals are defined as HER2/neu-positive tumor regions, while regions displaying only a pan-cytokeratin signal are classified as HER2/neu-negative. Whole slide immunohistochemical stainings and regions defined as HER2/neu-positive (red) and -negative (yellow) are shown in Supplementary Figures 8—13. The pixel-accurate annotation allows an unprecedented analysis of metabolic heterogeneity within tumor cells based on metabolic correlation networks that were calculated for annotated metabolites detected and stringently filtered from gastric cancer tissue sections (Figure 6). For visualization purposes, a zoom-in of HER2/neu-positive and -negative tumor regions of Supplementary Figures 9, 11, and 13 is shown.

Since glucose plays a major role in altered energy metabolism in cancer [39], focusing on captured glucose as glucose 6-phosphate in the analysis of correlation networks provides insight into the complexity of the tumor biology regarding HER2/neu status. The spatial correlation networks comprise 67 to 171 metabolites (Supplementary Table 2) in HER2/neu-positive or -negative tumor regions, revealing intratumoral heterogeneity (Figure 6A—C). The number of correlating metabolites was identified in samples A and C, but the number and strength of pairwise spatial correlations differed, leading to different network structures; in particular, the network density is higher in C by a factor of approximately four (Supplementary Table 2). A majority of the correlating metabolites belong to the class of lipids and lipid-like molecules. In HER2/neu-positive regions of all patients, lysophosphatidylinositole (LPI) abundance correlates positively with glucose 6-phosphate. LPI is a bioactive lipid produced by the phospholipase A family, which is believed to play an essential role in several physiological and pathological processes [40]. As a ligand for the G-protein-coupled receptor GPR55, LPI may increase the glycolytic activity, since a GPR55 antagonist was shown to decrease glycolytic activity in cancer cell lines [41]. In one sample, glucose 6-phosphate formed a cluster together with numerous lipids (Figure 6C), while in the other two
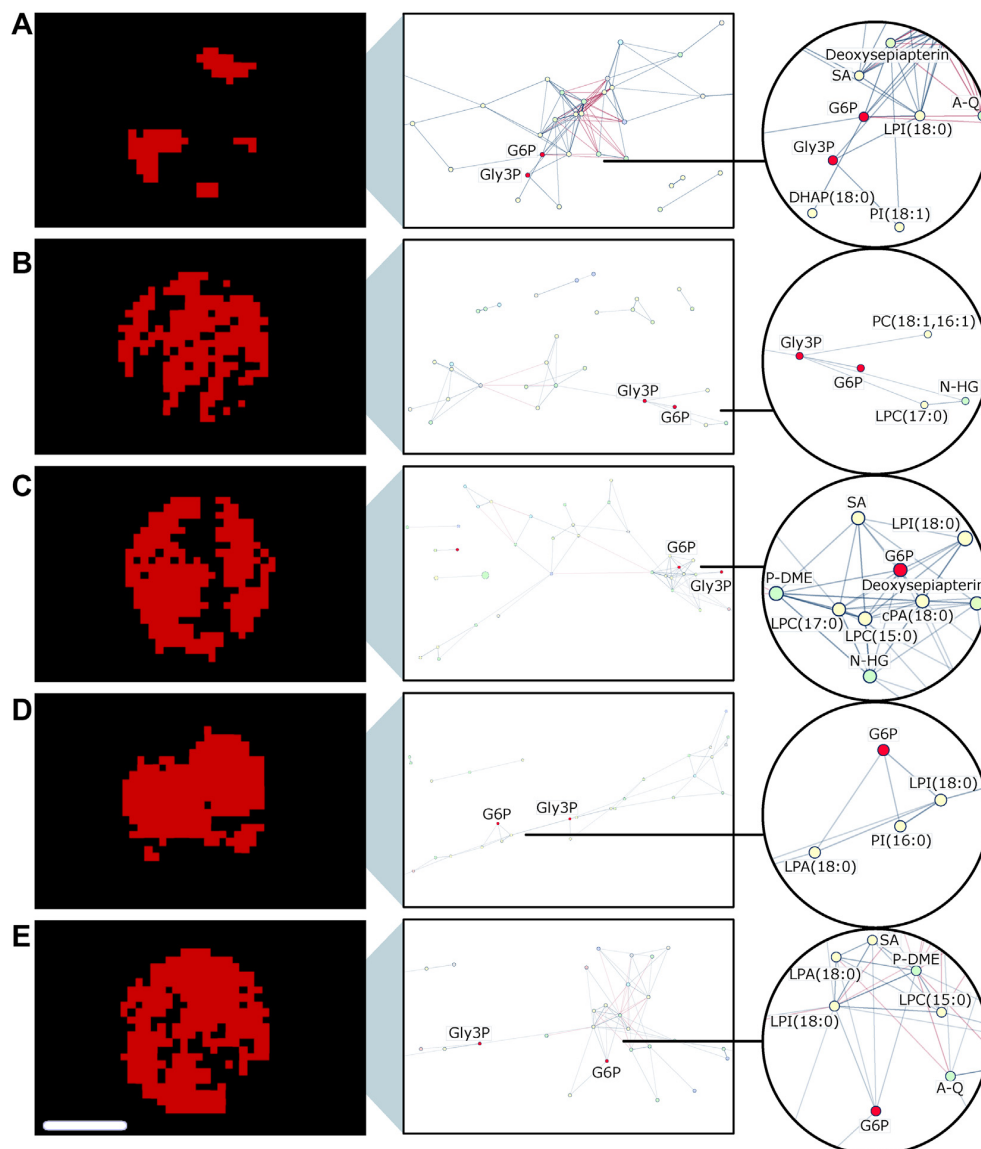
Figure 7: Intertumoral heterogeneity of metabolites in five tissue cores from HER2/neu positive patients with gastric cancer, visualized via spatial correlation networks (**A**–**E**). Edges represent positive (blue) and negative (red) spatial correlations between metabolites. Line thickness and transparency correspond to the correlation coefficient. Right: Zoom-in to glucose 6-phosphate. Abbreviations: glucose 6-phosphate (G6P), glycerol 3-phosphate (Gly3P), phospholipid (PC), phosphatidylinositol (PI), cyclic phosphatidic acid (CPA), lysophosphatidic acid (LPA), lysophospholipid (LPC), lysophosphatidylinositol (LPI), phosphodimethylethanolamine (P-DME), stearic acid (SA), dihydroxyacetone phosphate (DHAP), alanylglutamine (A–Q), histidinyl-glycine (N-HG). Scale bar, 600 μm.

samples, the neighboring nodes belonged to different metabolic classes — including carbohydrates, dipeptides and glycosylamines (Figure 6A,B). The intratumoral heterogeneity was most prominent in tumor sample C, reflected by the difference in degree, average shortest path length, and clustering coefficient of HER2/neu-positive and -negative metabolic networks (Figure 6 and Table 1). Overall, the degree and clustering coefficient of the glucose 6-phosphate node varies more strongly between patient samples, than between HER2/ neu-positive and -negative tumor regions within individual patient samples, reflecting intertumoral heterogeneity (Table 1).

3.4. Intertumoral metabolic heterogeneity in gastric cancer

To additionally demonstrate the compatibility of SPACiAL for high-throughput multiplex phenotyping, metabolic correlation networks were created for gastric cancer patient tissues from an FFPE tissue microarray (Figure 7A–E). Networks on the extracted HER2/neu-positive tumor regions of 5 gastric cancer patients comprised 30 to 39 metabolites and exhibited diverse correlation patterns. Similar to the results from whole gastric cancer resection specimens, most of the correlating metabolites are lipids. An altered lipid metabolism has been described previously

in a HER2/neu-positive breast cancer model [42]. Thus, a changed lipid metabolism may be associated with a high positive correlation of individual lipids to glucose 6-phosphate in human gastric cancer patients.

The diversity between metabolic correlation networks in individual patients demonstrates high intertumoral heterogeneity of HER2/neu-positive gastric cancer tissue (also see network metrics in Supplementary Table 3). The novel pipeline is a starting point for intra- and intertumoral heterogeneity analyses, enabling simultaneous analysis of distinct tissue and cellular compartments. The spatially resolved information from the molecular analysis has been used in our study to generate correlation networks between metabolites within ROIs that are automatically defined by immunohistochemical staining.

4. CONCLUSIONS

Our SPACiAL workflow integrates molecular MALDI imaging mass spectrometry data with IHC staining to facilitate automatic, reliable, and pixel-accurate annotation of specific cell types. In this context, the phenotypical information provided by IHC complements *in situ* molecular information for cell type-specific evaluation. The pipeline was demonstrated for both physiological and pathophysiological applications to investigate metabolic heterogeneity in alpha and beta cells from islets of Langerhans of a mouse model and in HER2/neu-positive tumor cells from patients with gastric cancer.

Glucagon-releasing alpha and insulin-releasing beta cells of different pancreatic islets within one animal were automatically annotated, demonstrating the basic functionality of the SPACiAL pipeline as a tool for objective IHC-guided annotation of otherwise histologically indistinguishable cell types. The pixel-accurate annotation and analysis of metabolites allows previously infeasible assessments of metabolomic heterogeneity between islets of Langerhans. Additionally, tissue samples from patients with gastric cancer were chosen to demonstrate the methodological advantages of SPACiAL for the analysis of intra- and intertumoral heterogeneity. The SPACiAL strategy can be extended by integrating other *in situ* datasets from tissue analytic platforms, since all spatially resolved information of a tissue section can be integrated in this pipeline (e.g., morphometrics, fluorescence *in situ* hybridization, and imaging mass cytometry). Prospectively, the application can also be useful for the automatic readout of regions of interest for metabolite quantification on an absolute, rather than on a relative scale. Quantification is a major topic of investigation in the targeted MALDI IMS field concentrating on the analysis of a subset of metabolites. Furthermore, the workflow was demonstrated to be compatible with both frozen and FFPE tissue samples. With SPACiAL, hundreds of distinct samples within tissue microarrays can be analyzed simultaneously. In contrast to the traditional analysis of mean spectra per ROI, SPACiAL allows in-depth and full use of available data without loss of resolution. With the spatial correlation networks of metabolites and the comparative approach to investigate islet cell heterogeneity, we demonstrate one of the many possibilities to utilize MALDI data. Combining the data from multi-omics studies, the pipeline represents an important starting point for the objective analysis of high-throughput data from large-scale clinical cohort studies, which are required for artificial intelligence-guided diagnostics, biomarker discovery, or therapy prediction.

We expect that further development of computational techniques for automatic feature identification based on multi-parameter molecular imaging data will remain an important area of ongoing investigation, and the results we present provide a useful framework and resource for advancing future studies.

DATA AVAILABILITY

Imaging mass spectrometry data for mouse pancreatic islets of Langerhans are provided at Zenodo.org (DOI:10.5281/zenodo.3607915) [43].

DECLARATION OF INTEREST

The authors declare no conflicts of interest.

APPENDIX A. SUPPLEMENTARY DATA

Supplementary data to this article can be found online at https://doi.org/10.1016/j.molmet.2020.01.017.

REFERENCES

[1] Colling, R., Pitman, H., Oien, K., Rajpoot, N., Macklin, P., Snead, D., et al., 2019. Artificial intelligence in digital pathology: *a roadmap to routine use in clinical practice*. The Journal of Pathology: Path, 5310. https://doi.org/10.1002/path.5310.

[2] Huang, S., Chaudhary, K., Garmire, L.X., 2017. More is better: recent progress in multi-omics data integration methods. Frontiers in Genetics 8(JUN):1—12. https://doi.org/10.3389/fgene.2017.00084.

[3] Buck, A., Ly, A., Balluff, B., Sun, N., Gorzolka, K., Feuchtinger, A., et al., 2015. High-resolution MALDI-FT-ICR MS imaging for the analysis of metabolites from formalin-fixed, paraffin-embedded clinical tissue samples. The Journal of Pathology 237:123—132. https://doi.org/10.1002/path.4560.

[4] Aeffner, F., Zarella, M., Buchbinder, N., Bui, M., Goodman, M., Hartman, D., et al., 2019. Introduction to digital image analysis in whole-slide imaging: a white paper from the digital pathology association. Journal of Pathology Informatics 10(1):9. https://doi.org/10.4103/jpi.jpi_82_18.

[5] Inglese, P., Correia, G., Pruski, P., Glen, R.C., Takats, Z., 2019. Colocalization features for classification of tumors using desorption electrospray ionization mass spectrometry imaging. Analytical Chemistry 91(10):6530—6540. https://doi.org/10.1021/acs.analchem.8b05598.

[6] Bulten, W., Bándi, P., Hoven, J., van de Loo, R., Lotz, J., Weiss, N., et al., 2019. Epithelium segmentation using deep learning in H&E-stained prostate specimens with immunohistochemistry as reference standard. Scientific Reports 9(1):1—10. https://doi.org/10.1038/s41598-018-37257-4.

[7] Ahmed, M., Broeckx, G., Baggerman, G., Schildermans, K., Pauwels, P., Van Craenenbroeck, A.H., et al., 2019. Next-generation protein analysis in the pathology department. p. 1—6. https://doi.org/10.1136/jclinpath-2019-205864.

Original Article

[8] Alexandrov, T., 2012. MALDI imaging mass spectrometry: statistical data analysis and current computational challenges. BMC Bioinformatics 13(Suppl 1). https://doi.org/10.1186/1471-2105-13-s16-s11 (Suppl 16).

[9] Jansson, E.T., Comi, T.J., Rubakhin, S.S., Sweedler, J.V., 2016. Single cell peptide heterogeneity of rat islets of Langerhans. ACS Chemical Biology 11(9): 2588—2595. https://doi.org/10.1021/acschembio.6b00602.

[10] Prentice, B.M., Hart, N.J., Phillips, N., Haliyur, R., Judd, A., Armandala, R., et al., 2019. Imaging mass spectrometry enables molecular profiling of mouse and human pancreatic tissue. Diabetologia 62(6):1036—1047. https://doi.org/10.1007/s00125-019-4855-8.

[11] Feuchtinger, A., Stiehler, T., Jütting, U., Marjanovic, G., Luber, B., Langer, R., et al., 2014. Image analysis of immunohistochemistry is superior to visual scoring as shown for patient outcome of esophageal adenocarcinoma. Histochemistry and Cell Biology 143(1):1—9. https://doi.org/10.1007/s00418-014-1258-2.

[12] Brieu, N., Caie, P., Gavriel, C., Schmidt, G., Harrison, D.J., 2018. Context-based interpolation of coarse deep learning prediction maps for the segmentation of fine structures in immunofluorescence images (March 2018). p. 24. https://doi.org/10.1117/12.2292794.

[13] Van De Plas, R., Yang, J., Spraggins, J., Caprioli, R.M., 2015. Image fusion of mass spectrometry and microscopy: a multimodality paradigm for molecular tissue mapping. Nature Methods 12(4):366—372. https://doi.org/10.1038/nmeth.3296.

[14] Neumann, E.K., Comi, T.J., Rubakhin, S.S., Sweedler, J.V., 2019. Lipid heterogeneity between astrocytes and neurons revealed by single-cell MALDI-MS combined with immunocytochemical classification. Angewandte Chemie International Edition 58(18):5910—5914. https://doi.org/10.1002/anie.201812892.

[15] Roscioni, S.S., Migliorini, A., Gegg, M., Lickert, H., 2016. Impact of islet architecture on β-cell heterogeneity, plasticity and function. Nature Reviews Endocrinology 12(12):695—709. https://doi.org/10.1038/nrendo.2016.147.

[16] Carrano, A.C., Mulas, F., Zeng, C., Sander, M., 2017. Interrogating islets in health and disease with single-cell technologies. Molecular Metabolism 6(9): 991—1001. https://doi.org/10.1016/j.molmet.2017.04.012.

[17] Farack, L., Golan, M., Egozi, A., Dezorella, N., Bahar Halpern, K., Ben-Moshe, S., et al., 2019. Transcriptional heterogeneity of beta cells in the intact pancreas. Developmental Cell 48(1):115—125. https://doi.org/10.1016/j.devcel.2018.11.001 e4.

[18] Ly, A., Buck, A., Balluff, B., Sun, N., Gorzolka, K., Feuchtinger, A., et al., 2016. High-mass-resolution MALDI mass spectrometry imaging of metabolites from formalin-fixed paraffin-embedded tissue. Nature Protocols 11(8):1428—1443. https://doi.org/10.1038/nprot.2016.081.

[19] Aichler, M., Borgmann, D., Krumsiek, J., Buck, A., MacDonald, P.E., Fox, J.E.M., et al., 2017. N-acyl taurines and acylcarnitines cause an imbalance in insulin synthesis and secretion provoking β cell dysfunction in type 2 diabetes. Cell Metabolism 25(6):1334—1347. https://doi.org/10.1016/j.cmet.2017.04.012 e4.

[20] Wishart, D.S., Feunang, Y.D., Marcu, A., Guo, A.C., Liang, K., Rosa, V., et al., 2018. HMDB 4.0 : the human metabolome database for 2018. Nucleic Acids Research 46:608—617. https://doi.org/10.1093/nar/gkx1089 (November 2017).

[21] Schindelin, J., Arganda-Carreras, I., Frise, E., Kaynig, V., Longair, M., Pietzsch, T., et al., 2012. Fiji: an open-source platform for biological-image analysis. Nature Methods 9(7):676—682. https://doi.org/10.1038/nmeth.2019.

[22] Shannon, P., Markiel, A., Ozier, O., Baliga, N.S., Wang, J.T., Ramage, D., et al., 2003. Cytoscape: a software environment for integrated models of biomolecular interaction networks. Genome Research 13(11):2498—2504. https://doi.org/10.1101/gr.1239303.

[23] Kriegsmann, K., Longuespée, R., Hundemer, M., Zgorzelski, C., Casadonte, R., Schwamborn, K., et al., 2019. Combined immunohistochemistry after mass

[24] Kaya, I., Michno, W., Brinet, D., Iacone, Y., Zanni, G., Blennow, K., et al., 2017. Histology-compatible MALDI mass spectrometry based imaging of neuronal lipids for subsequent immunofluorescent staining. Analytical Chemistry 89(8): 4685—4694. https://doi.org/10.1021/acs.analchem.7b00313.

[25] Da Silva Xavier, G., Rutter, G.A., 2019. Metabolic and functional heterogeneity in pancreatic β cells. Journal of Molecular Biology. https://doi.org/10.1016/j.jmb.2019.08.005.

[26] Van Schravendijk, C.F.H., Kiekens, R., Pipeleers, D.G., 1992. Pancreatic β cell heterogeneity in glucose-induced insulin secretion. Journal of Biological Chemistry 267(30):21344—21348.

[27] Strott, C.A., Higashi, Y., 2003. Cholesterol sulfate in human physiology: what's it all about? Journal of Lipid Research 44(7):1268—1278 https://doi.org/10.1194/jlr.R300005-JLR200.

[28] Dirkx, R., Solimena, M., 2012. Cholesterol-enriched membrane rafts and insulin secretion. Journal of Diabetes Investigation 3(4):339—346. https://doi.org/10.1111/j.2040-1124.2012.00200.x.

[29] Takahashi, T., Suzuki, T., 2012. Role of sulfatide in normal and pathological cells and tissues. Journal of Lipid Research 53(8):1437—1450. https://doi.org/10.1194/jlr.R026682.

[30] Boslem, E., Meikle, P.J., Biden, T.J., 2012. Roles of ceramide and sphingolipids in pancreatic β-cell function and dysfunction. Islets 4(3):177—187. https://doi.org/10.4161/isl.20102.

[31] Holm, L.J., Krogvold, L., Hasselby, J.P., Kaur, S., Claessens, L.A., Russell, M.A., et al., 2018. Abnormal islet sphingolipid metabolism in type 1 diabetes. Diabetologia 61(7):1650—1661. https://doi.org/10.1007/s00125-018-4614-2.

[32] Lee, H.E., Park, K.U., Yoo, S.B., Nam, S.K., Park, D.J., Kim, H.-H., et al., 2013. Clinical significance of intratumoral HER2 heterogeneity in gastric cancer. European Journal of Cancer 49(6):1448—1457. https://doi.org/10.1016/j.ejca.2012.10.018.

[33] Kurokawa, Y., Matsuura, N., Kimura, Y., Adachi, S., Fujita, J., Imamura, H., et al., 2015. Multicenter large-scale study of prognostic impact of HER2 expression in patients with resectable gastric cancer. Gastric Cancer 18(4): 691—697. https://doi.org/10.1007/s10120-014-0430-7.

[34] Ahn, S., Ahn, S., van Vrancken, M., Lee, M., Ha, S.Y., Lee, H., et al., 2015. Ideal number of biopsy tumor fragments for predicting HER2 status in gastric carcinoma resection specimens. Oncotarget 6(35):38372—38380. https://doi.org/10.18632/oncotarget.5368.

[35] Yagi, S., Wakatsuki, T., Yamamoto, N., Chin, K., Takahari, D., Ogura, M., et al., 2019. Clinical significance of intratumoral HER2 heterogeneity on trastuzumab efficacy using endoscopic biopsy specimens in patients with advanced HER2 positive gastric cancer. Gastric Cancer 22(3):518—525. https://doi.org/10.1007/s10120-018-0887-x.

[36] Lee, H.J., Kim, J.Y., Park, S.Y., Park, I.A., Song, I.H., Yu, J.H., et al., 2015. Clinicopathologic significance of the intratumoral heterogeneity of HER2 gene amplification in HER2-positive breast cancer patients treated with adjuvant trastuzumab. American Journal of Clinical Pathology 144(4):570—578. https://doi.org/10.1309/AJCP51HCGPOPWSCY.

[37] Wakatsuki, T., Yamamoto, N., Sano, T., Chin, K., Kawachi, H., Takahari, D., et al., 2018. Clinical impact of intratumoral HER2 heterogeneity on trastuzumab efficacy in patients with HER2-positive gastric cancer. Journal of Gastroenterology 53(11):1186—1195. https://doi.org/10.1007/s00535-018-1464-0.

[38] Kaito, A., Kuwata, T., Tokunaga, M., Shitara, K., Sato, R., Akimoto, T., et al., 2019. HER2 heterogeneity is a poor prognosticator for HER2-positive gastric cancer. World Journal of Clinical Cases 7(15):1964—1977. https://doi.org/10.12998/wjcc.v7.i15.1964.

[39] Hanahan, D., Weinberg, R.a., 2011. Hallmarks of cancer: the next generation. Cell 144(5):646—674. https://doi.org/10.1016/j.cell.2011.02.013.

[40] Arifin, S.A., Falasca, M., 2016. Lysophosphatidylinositol signalling and metabolic diseases. Metabolites 6(1):1–11. https://doi.org/10.3390/metabo6010006.

[41] Bernier, M., Catazaro, J., Singh, N.S., Wnorowski, A., Boguszewska-Czubara, A., Jozwiak, K., et al., 2017. GPR55 receptor antagonist decreases glycolytic activity in PANC-1 pancreatic cancer cell line and tumor xenografts. International Journal of Cancer 141(10):2131–2142. https://doi.org/10.1002/ijc.30904.

[42] Dai, C., Arceo, J., Arnold, J., Sreekumar, A., Dovichi, N.J., Li, J., et al., 2018. Metabolomics of oncogene-specific metabolic reprogramming during breast cancer. Cancer & Metabolism 6(5):1–17. https://doi.org/10.1186/s40170-018-0175-6.

[43] Prade, V.M., Kunzke, T., Feuchtinger, A., Rohm, M., Luber, B., Lordick, F., et al., 2020. MALDI FTICR MS imaging data of pancreatic mouse tissue. https://doi.org/10.5281/zenodo.3607915.

3.3. Patterns of carbon-bound exogenous compounds in patients with lung cancer and association with disease pathophysiology

The publication "Patterns of carbon-bound exogenous compounds in patients with lung cancer and association with disease pathophysiology" [3] examines the cancer metabolism in tissues derived from patients with lung cancer by applying the improved spatial metabolomics method [2]. It has been shown that exogenous metabolites derived from the environment accumulate in a patient's lungs over time [96, 97]; however, the exact localization in lung tissues was so far unknown. A multimodal examination of protein expression by multiplex IHC to automatically distinguish tumor cells from tumor stroma and spatial metabolomics by MALDI MS imaging was consulted to address the question of the exact localization of exogenous metabolites in patient's lungs. We reveal for the first time that tobacco-associated exogenous metabolites were localized at anthracotic pigments, and these compounds are significantly correlating with PD-L1 expression and other tumor biological features. This knowledge substantially improves our understanding of lung cancer pathophysiology since anthracotic pigments are so far an underrated factor for disease progression.

I am sharing the first authorship with my former colleague Verena M. Prade. For this publication, I performed all spatial metabolomics and validation experiments. I calculated the statistics, prepared all figures, and wrote the original draft of the manuscript with Verena M. Prade. Furthermore, I conceived the study design with Verena M. Prade, Sabina Berezowska, and Axel Walch.

Patterns of Carbon-Bound Exogenous Compounds in Patients with Lung Cancer and Association with Disease Pathophysiology

Thomas Kunzke[1], Verena M. Prade[1], Achim Buck[1], Na Sun[1], Annette Feuchtinger[1], Marco Matzka[1], Isis E. Fernandez[2,3], Wim Wuyts[4], Maximilian Ackermann[5,6], Danny Jonigk[7,8], Michaela Aichler[1], Ralph A. Schmid[9], Oliver Eickelberg[10], Sabina Berezowska[11,12], and Axel Walch[1]

ABSTRACT

Asymptomatic anthracosis is the accumulation of black carbon particles in adult human lungs. It is a common occurrence, but the pathophysiologic significance of anthracosis is debatable. Using *in situ* high mass resolution matrix-assisted laser desorption/ionization (MALDI) fourier-transform ion cyclotron resonance (FT-ICR) mass spectrometry imaging analysis, we discovered noxious carbon-bound exogenous compounds, such as polycyclic aromatic hydrocarbons (PAH), tobacco-specific nitrosamines, or aromatic amines, in a series of 330 patients with lung cancer in highly variable and unique patterns. The characteristic nature of carbon-bound exogenous compounds had a strong association with patient outcome, tumor progression, the tumor immune microenvironment, programmed death-ligand 1 (PD-L1) expression, and DNA damage. Spatial correlation network analyses revealed substantial differences in the metabolome of tumor cells compared with tumor stroma depending on carbon-bound exogenous compounds. Overall, the bioactive pool of exogenous compounds is associated with several changes in lung cancer pathophysiology and correlates with patient outcome. Given the high prevalence of anthracosis in the lungs of adult humans, future work should investigate the role of carbon-bound exogenous compounds in lung carcinogenesis and lung cancer therapy.

Significance: This study identifies a bioactive pool of carbon-bound exogenous compounds in patient tissues associated with several tumor biological features, contributing to an improved understanding of drivers of lung cancer pathophysiology.

Introduction

Asymptomatic anthracosis is the macroscopically and histologically visible black discoloration resulting from the deposition of black carbon particles in various anatomical locations of human lungs. Associated with age, environmental pollution, and smoking load, anthracosis can serve as an index of lifetime exposure to exogenous factors (1). Studies have shown lungs of heavy smokers to exhibit more pronounced anthracosis (2) and an association with lung carcinogenesis or cancer progression (3, 4). Others have shown cigarette smoke not to be a risk factor for anthracosis and found no epidemiologic or etiologic link with lung cancer (5).

The highly complex and heterogeneous chemical composition of black carbon particles comprises numerous organic and inorganic compounds, including carbon, silica, aluminum, and iron oxide (5, 6). Black carbon particles can bind potentially toxic or carcinogenic compounds present in air pollutants, soot, dust, or tobacco smoke (2, 7, 8). Furthermore, black carbon particles are carriers of toxic chemicals, such as polycyclic aromatic hydrocarbons (PAH) and nicotine-derived nitrosamine ketones, to the lung, immune cells, and systemic blood circulation (9). The toxins that were originally thought to be chemically inert can be retained, released, or metabolized over a long period of time (10). Although extensively researched, the effects and interplay of carbon particles in anthracosis and exogenous compounds within their natural cellular and extracellular context of human lung tissue are unexplored and challenging due to the complex histologic interrelationships.

[1]Research Unit Analytical Pathology, Helmholtz Zentrum München, German Research Center for Environmental Health, Neuherberg, Germany. [2]Department of Internal Medicine V, Comprehensive Pneumology Center Munich (CPC-M), Member of the German Center for Lung Research (DZL), Ludwig-Maximilians-Universität München, Munich, Germany. [3]Institute of Lung Biology and Disease, Comprehensive Pneumology Center, Helmholtz Zentrum München, Member of the German Center for Lung Research (DZL), Munich, Germany. [4]Department of Respiratory Diseases, University Hospitals Leuven, Leuven, Belgium. [5]Institute of Functional and Clinical Anatomy, University Medical Center Mainz, Johannes Gutenberg-University Mainz, Mainz, Germany. [6]Institute of Pathology and Molecular Pathology, Helios University Hospital Wuppertal, University of Witten/Herdecke, Wuppertal, Germany. [7]Institute of Pathology, Hannover Medical School, Hannover, Germany. Biomedical Research in Endstage and Obstructive Lung Disease Hannover (BREATH). [8]German Center for Lung Research (DZL), Hannover Medical School, Hannover, Germany. [9]Department of General Thoracic Surgery, Inselspital University Hospital Bern, Bern, Switzerland. [10]Division of Pulmonary, Allergy, and Critical Care Medicine, Department of Medicine, University of Pittsburgh, Pittsburgh, Pennsylvania. [11]Institute of Pathology, University of Bern, Bern, Switzerland. [12]Department of Laboratory Medicine and Pathology, Institute of Pathology, Lausanne University Hospital and University of Lausanne, Lausanne, Switzerland.

56

Mass spectrometry imaging (MSI) has gained significant relevance in biomedical research and reveals the discrete distribution of compounds and their related metabolites. MSI has high molecular specificity and allows comprehensive, multiplexed detection and localization of thousands of endogenous metabolites directly in tissues (11). In a very recent study, MSI was applied on mice to characterize the *in situ* organ distribution of intratracheal-instilled and intravenously injected carbon particles, revealing surface-adsorbed aromatic hydrocarbons (12). The toxicologic and pathologic findings based on studies of the molecular and cellular processes induced by toxins are important to achieve a mechanistic understanding. One of the strengths of MSI is its ability to directly overlay molecular information with tissue sections to correlatively compare molecular and histologic information. Therefore, MSI can provide novel insights into the effects and interactions of anthracosis, compounds, and endogenous metabolites within their natural cellular and extracellular context in human lung tissue.

Using *in situ* high mass resolution matrix-assisted laser desorption/ionization (MALDI) fourier-transform ion cyclotron resonance (FT-ICR) MSI analysis, we report carbon-bound exogenous compounds in a series of 330 patients with lung cancer. The spatial distribution of compounds like PAHs, tobacco-specific nitrosamines, or aromatic amines, as well as their impact on patient outcome, tumor progression, composition of intratumoral immune cells, programmed death-ligand 1 (PD-L1) expression, and DNA damage is examined. Furthermore, we investigate metabolic differences between tumor cells and the tumor microenvironment and illuminate the relationship of concentration and composition of black carbon pigments in patients with lung cancer.

Materials and Methods

Patients with squamous cell carcinoma and tissues

We retrospectively analyzed 330 consecutive patients with primary resected squamous cell carcinoma (SCC), diagnosed at the Institute of Pathology, University of Bern without previous or concomitant diagnosis of SCC of other organs, to reliably exclude metastatic lung disease, as previously described (13). The study was done in accordance with the Declaration of Helsinki, and the local Ethics Committee of the Canton of Bern approved the study and waived the requirement for written informed consent (KEK 200/14). The cohort was assembled according to pathology files and validated according to clinical files. The histology of all cases was reassessed according to current World Health Organization (WHO) guidelines for diagnosis of SCC (14). All tumors were restaged according to the Union for International Cancer Control (UICC) 2017, 8th edition tumor–node–metastasis (TNM) classification (15). Overall survival (OS) was defined as the time from the resection to death of any cause. For baseline characteristics, see Supplementary Table S1. A tissue microarray was constructed from formalin-fixed, paraffin-embedded (FFPE) tissue blocks as described before (13). In short, slides were scanned and digitally annotated with subsequent automatic transferal of the punches to a tissue microarray (TMA) receptor block, which was used for further analysis. Additionally, full tissue sections were used for comparison between tissue microarray cores and full tissue sections.

Patients with idiopathic pulmonary fibrosis and tissues

Idiopathic pulmonary fibrosis (IPF) tissues were collected at the Institute of Pathology, Hannover Medical School, Germany (FFPE), as previously described (16). All patients provided written informed consent, and the study was done in accordance with the Declaration of Helsinki. All experiments were performed in accordance with relevant guidelines and regulations (ethical votes #1691–2013 or #3381–2016, Hannover Medical School). In brief, the specimens for primary surgical resection were obtained from patients diagnosed with lung IPF ($n = 10$) and preserved as FFPE material.

In addition, explanted lung tissue from patients with IPF ($n = 4$) and healthy organ donors ($n = 4$) were inflated with air to a transpulmonary pressure of 30 cm H_2O, then deflated to 10 cm H_2O while freezing in liquid nitrogen vapor; frozen samples were stored at $-80°C$. This study was approved by the hospital ethics and university biosafety committees in Leuven, Belgium (ML6385). IPF tissues and healthy lung tissues were collected at KU Leuven, as previously described (17). All patients provided written informed consent, and the study was done in accordance with the Declaration of Helsinki. For baseline characteristics, see Supplementary Table S2.

Quantification of anthracotic pigment

Tissues were counterstained with nuclear red stain (Fluka, 60700, 0.1%). Stained tissue sections were scanned using an AxioScan.Z1 digital slide scanner (Zeiss) equipped with a 20x magnification objective. Quantification of the amount of anthracotic pigments was determined by digital image analysis using the software Definiens Developer XD2 (Definiens AG), following a previously published procedure (18). The calculated parameter was the ratio of pigment area respective to total tissue area for each core.

High mass resolution MALDI FT-ICR MSI

High mass resolution MALDI FT-ICR MSI was performed as previously described (19, 20). In brief, FFPE sections (4 μm) or fresh frozen sections (12 μm) were mounted onto indium–tin–oxide (ITO)–coated glass slides (Bruker Daltonik). The air-dried tissue sections were spray-coated with 10 mg/mL of 9-aminoacridine hydrochloride monohydrate matrix (Sigma–Aldrich) in methanol (70%) using the SunCollect sprayer (Sunchrom). Prior to matrix application, FFPE tissue sections were incubated additionally for 1 hour at 70°C and deparaffinized in xylene (2 × 8 minutes). Spray-coating of the matrix was conducted in 8 passes (ascending flow rates 10 μL/minute, 20 μL/minute, and 30 μL/minute for layers 1–3 and for layers 4–8 with 40 μL/minute), utilizing 2-mm line distance and a spray velocity of 900 mm/minute.

Metabolites were detected in negative-ion mode on a 7 T Solarix XR FT-ICR mass spectrometer (Bruker Daltonik) equipped with a dual electrospray ionization MALDI (ESI-MALDI) source and a SmartBeam-II Nd: YAG (355 nm) laser. Mass spectra were acquired within m/z 50 to 1,100 and a lateral resolution of 50 μm. L-Arginine was used for external calibration in the electrospray ionization (ESI) mode. The SCiLS lab software 2020b was used to export the picked peaks of the mass spectra as processed and root mean square normalized imzML files.

The SPACiAL workflow was used as previously described to automatically annotate tumor and stroma regions in SCC tissues (21). In short, after MALDI-MSI analysis, the 9-aminoacridine matrix was removed with ethanol (70%) for 5 minutes from tissue sections, followed by IHC staining. Double staining of the TMA was performed using pan-cytokeratin [monoclonal mouse pan-cytokeratin plus (AE1/AE3+8/18), 1:75, catalog no. CM162; Biocare Medical, RRID: AB_10582491) and vimentin (Abcam, clone ab92547, 1:500, RRID: AB_10562134). Regions positive for pan-cytokeratin were defined as tumor. Regions negative for pan-cytokeratin but positive for vimentin were defined as stroma.

Discovery and visualization of exogenous and endogenous compounds

In order to discover and visualize exogenous and endogenous compounds, mass spectra in and near anthracotic pigments were extracted using the SCiLS lab software 2020b. Annotations were performed using Kyoto Encyclopedia of Genes and Genomes (KEGG, RRID: SCR_012773; ref. 22), The Human Metabolome Database (HMDB; RRID: SCR_007712; ref. 23), and Hoffmann analytes (24).

We performed a stringent annotation of molecules using the following inclusion criteria: (i) The molecular mass of endogenous and exogenous compounds must be between 50 Da and 1100 Da; (ii) the signal to noise ratio must be above 2; (iii) for exogenous compounds, literature evidence must exist for their presence in tobacco smoke. Exclusion criteria were: (i) Signals that were annotated as isotopes were excluded; (ii) as previously published, substances with HMDB descriptions containing a reference to drugs, pesticides, or other implausible descriptions were excluded (21). M-H, M-H_2O-H, and M+Cl as negative adducts with a mass tolerance of 4 ppm were prioritized.

On-tissue measurement of benzo[a]pyrene

Benzo[a]pyrene was purchased from Sigma Aldrich and diluted in xylene. One microliter benzo[a]pyrene solution was spotted onto human fresh frozen lung tissue sections between the absolute amounts of 60 nmol–0.6 nmol benzo[a]pyrene. Matrix application and high mass resolution MALDI FT-ICR MSI was performed as described before. Stack plot was created by flexImaging (v. 5.0, Bruker), and overlayed peak spectra were illustrated in mMass (v. 5.5.0). Curve fitting was performed with GraphPad Prism (v. 9.2.0).

IHC staining

IHC staining for cluster of differentiation 3 (CD3), cluster of differentiation 8 (CD8), and PD-L1 was performed as previously described (13) on consecutive sections. In brief, an automated immunostainer (Bond III, Leica Bio-systems) with anti-CD3 (Abcam Cambridge; clone SP7, 1:400, RRID: AB_443425), anti-CD8 (Dako, clone C8/144B, 1:100, RRID: AB_2075537), and anti-PD-L1 (Cell Signaling Technology, clone E1L3N, 1:400, RRID: AB_2687655) was used. The numbers of CD8^{+} and CD3^{+} tumor infiltrating lymphocytes were determined using image analysis (Aperio Image Scope) and adjusted for core completeness. PD-L1 expression was assessed as the intensity of membranous staining by a pathologist (S. Berezowska).

Immunofluorescence analysis of γH2AX

Immunofluorescence analysis of γH2AX expression was achieved using primary antibodies against pH2A.X (Cell Signaling Technology; catalog no. 2577, 1:400, RRID: AB_2118010) and pan-cytokeratin [monoclonal mouse pan-cytokeratin plus (AE1/AE3+8/18), 1:75, catalog no. CM162; Biocare Medical, RRID: AB_10582491) on consecutive sections. Slides were digitized at 20× objective magnification using an Axio Scan.Z1 (Zeiss). Quantification was performed by digital image analysis in Definiens Developer XD2, following a previously published procedure (18). The quantified parameter was the ratio of γH2AX and pan-cytokeratin-positive cells to the total number of pan-cytokeratin-positive cells.

Statistical analysis

Correlations were calculated using pairwise Spearman rank-order correlation (Python 3.7, SciPy 1.2.0, RRID: SCR_008058). Spearman P values were adjusted with Benjamini–Hochberg correction (Python 3.7, StatsModels 0.9.0). To determine significant differences between UICC TNM stages, Kruskal–Wallis test by ranks (Python 3.7, SciPy 1.2.0) and posthoc Dunn multiple comparison test (Python 3.7, scikit-posthocs 0.6.1) were used in conjunction with Benjamini–Hochberg correction. Cutoff-optimized survival analyses were performed using a Kaplan–Meier Fitter and log–rank test (Python 3.7, lifelines 0.24.8). Cutoff-optimized in this context means that the threshold for low and high abundance of a compound was chosen such that the P value in the resulting Kaplan–Meier curve is minimal, while ensuring robust results for similar cutoffs.

We investigated the association between the survival time of patients and several predictor variables. The Cox proportional hazards model is a regression model commonly used in medical research for this purpose. The multivariate analysis was performed using the Cox proportional hazards model (Python 3.8, lifelines 0.25.7) using the same cutoffs as for Kaplan–Meier Fitter. Categorical data were used for the Cox proportional hazards model. Compounds that passed the nonproportional test were included in the model (Python 3.8, lifelines 0.25.7). All survival calculations were based on OS.

Spatial correlation networks

Correlation networks were created with Cytoscape (v. 3.8.0, RRID: SCR_003032; ref. 25). All networks were visualized using the edge weighted spring embedded layout and the absolute value of the correlation coefficient calculated as described above. Compounds with at least one significant correlation are shown ($P < 0.05$).

Circular plots

Circular plots were generated using Circos (v.0.69.8, RRID: SCR_011798; ref. 26). The metabolites of interest and correlations with the exogenous compounds were extracted from the spatial correlation networks. Pathway information for each metabolite was extracted from KEGG (22). If available, common compound name abbreviations were retrieved from HMDB (23) or KEGG databases.

Results

Carbon pigment is common not only in normal lung tissue, but also in lung SCC

Carbon deposits can be seen macroscopically (**Fig. 1A**), often found in the center of the tumor (27), beyond parenchymal (**Fig. 1B**) and pleural anthracosis (**Fig. 1C**). They are found intratumorally dispersed with varying degrees (**Fig. 1D** and **E**). Using digital image analysis, anthracotic pigment was quantified in SCC tissues of 313 patients (**Fig. 1F–H**) for subsequent statistical analyses (e.g., correlations with clinical parameters).

Concentration of carbon pigment in lung SCC does not correlate with smoking, DNA damage, presence of lymphocytes, PD-L1 expression, or patient survival

There is no significant association between the amount of carbon pigment and smoking behavior (pack-years, $P = 0.91$), DNA damage (γH2AX expression, $P = 0.61$), lymphocyte number (CD3, $P = 0.42$; and CD8, $P = 0.67$), PD-L1 expression ($P = 0.07$), and patient OS ($P = 0.23$, cut-off = 0.005%; **Fig. 1I–K**). There are no significant correlations for pigment quantity. Next, the molecular composition was further investigated.

Exogenous compounds such as PAHs, tobacco-specific nitrosamines, and aromatic amines are highly abundant in and nearby carbon pigment

Using high mass resolution MALDI FT-ICR MSI, 11 exogenous compounds were detected at different abundances throughout the tissues. Importantly, the abundance is highest in and nearby the

58

anthracotic pigment (**Fig. 2**). The exogenous compounds can be grouped into four classes: PAHs, tobacco-specific nitrosamines, aromatic amines, and organohalogens (**Fig. 2A**).

Five PAHs, benzo[a]pyrene (*m/z*: 287.0639), dibenz(a,h)anthracene (*m/z*: 313.0800), dibenzo[a,l]pyrene (*m/z*: 337.0775), benzo[b]pyridine (*m/z*: 128.0504), and 7-OH-12-methylbenz[a]anthracene sulfate (*m/z*: 351.0692) are particularly rich in carbon pigment (**Fig. 2**). Within pigment interspersed tissue, 3 tobacco-specific nitrosamines were detected: 4-(methylnitrosamino)-1-(3-pyridyl)-1-butanone [nicotine-derived nitrosamine ketone (NNK), m/z: 242.0702], 4-(methylnitrosamino)-1-(3-pyridyl)-1-butanol (NNAL, *m/z*: 208.1091), and NNAL-N-glucuronide (*m/z*: 367.1373; **Fig. 2B** and **C**). N-hydroxy-4-aminobiphenyl (*m/z*: 220.0526) and N-hydroxy-MeIQx (*m/z*: 264.0650) are aromatic amines and dichloroethane (*m/z*: 96.9617) is an organohalogen. To determine the quantity of benzo[a]pyrene as an example, we performed a spicking experiment. The minimum amount for detecting benzo[a]pyrene in lung tissues is 2 nmol (Supplementary Fig. S1).

In total, the concentration of exogenous compounds correlates with the amount of anthracotic pigment for benzo[a]pyrene ($P = 0.0009$), dibenz(a,h)anthracene ($P = 0.0056$), dibenzo[a,l]pyrene ($P = 0.0405$), NNK ($P = 0.0316$), NNAL ($P = 0.0338$), and NNAL-N-glucuronide ($P = 0.0257$). The correlations between carbon pigment and exogenous compounds are all positive. In the next, we analyzed the patterns of the exogenous compounds in the carbon pigment within and between the individual patients.

The chemical composition of carbon pigment is highly variable and unique for each patient

The chemical composition of carbon pigment is heterogeneous in terms of the pattern and abundance of the compounds within the different areas of lung tissue (**Fig. 3**; **Fig. 3A**; Supplementary Fig. S2 and S3). The variability of the chemical composition is also visible at the microscopic scale: **Fig. 3B** shows SCC regions from two patients with unique compositions of carbon-bound compounds. Although the carbon pigments of both regions exhibit a high amount of dibenz(a,h)anthracene, other compounds are present at very different abundances. A multicolor visualization of NNK, NNAL, and NNAL-N-glucuronide also shows an entirely different chemical signature (**Fig. 3C**; Supplementary Fig. S4). The chemical composition was shown to be unique and heterogenous within and between patients. Next, we investigated the differences within the tissue compartments stratified to tumor cells and tumor stroma.

Different quantities and qualities of carbon-bound compounds were found within tumor and stroma

We used our recently published SPACiAL method for immuno-phenotype-guided separation of tumor and stromal tissue compartments (21) to investigate the associated carbon pigment (Supplementary Figs. S5 and S6). The amount and prevalence of exogenous compounds differ between tumor and stromal regions (**Fig. 4A**; Supplementary Fig. S7). Most exogenous molecules were more frequently measured in tumor pigments. However, PAHs and tobacco-specific nitrosamines, if present in stroma, are more abundant there.

The abundance of carbon-bound compounds was next correlated to tumor features and patient characteristics. **Figure 4A** is a comparative representation of the abundance of compounds correlating with smoking behavior, DNA damage, and immunologic features.

NNK and dichloroethane are associated with smoking behavior

Several carbon-bound compounds correlate with smoking behavior, DNA damage, lymphocyte number, PD-L1 expression, and tumor progression (**Fig. 4**). In tumor, NNK and dichloroethane are significantly associated with smoking behavior (**Fig. 4B**, $P = 0.0114$ and $P = 0.0215$, respectively).

DNA damage in cancer cells and high amounts of PAH are interrelated

A total of 89.7% of the patients have γH2AX-positive tumor cells, which is indicative of DNA damage. The PAHs benzo[a]pyrene ($P = 0.0020$), dibenz(a,h)anthracene ($P = 0.0262$), and dibenzo[a,l]pyrene ($P = 0.0432$) correlate positively with γH2AX (**Fig. 4C**).

In tumor tissue, PAHs and NNAL are linked to T-cell infiltration and PD-L1 expression

In tumor regions, dibenz(a,h)anthracene abundance correlates negatively with both the overall number of tumor infiltrating T cells (CD3, $P = 0.0429$) and CD8 ($P = 0.0450$; **Fig. 4D**). In stromal areas, dibenzo[a,l]pyrene correlates positively with CD3 and CD8 ($P = 0.0292$ and $P = 0.0156$, respectively). The intensity of tumoral PD-L1 expression correlates negatively with NNAL abundance ($P = 0.0489$).

Tumor stage is associated with benzo[a]pyrene and dibenz(a,h)anthracene

Benzo[a]pyrene in stroma regions ($P = 0.0364$) and dibenz(a,h)anthracene in tumor and stroma regions ($P = 0.0400$, $P = 0.0439$, respectively) are associated with UICC tumor stages (**Fig. 4E**). In contrast to carbon-bound PAHs, the amount of carbon pigment shows no association with tumor stage ($P = 0.1729$).

Patient outcome correlates with amount and spatial location of PAHs, NNKs, and aromatic amines

Two PAHs, benzo[b]pyridine (tumor, $P = 0.0103$) and dibenz(a,h)anthracene (stroma, $P = 0.0270$) correlate significantly with OS (**Fig. 5A**, see also Supplementary Figs. S8 and S9). Additionally, two tobacco-specific nitrosamines, NNK ($P = 0.0071$) and NNAL-N-glucuronide ($P = 0.0298$), are significantly correlated with survival (**Fig. 5B**). However, a higher concentration of NNK is associated with poor OS, while its detoxified form, NNAL-N-glucuronide, is significantly linked with better OS. In contrast, higher amounts of the two aromatic amines, N-hydroxy-MeIQx and N-hydroxy-4-aminobiphenyl, are significantly correlated with poor patient outcome, both in tumor and in stroma (**Fig. 5C**).

We also tested the correlation of CD3, CD8, PD-L1, and pack-years with patient survival. High expression of CD3 ($P = 0.0139$) and CD8 ($P = 0.0275$) in tumor stroma regions, low expression of PD-L1 in tumor cells ($P = 0.0021$), and low pack-years ($P = 0.0003$) are associated with good survival (Supplementary Fig. S10).

PAH, NNK, and aromatic amines are independent factors for OS

We investigated the association between the survival time of patients and several predictor variables and used the Cox proportional hazards model. Benzo[b]pyridine ($P = 0.0019$), dibenz(a,h)anthracene ($P = 0.0150$), NNK ($P = 0.0043$), and N-hydroxy-MeIQx ($P = 0.0008$) are independent factors for OS (**Fig. 5D**). The highest HR was determined for NNK in stroma (HR = 5.0263) and N-hydroxy-MeIQx in tumor (HR = 3.0943), indicating that a higher amount of these compounds is deleterious.

After finding significant correlations of individual carbon-bound compounds with tumor features and patient characteristics, we investigated spatial correlations of exogenous and endogenous compounds with a focus on pathway and network analyses.
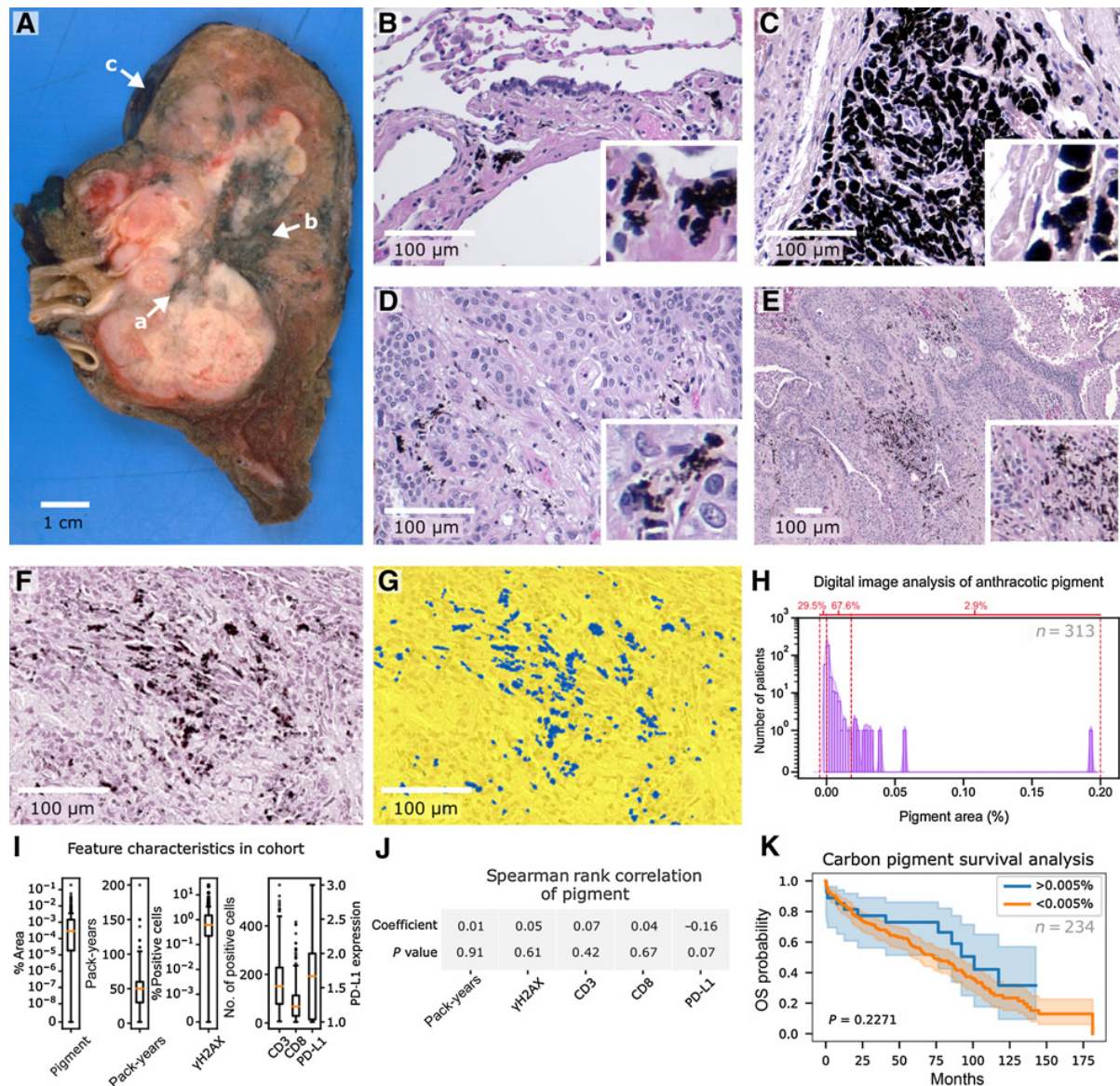
Figure 1.
Carbon pigment is abundant in both normal-lung and pulmonary SCC tissue. **A,** Gross appearance of lung SCC tissue. The tumor tissue has grayish, focal areas with carbon pigment deposits at the center (a). Additionally, anthracosis with carbon deposits are seen in lung parenchyma (b) and pleura (c). **B** and **C,** Histology of normal lung tissue exhibiting carbon pigment deposits (hematoxylin and eosin staining). The pigment accumulates in the cytoplasm of macrophages in the bronchial wall. **D** and **E,** Histopathology of lung SCC tissue with dispersed intratumoral carbon deposits. High magnification shows the close spatial relationship of carbon particles and cancer cells. **F** and **G,** Carbon deposits in SCC (nuclear red stain) and segmentation (blue) by image analysis for the quantification of carbon particles. Subsequent analyses are based on pigment quantification (**H–K**). **H,** Distribution of pigment amount within tumor tissue. Patients can be divided into those with no, low, or high pigment content. **I,** Distribution of feature characteristics relating to pigment content, smoking behavior, DNA damage, and CD3, CD8, and PD-L1 expression. **J,** Spearman rank correlation of the pigment area with feature characteristics, showing no significant correlation. **K,** Survival analysis showing that pigment abundance does not correlate with patient survival ($n = 234$; cutoff $= 0.005\%$).

Spatial correlation networks of metabolites and exogenous compounds reveal substantially different metabolism in tumor and stroma regions

To investigate the metabolic changes of tumor cells associated with exogenous compound quantities, we evaluated the spatial correlation networks of metabolites in 330 patient tissues. Dense clusters within the networks indicate stronger spatial correlation, and therefore, dependencies between quantities of exogenous and endogenous compounds. Pixelwise spatial correlations within and between metabolites and eleven exogenous compounds were calculated and filtered ($P < 0.05$). In the two resulting networks, the spatial correlation of 133 metabolites within tumor cells and 159 metabolites in the stroma are visualized (**Fig. 6**).

60
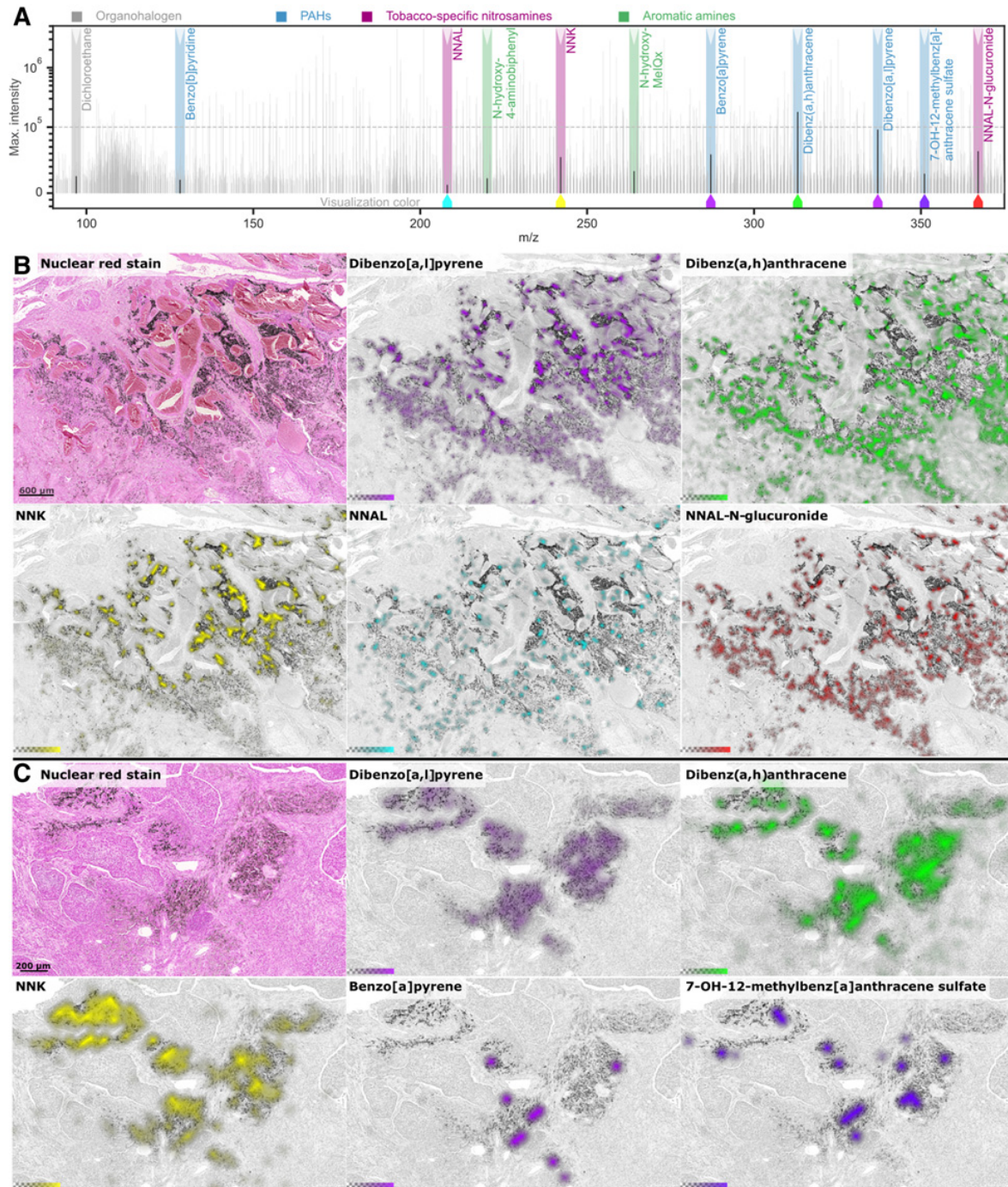
Figure 2.
Carbon-bound exogenous compounds detected with high mass resolution MALDI FT-ICR MSI. **A,** Skyline spectrum showing maximum peak intensities between 90 and 375 dalton. Exogenous compounds are highlighted and colored according to their respective class: PAHs (blue), tobacco-specific nitrosamines (red), aromatic amines (green), and an organohalogen (gray). Max., maximum. **B,** Tissue region featuring high carbon pigment content (top left; nuclear red stain) and ion distribution of dibenzo[a, l]pyrene, dibenz(a,h)anthracene, NNK, NNAL, and NNAL-N-glucuronide. Note that all five show a close spatial relationship to the pigment, but also differing distribution patterns. Although NNK has focal high intensity in dense carbon deposits, NNAL-N-glucuronide is conversely distributed within the pigment. **C,** Tumor tissue region featuring extensive intratumoral carbon pigment deposits (top left; nuclear red stain). Spatial organization of dibenzo[a, l]pyrene, dibenz(a,h)anthracene, NNK, benzo[a]pyrene, and 7-OH-12-methylbenz[a]anthracene sulfate and the intratumoral carbon pigment. There are obvious differences in the abundance and distribution pattern of PAHs and NNK and that of carbon pigment, indicating intratumoral heterogeneity.
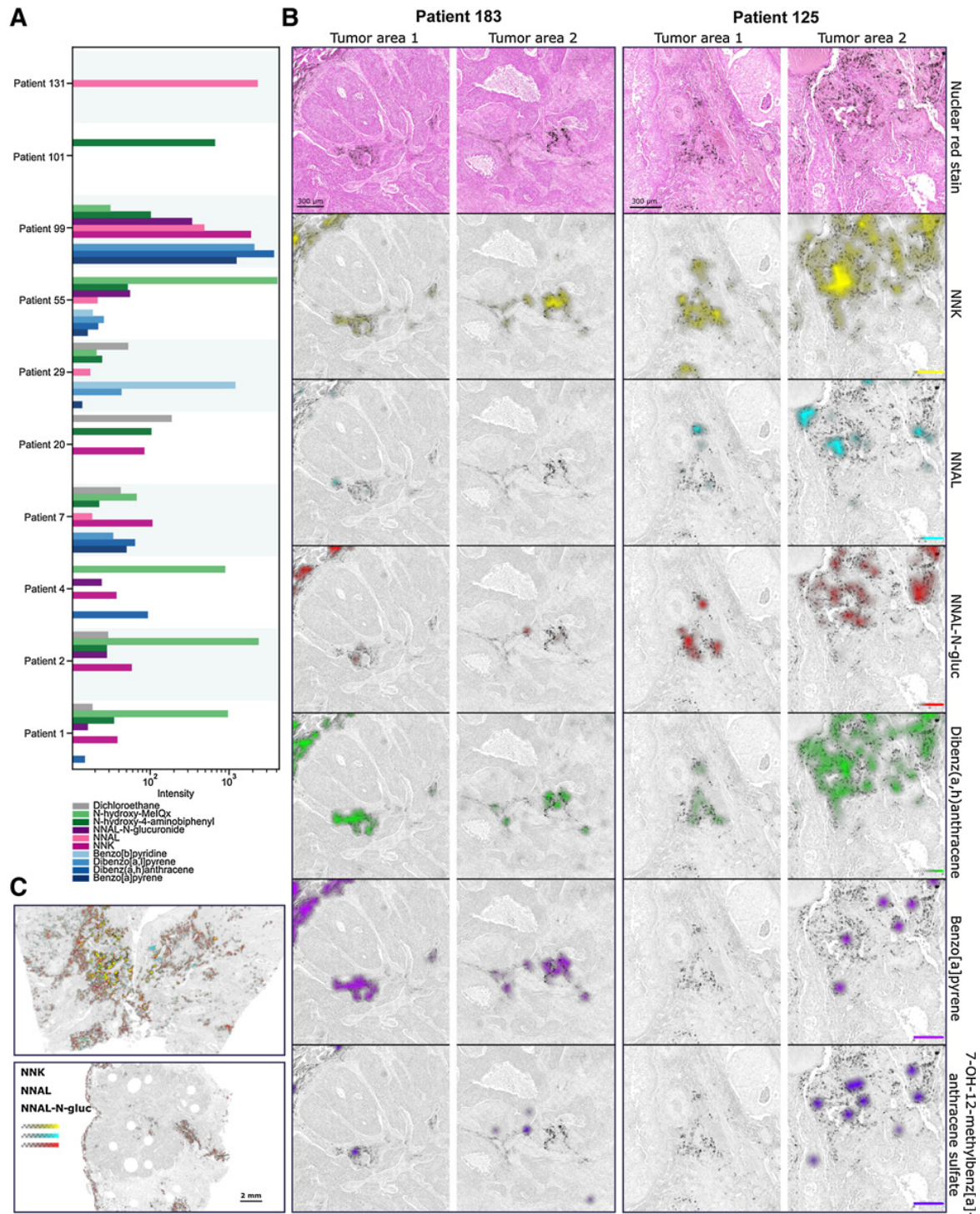
Figure 3.
Inter- and intratumoral heterogeneity in the chemical composition of carbon pigment in SCC. **A,** Signal intensities of carbon-bound compounds in the tissues of 10 patients, illustrating the unique and heterogeneous chemical composition of carbon pigment. See Supplementary Fig. S3 for all patients. **B,** SCC tissues from two patients with comparable intratumoral carbon depositions (nuclear red stains) and distribution of carbon-bound compounds: NNK, NNAL, NNAL-N-glucuronide, dibenz(a,h)anthracene, benzo[a]pyrene, and 7-OH-12-methylbenz[a]anthracene sulfate. **C,** Visualization of NNK, NNAL, and NNAL-N-glucuronide demonstrates heterogeneity within one patient tissue. See Supplementary Fig. S4 for increased visibility.

62
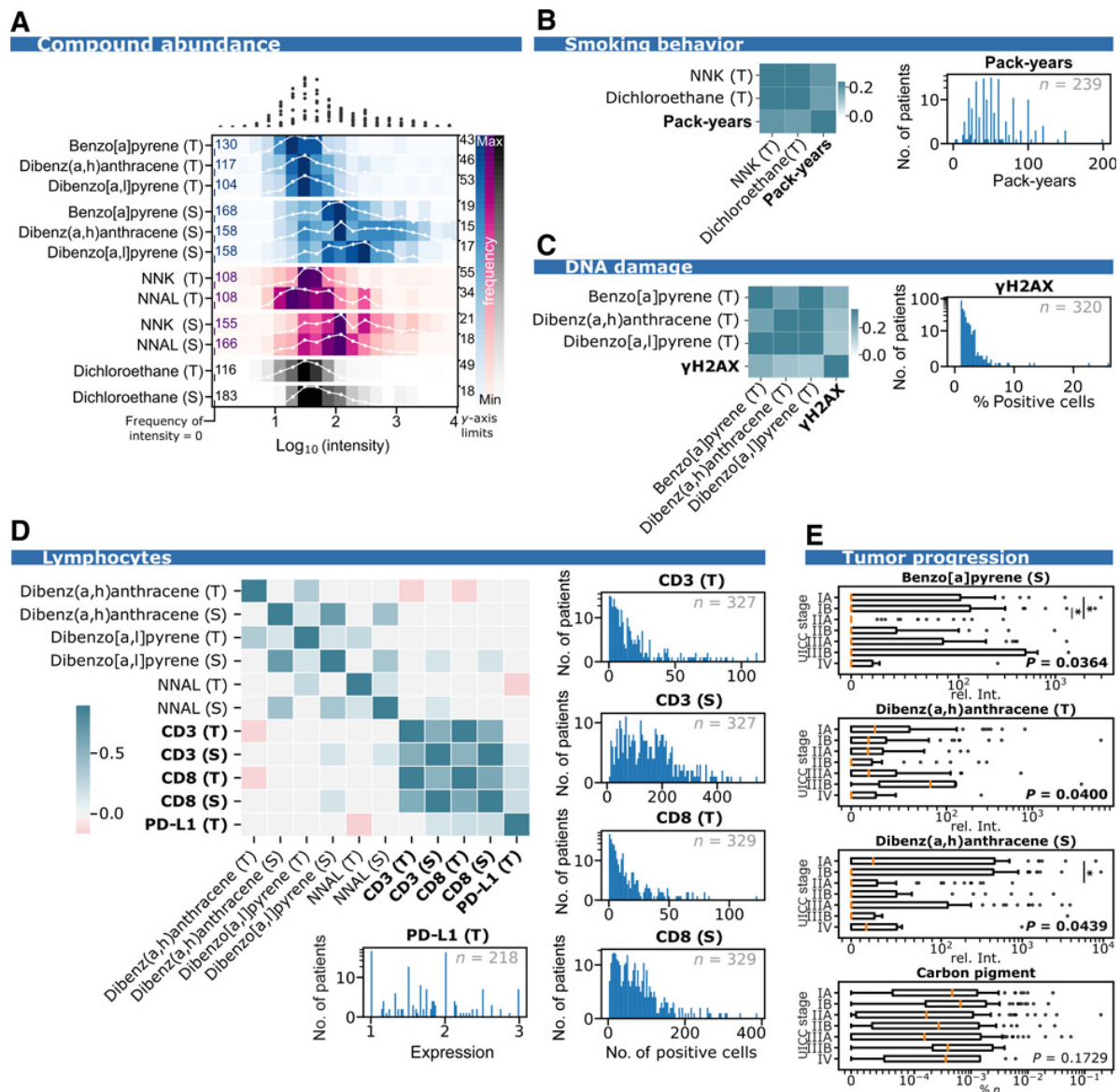
Figure 4.
Concentration and prevalence of carbon-bound exogenous compounds and their correlation with smoking behavior, DNA damage, lymphocyte number, PD-L1 expression, and tumor progression. **A,** Intensity distribution of carbon-bound compounds in the tumor (T) and stromal (S) regions. The noncumulative histograms are visualized as heatmaps to facilitate visual comparison. Because the logarithmic intensities are shown, the counts of intensity = 0 are separately shown on the left of each row. To the right of each row the maximum number of patients in a bin is shown. Min., minimum. **B,** Significant correlation between NNK and dichloroethane and pack-years (left) and distribution of pack-years (noncumulative histogram, right). **C,** Significant correlation between PAH and γH2AX (left) and distribution of γH2AX percent positive cells (noncumulative histogram, right). **D,** Significant correlation between compounds with immunologic features (top left) and distribution of the number of positive cells or expression per feature characteristic (histograms). **E,** Benzo[a]pyrene (S), dibenz(a,h)anthracene (T), and dibenz(a,h)anthracene (S) but not carbon pigment are associated with the UICC tumor stage.

In tumor, N-hydroxy-MeIQx is associated with altered lipid and glutathione metabolism

The spatial correlation network in tumor reveals no distinct cluster of exogenous compounds (**Fig. 6A**). N-Hydroxy-MeIQx, which has the most striking effect on patient survival, was detected in a dense cluster of metabolites (maximum $r_S = 0.79$), featuring a higher spatial positive correlation with glutathione (GSH, $r_S = 0.408$).

Most endogenous metabolites within the cluster of interest can be associated with lipid metabolism (41.2%), whereby the strongest, albeit not very pronounced positive correlations to N-hydroxy-MeIQx were found for 9 (10)-EpOME (9,10-EOA, $r_S = 0.166$), sn-glycero-3-phosphoethanolamine (NGPE, $r_S = 0.173$), and sn-glycerol 3-phosphate (G3P, $r_S = 0.185$). The second most represented pathway is nucleotide metabolism (17.6%). Higher quantities

63
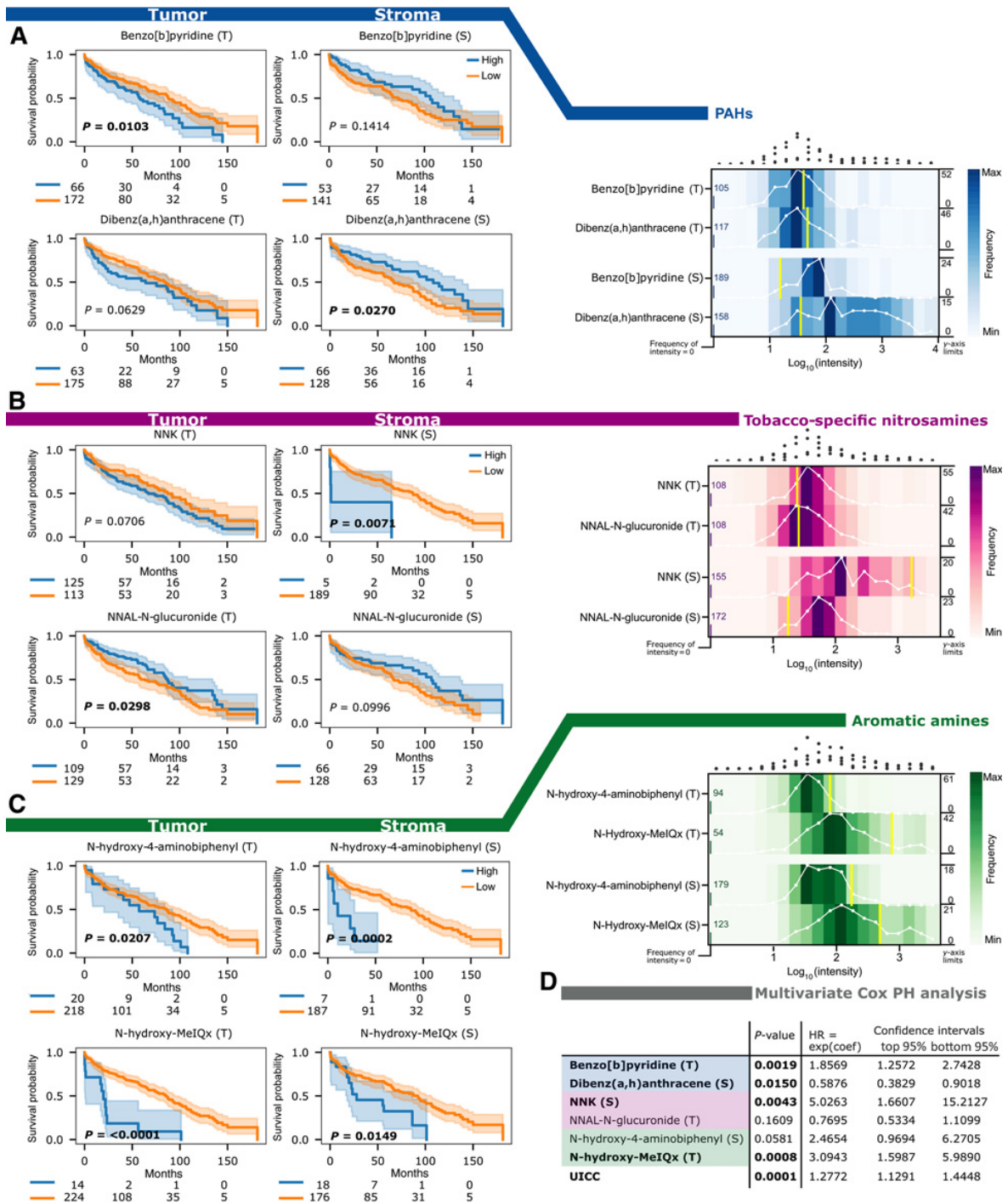
Figure 5.
The abundance of carbon-bound exogenous compounds is an independent factor for patient outcome. **A–C,** Kaplan–Meier survival analyses (left) and distribution of compound abundance (noncumulative histograms, right), including the intensity threshold used to split the collective (yellow) for PAHs (**A**), nitrosamines (**B**), and aromatic amines (**C**). On the right, the y-axes are annotated with the maximum frequency per distribution. Only compounds with a significant separation are shown here ($P < 0.05$). All Kaplan–Meier curves as well as the histograms for all exogenous compounds can be found in the supplementary data (Supplementary Figs. S8 and S9). **D,** Cox proportional hazard model for the shown compounds, with significant separation in the Kaplan–Meier analyses (log–rank test), and which passed the nonproportional test, as well as the UICC stage. All but two compounds remained significant in multivariate analysis, indicating that they are independent factors for patient survival. PH, proportional hazards; coef, coefficient.

64

of the purine metabolite deoxyinosine-phosphate (dIMP, $r_S = 0.159$) and the pyrimidine metabolites cytidine (Cyd, $r_S = 0.127$) and deoxycytidine diphosphate (dCDP, $r_S = 0.151$) are associated with an increased N-hydroxy-MeIQx concentration (**Fig. 6A**).

In stroma, PAH and tobacco-specific nitrosamines have a strong impact on amino acid and nucleotide metabolism

The spatial correlation network for the stroma region differs substantially from the network for the tumor region (**Fig. 6B**). Six exogenous molecules are part of a dense cluster together with endogenous metabolites. The highest spatial correlation was found between the two exogenous compounds dibenzo[a,l]pyrene and dibenz(a,h) anthracene ($r_S = 0.679$). Unlike the network for the tumor region, most of the correlating metabolites in the main cluster take part in amino acid or nucleotide metabolism.

Four metabolites with a role in amino acid metabolism are related to tryptophan metabolism. A high abundance of tryptophan metabolites is associated with high PAH and tobacco-specific nitrosamine concentrations. Deoxyadenosine (dA), deoxyinosine (D-Ino), deoxycytidine (dC), and deoxyuridine (dU) are two purine and two pyrimidine metabolites from the nucleotide metabolism pathway that correlate positively with the exogenous compounds (**Fig. 6B**).

Carbon-bound exogenous compounds are also present in IPF

In addition to lung cancer, other respiratory pathophysiologic conditions, such as interstitial lung diseases, have been linked to environmental pollutants, e.g., due to epigenetic modification (28). With the analysis of IPF tissue, we aim to highlight, albeit not in depth, the presence and possible significance of anthracosis on other respiratory pathophysiologic conditions. Similarly to SCC we found inter- and intrapatient heterogeneity of carbon-bound exogenous compounds in both normal lung parenchyma and IPF. In contrast to the tumor and tumor stroma, spatial correlation networks for IPF tissues reveal two clusters of exogenous compounds and endogenous metabolites. One cluster comprises several PAHs including dibenzo[a,l]pyrene, dibenz(a,h)anthracene, and benzo[a]pyrene, while the other is a mixture of two PAHs - benzo[b]pyrene and 7-hydroxymethyl-12-methylbenz[a]anthracene sulfate, one tobacco-specific nitrosamine and one aromatic amine. Both the spatially correlating endogenous and exogenous compounds within the clusters and the biological pathways they are related to show only minor similarity to the tumor metabolic networks and pathway analysis. See supplementary information for details (Supplementary Fig. S11–S14).

Discussion

We have discovered a biologically active pool of carbon-bound exogenous compounds in lung cancer tissue. High amounts of these exogenous compounds in various and patient-unique chemical combinations were found in and near anthracotic pigment. Although the detected exogenous compounds are known carcinogens, we show here for the first time that these exogenous compounds also have a strong impact on tumor pathophysiology and survival outcome of patients with lung cancer.

Carbon particles accumulate in human lungs and exhibit a large surface area as well as specific surface characteristics for the adsorption of inorganic and organic exogenous compounds (29–31). In mouse lungs, carbon particles were shown to persist indefinitely (32). The long-term persistence and bioavailability of carbon-bound exogenous compounds is supported by further animal studies showing that the

detection of benzo[a]pyrene was possible up to 5.6 months after incubation (33).

We used *in situ* high mass resolution MALDI FT-ICR MSI to show that the chemical composition of carbon particles in human lung cancer tissue is much more complex than expected. Each patient showed a unique chemical signature of carbon particles (**Fig. 3A**). Even within 1 patient, carbon particles exhibit high chemical heterogeneity (**Fig. 3B**). Both extrinsic factors, such as environmental conditions, and intrinsic factors, such as metabolism of exogenous compounds, may play a role for the diverse chemical patterns of carbon pigments. However, our cohort mainly comprises patients with a history of smoking and SCC is a clear smoker-associated type of cancer (Supplementary Table S1). Hence, the particles analyzed in this study are likely smoking related. Certain PAHs accumulate in smokers' lungs (34, 35), however, their localization and pathophysiologic impact remains unclear. Nevertheless, Tomingas and colleagues demonstrated a large increase of benzo[a]pyrene in human bronchial carcinoma in contrast to adjacent tissue (36). In contrast, our study localized exogenous compounds in human lungs and illustrates the significance of these compounds on SCC depending on their spatial localization. In our patient cohort, NNK, as the most abundant systemic lung carcinogen in cigarette smoke (37), showed the strongest correlation with pack-years (**Fig. 4B**). Indeed, NNK is derived mainly from tobacco smoke. In contrast, PAHs can be derived from numerous environmental sources (38), explaining the lack of a significant correlation.

Unique differences in the metabolism of exogenous compounds are an intrinsic factor for the chemical signature of carbon particles. This is known in carcinogenesis research, and crucial pathways in PAH metabolism arguably differ between patients (39, 40). We found that carbon-bound exogenous compounds are present and bioactive in tumor tissue beyond carcinogenesis (**Figs. 2**, **4** and **5**), and their abundance may strongly depend on the metabolic activity in individual patients. Our observations revealed a high variation in NNK, its reduced form NNAL, and its detoxification product NNAL-N-glucuronide (41), suggesting unique metabolic activities in patients (**Fig. 3A**).

In our study, an increased concentration of PAHs was associated with increased DNA damage in tumor cells (**Fig. 4C**). Another study focused on carbon particles in mouse lungs and confirmed our finding that anthracosis is associated with DNA damage (32). Alexandrov and colleagues showed that tobacco smoking and PAH exposure cause specific mutations representing the leading mutation signature of lung cancer (42). High mutational burden is associated with an improved objective response to anti–Programmed cell death protein 1 (PD-1) therapy, patient survival, and durable clinical benefit in non–small cell lung cancers (43). Tumor mutational burden and PD-L1 are used as predictive markers for immunotherapies. Thus, our data suggests that these exogenous molecules may influence SCC therapies.

While we found exogenous compounds as toxic molecules of tobacco smoke and environmental factors, a recent study found the presence of an exogenous molecule as a drug in anthracosis. Cisplatin can be accurately detected in tissues using laser ablation inductively coupled plasma mass spectrometry (LA-ICP-MS) imaging. Greenhalgh and colleagues (44) applied LA-ICP-MS imaging for 3D *ex vivo* human explant model and demonstrated for the first time a spatial correlation between platinum and anthracosis in lung tissue. The carbon deposits found in lung tissue may affect the movement and thus the efficacy of cisplatin treatment. The authors conclude that cisplatin penetration can be predicted and monitored by LA-ICP-MS imaging as a screening tool (44). This underlines the potential therapeutic implications of anthracosis in non–small cell lung cancer.

65

Kunzke et al.
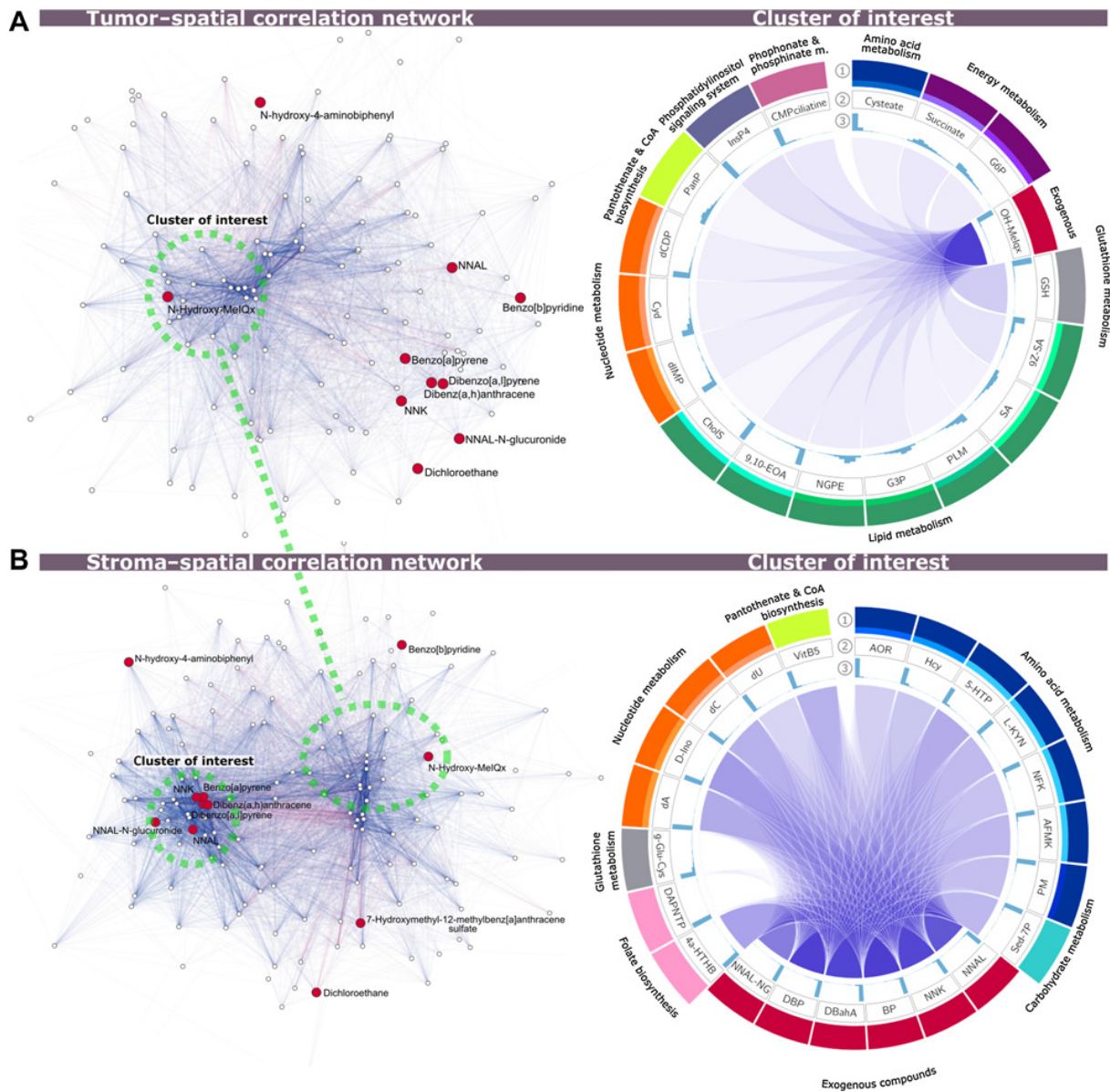
Figure 6.

Spatial correlation between carbon-bound compounds and endogenous metabolites in tumor ($n = 313$; **A**) and stroma ($n = 268$; **B**) tissue. Nodes in the spatial correlation networks (left), endogenous metabolites (white), and carbon-bound compounds (red); edges, positive (blue) and negative (red) spatial correlations, with edge opacity increasing with the correlation coefficient. Circular plots (right) focus on the highlighted compounds from the networks and exclusively on correlations with carbon-bound compounds (middle). Tracks: (i) pathway information; (ii) compound abbreviation; (iii) histogram of the minimum/maximum scaled compound signal intensities. Note that within the stroma, multiple carbon-bound compounds form a dense cluster with endogenous metabolites mainly involved in amino acid and nucleotide metabolism, whereas in the tumor, only N-hydroxy-MeIQx is part of a cluster of metabolites involved in lipid metabolism. L-cysteate, cysteate; D-glucose 6-phosphate, G6P; N-hydroxy-MeIQx, OH-MeIQx; glutathione, GSH; (9Z)-stearic acid, 9Z-SA; stearic acid, SA; palmitic acid, PLM; sn-glycerol 3-phosphate, G3P; sn-glycero-3-phosphoethanolamine, NGPE; 9 (10)-EpOME, 9,10-EOA; cholesterol sulfate, CholS; cytidine, Cyd; D-4′-phosphopantothenate, PanP; inositol 1,3,4,5-tetraphosphate, InsP4; CMP-2-aminoethylphosphonate, CMPciliatine; N-acetylornithine, AOR; L-homocysteine, Hcy; 5-hydroxy-L-tryptophan, 5-HTP; L-kynurenine, L-KYN; L-formylkynurenine, NFK; formyl-N-acetyl-5-methoxykynurenamine, AFMK; pyridoxamine, PM; sedoheptulose 7-phosphate, Sed-7P; benzo[a]pyrene, BP; dibenz(a,h)anthracene, DBahA; dibenzo[a,l]pyrene, DBP; NNAL N-glucuronide, NNAL-NG; 4a-hydroxytetrahydrobiopterin, 4a-HTHB; 2,5-diaminopyrimidine nucleoside triphosphate, DAPNTP; gamma-L-glutamyl-L-cysteine, g-Glu-Cys; deoxyadenosine, dA; deoxyinosine, D-Ino; deoxycytidine, dC; deoxyuridine, dU; pantothenate, Vit B5.

66

Because LA-ICP-MS imaging is capable of measuring metals, it would be interesting to apply this MSI technology to measure metals in the anthracotic pigment, which are also present in cigarette smoke (45).

Lymphocytes are known to be associated with harmful compounds in lung cancer tissues. In our study, the infiltration of $CD3^+$ and $CD8^+$ lymphocytes was correlated with the concentrations of dibenz(a,h)anthracene and dibenzo[a,l]pyrene (**Fig. 4D**). Many PAHs influence patient immunity, as they are important ligands of the aryl hydrocarbon receptor (AhR) on several immune cells (46, 47). Systemic AhR activation by an exogenous compound triggers the suppression of the $CD8^+$ T-cell response in infected lungs (48). In our study, a suppression of T cells was observed with a higher concentration of dibenz(a,h)anthracene in tumor regions. Another study showed that tobacco smoke and benzo[a]pyrene lead to $CD8^+$ lymphocyte enrichment in mouse lungs, possibly induced by AhR (49). In this study, a similar effect of lymphocyte enrichment was seen in the stroma regions for high concentrations of dibenzo[a,l]pyrene.

We have shown for the first time that exogenous compounds have a strong impact on patient survival (**Fig. 5**). The presence of NNK, NNAL-N-glucuronide, and N-hydroxy-4-aminobiphenyl in SCC tissues was associated with patient outcomes. A study on 770 resected lung cancers revealed poorer prognosis for smokers (50). We observed the same effect of smoking on survival (Supplementary Fig. S10). All substances with a significant effect on survival can be associated with tobacco smoke. Interestingly, the nonmetabolized primary substance from tobacco smoke, NNK, was associated with poor OS. In contrast, the detoxified variant of the metabolite, NNAL-N-glucuronide, was an indicator of a favorable prognosis (**Fig. 5B**). Hence, glucuronidation may be worth investigating in more detail for detoxification of exogenous compounds. This is underlined by another study, which revealed that smokers with an increased urinary level of glucuronidated nitrosamine N'-nitrosonornicotine experienced a significantly reduced risk of esophageal cancer (51). Whether and to what extent glucuronidation in lungs of human individuals can be specifically influenced still remains open.

Correlations between endogenous metabolites and exogenous molecules are fundamentally different between tumor and stroma regions. Notably, in tumor regions, N-hydroxy-MeIQx alters lipid and glutathione metabolism. A higher abundance of the metabolite N-hydroxy-MeIQx is associated with increased lipid species and a higher concentration of glutathione (**Fig. 6A**). The effect of MeIQx on lipid profile, potentially caused by dysregulated maturation of autolysosomes, has been described in hepatocytes (52). Otherwise, glutathione has been shown to increase the perceptivity to oxidative stress (53). The formation of 8-hydroxy-2′-deoxyguanosine, an oxidative DNA damage marker, increases in the liver with a specific dose of MeIQx (54). Oxidative stress caused by N-hydroxy-MeIQx may be contained by an increase in glutathione in tumor cells.

In tumor stroma, PAHs and tobacco-specific nitrosamines revealed a strong impact on amino acid and nucleotide metabolism (**Fig. 6B**). Notably, the majority of the changed amino acid metabolites can be associated with tryptophan metabolism, which is of crucial importance to the immune system as its metabolites orchestrate local and systemic responses to control inflammation (55). The indole ring of the critical regulatory molecule tryptophan is cleaved by indoleamine 2,3-dioxygenase (IDO; ref. 56). The activation of AhR increases IDO expression (57). Therefore, PAHs may increase tryptophan metabolism through the activation of AhR. Our second finding that nucleotide metabolism is enhanced is most likely associated with DNA damage and repair caused by these substances.

The effects of carbon-bound exogenous compounds might also be of pathophysiologic significance for other lung diseases. Anthracosis has been described to be associated with nonneoplastic diseases such as emphysema (32). We have selected IPF as an example for an exploratory analysis of anthracotic pigment in the context of nonneoplastic diseases. IPF is a lung disease of unknown etiology and is characterized by progressive scarring. The underlying pathomechanisms of IPF, with its complex immunologic and inflammatory processes and external impacts, have been the focus of recent research. Lifestyle and environmental influences are held responsible for much of its natural history. Because smoking, pneumotoxic medications, and inhalation of dust are known risk factors of IPF (58), we analyzed the presence and constitution of exogenous compounds within anthracotic tissue of patients with IPF to uncover differences to the smoking-related SCC. Indeed, we also found carbon-bound exogenous molecules in IPF anthracotic pigment. Similarly to SCC we found inter and intrapatient heterogeneity of carbon-bound exogenous compounds in both, normal-lung parenchyma and IPF. Furthermore, the network analysis revealed differences in the affected metabolic pathways compared with SCC tissues. We conclude that exogenous compounds could be an unrecognized factor in the development and progression of IPF. These preliminary findings warrant further investigation.

When the amount of anthracotic pigment is considered over the total volume of both lungs, there is a large and persistent pool of carbon-bound exogenous compounds with possible systemic effects beyond the lungs. Tobacco smoking is also the leading risk factor for bladder cancer (41). As a representative of aromatic amines, 4-aminobiphenyl has been extensively studied to understand the mechanism of bladder carcinogenesis (59). We discovered that N-hydroxy-4-aminobiphenyl, a carbon-bound exogenous compound, was highly abundant in human lung tissue. Given the potentially large amount of anthracotic pigment in both lungs, it is possible that 4-aminobiphenyl is stored in the pigment and released continuously over the long term and thus may contribute to the development of bladder carcinoma. Similarly, other carcinogens could be stored and continuously released via the persistent carbon pool and thus also play a role in the development of tumors outside the lung.

Since carbon particles and carbon-bound exogenous compounds are known to be persistent, and the subsequent removal of the carbon particles from the lung is as of yet not feasible, the most reasonable and implementable courses of action right now are risk assessment and prevention. Apart from smoking cessation, a change in smoking behavior may influence concentrations of biomarkers of exposure. For example, in a large scale study including 5,105 participants, e-cigarette users showed a 10% to 98% lower concentration of PAHs compared with exclusive cigarette smokers– albeit it was still significantly increased compared to the levels in never smokers (60). Based on another study, the most significant determinants of PAH exposure beyond smoking are diet and indoor exposures like coal- or wood-heaters, cooking, diverse leisure activities, and passive tobacco smoke - and most of these exposures can be deemed preventable (61). In the case of PAHs, there are several physical and chemical remediation strategies to remove PAHs from polluted environments including membrane filtration, soil washing, adsorption, electrokinetic, thermal, oxidation, and photocatalytic treatments (62). Given that we here show that several exogenous compounds are present directly within anthracotic pigment and that they are an unrecognized factor with strong impact on tumor pathophysiology underlines the importance of risk assessment and prevention.

In conclusion, the bioactive pool of exogenous compounds in and nearby the anthracotic pigment is associated with several changes in

tumor pathophysiology and has adverse effects on patient outcome. Genome integrity, immune factors, and tumor progression are associated with specific chemical signatures in the anthracotic pigment. The exact localization of exogenous compounds influences patient outcome by altering amino acid, nucleotide, and lipid metabolism. In lung IPF, exogenous substances can also be found in and nearby anthracotic pigment, however, these molecules affect other pathways (Supplementary Fig. S11). The exogenous compounds may contribute to the formation and influence the progression of diseases of the lung and other organs. Because all healthy lung tissues contained exogenous compounds (Supplementary Fig. S14), a deeper understanding of the unique composition and pathophysiologic relevance of anthracosis is needed.

Authors' Disclosures

W. Wuyts reports grants from Roche, Boehringer Ingelheim and grants from Galapagos outside the submitted work. O. Eickelberg reports personal fees from Blade Therapeutics and personal fees from Pieris outside the submitted work. A. Walch reports grants from Ministry of Education and Research of the Federal Republic of Germany, the Deutsche Forschungsgemeinschaft, and the Deutsche Krebshilfe outside the submitted work. No disclosures were reported by the other authors.

Authors' Contributions

T. Kunzke: Conceptualization, visualization, methodology, writing–original draft, writing–review and editing. **V.M. Prade:** Conceptualization, visualization, methodology, writing–original draft, writing–review and editing. **A. Buck:** Methodology, writing–review and editing. **N. Sun:** Visualization, methodology, writing–review and editing. **A. Feuchtinger:** Methodology, writing–review and editing. **M. Matzka:** Methodology, writing–review and editing. **I.E. Fernandez:** Resources, writing–review and editing. **W. Wuyts:** Resources, writing–review and editing. **M. Ackermann:** Resources, writing–review and editing. **D. Jonigk:** Resources, writing–review and editing. **M. Aichler:** Methodology, writing–review and editing. **R.A. Schmid:** Resources, writing–review and editing. **O. Eickelberg:** Resources, writing–review and editing. **S. Berezowska:** Conceptualization, resources, supervision, writing–original draft, writing–review and editing. **A. Walch:** Conceptualization, resources, supervision, writing–review and editing.

Acknowledgments

References

1. Takano APC, Justo LT, Dos Santos NV, Marquezini MV, de André PA, da Rocha FMM, et al. Pleural anthracosis as an indicator of lifetime exposure to urban air pollution: An autopsy-based study in Sao Paulo. Environ Res 2019;173:23–32.

2. Saxena RK, McClure ME, Hays MD, Green FHY, McPhee LJ, Vallyathan V, et al. Quantitative assessment of elemental carbon in the lungs of never smokers, cigarette smokers, and coal miners. J Toxicol Environ Health A 2011;74:706–15.

3. Wang D, Minami Y, Shu Y, Konno S, Iijima T, Morishita Y, et al. The implication of background anthracosis in the development and progression of pulmonary adenocarcinoma. Cancer Sci 2003;94:707–11.

4. Konno S, Morishita Y, Fukasawa M, Shu Y, Wang D, Tanaka R, et al. Anthracotic index and DNA methylation status of sputum contents can be used for identifying the population at risk of lung carcinoma. Cancer 2004;102:348–54.

5. Mirsadraee M. Anthracosis of the lungs: etiology, clinical manifestations and diagnosis: a review. Tanaffos 2014;13:1–13.

6. Churg A. The uptake of mineral particles by pulmonary epithelial cells. Am J Respir Crit Care Med 1996;154:1124–40.

7. Mitchev K, Dumortier P, De VP. "Black Spots" and hyaline pleural plaques on the parietal pleura of 150 urban necropsy cases. Am J Surg Pathol 2002;26:1198–206.

8. Sun JD, Wolff RK, Kanapilly GM, McClellan RO. Lung retention and metabolic fate of inhaled benzo(a)pyrene associated with diesel exhaust particles. Toxicol Appl Pharmacol 1984;73:48–59.

9. Janssen NAH, Gerlofs-Nijland ME, Lanki T, O Salonen R, Cassee F, Hoek G, et al. Health effects of black carbon. Copenhagen, Denmark: World Health Organization; 2012.

10. Oh S-Y, Chiu PC. Graphite- and soot-mediated reduction of 2,4-dinitrotoluene and hexahydro-1,3,5-trinitro-1,3,5-triazine. Environ Sci Technol 2009;43:6983–8.

11. Norris JL, Caprioli RM. Analysis of tissue specimens by matrix-assisted laser desorption/ionization imaging mass spectrometry in biological and clinical research. Chem Rev 2013;113:2309–42.

12. Jiang Y, Sun J, Xiong C, Liu H, Li Y, Wang X, et al. Mass spectrometry imaging reveals in situ behaviors of multiple components in aerosol particles. Angew Chem Int Ed Engl 2021;60:23225–31.

13. Keller MD, Neppl C, Irmak Y, Hall SR, Schmid RA, Langer R, et al. Adverse prognostic value of PD-L1 expression in primary resected pulmonary squamous cell carcinomas and paired mediastinal lymph node metastases. Mod Pathol 2018;31:101–10.

14. WHO Classification of Tumours Editorial Board. Thoracic Tumours. WHO Classification of Tumours, 5th ed. Volume 5. Lyon, France: IARC Publications; 2021.

15. Neppl C, Keller MD, Scherz A, Dorn P, Schmid RA, Zlobec I, et al. Comparison of the 7th and 8th edition of the UICC/AJCC TNM staging system in primary resected squamous cell carcinomas of the lung-a single center analysis of 354 cases. Front Med 2019;6:196.

16. Aichler M, Kunzke T, Buck A, Sun N, Ackermann M, Jonigk D, et al. Molecular similarities and differences from human pulmonary fibrosis and corresponding mouse model: MALDI imaging mass spectrometry in comparative medicine. Lab Invest 2018;98:141–9.

17. Sun N, Fernandez IE, Wei M, Witting M, Aichler M, Feuchtinger A, et al. Pharmacometabolic response to pirfenidone in pulmonary fibrosis detected by MALDI-FTICR-MSI. Eur Respir J 2018;52:1702314.

18. Feuchtinger A, Stiehler T, Jütting U, Marjanovic G, Luber B, Langer R, et al. Image analysis of immunohistochemistry is superior to visual scoring as shown for patient outcome of esophageal adenocarcinoma. Histochem Cell Biol 2015; 143:1–9.

19. Ly A, Buck A, Balluff B, Sun N, Gorzolka K, Feuchtinger A, et al. High-mass-resolution MALDI mass spectrometry imaging of metabolites from formalin-fixed paraffin-embedded tissue. Nat Protoc 2016;11:1428–43.

20. Aichler M, Borgmann D, Krumsiek J, Buck A, MacDonald PE, Fox JEM, et al. N-acyl Taurines and Acylcarnitines cause an imbalance in insulin synthesis and secretion provoking β cell dysfunction in type 2 diabetes. Cell Metab 2017;25:1334–47.

21. Prade VM, Kunzke T, Feuchtinger A, Rohm M, Luber B, Lordick F, et al. De novo discovery of metabolic heterogeneity with immunophenotype-guided imaging mass spectrometry. Mol Metab 2020;36:100953.

22. Kanehisa M, Goto S. KEGG: kyoto encyclopedia of genes and genomes. Nucleic Acids Res 2000;28:27–30.

23. Wishart DS, Feunang YD, Marcu A, Guo AC, Liang K, Vázquez-Fresno R, et al. HMDB 4.0: the human metabolome database for 2018. Nucleic Acids Res 2018; 46:D608–17.

24. Hoffmann D, Hoffmann I. Letters to the Editor - Tobacco smoke components. Beiträge zur Tabakforschung International/Contributions to Tobacco Research 1998;18:49–52.

25. Shannon P, Markiel A, Ozier O, Baliga NS, Wang JT, Ramage D, et al. Cytoscape: a software environment for integrated models of biomolecular interaction networks. Genome Res 2003;13:2498–504.

68

26. Krzywinski M, Schein J, Birol I, Connors J, Gascoyne R, Horsman D, et al. Circos: an information aesthetic for comparative genomics. Genome Res 2009; 19:1639–45.
27. Travis WD, Brambilla E, Burke AP, Marx A, Nicholson AG, editors. WHO Classification of Tumours of the Lung, Pleura, Thymus and Heart. WHO Classification of Tumours, 4th ed. Volume 7. Lyon, France: IARC Publications; 2015.
28. Goobie GC, Nouraie M, Zhang Y, Kass DJ, Ryerson CJ, Carlsten C, et al. Air pollution and interstitial lung diseases: defining epigenomic effects. Am J Respir Crit Care Med 2020;202:1217–24.
29. IARC Working Group on the evaluation of carcinogenic risks to humans. Carbon black, titanium dioxide, and talc. Volume 93. In Proceedings of the IARC Working Group on the evaluation of carcinogenic risks to humans; 2006 Feb 7–14; Lyon, France. World Health Organization International Agency For Research On Cancer; 2010. p. 1–413.
30. World Health Organization. Regional Office for Europe. Air Quality Guidelines for Europe. 2nd ed. WHO Regional Publications, European Series; 2000.
31. Möller W, Felten K, Sommerer K, Scheuch G, Meyer G, Meyer P, et al. Deposition, retention, and translocation of ultrafine particles from the central airways and lung periphery. Am J Respir Crit Care Med 2008;177:426–32.
32. You R, Lu W, Shan M, Berlin JM, Samuel EL, Marcano DC, et al. Nanoparticulate carbon black in cigarette smoke induces DNA cleavage and Th17-mediated emphysema. Elife 2015;4:e09623.
33. Gerde P, Muggenburg BA, Lundborg M, Tesfaigzi Y, Dahl AR. Respiratory epithelial penetration and clearance of particle-borne benzo[a]pyrene. Res Rep Health Eff Inst 2001;5:25.
34. Goldman R, Enewold L, Pellizzari E, Beach JB, Bowman ED, Krishnan SS, et al. Smoking increases carcinogenic polycyclic aromatic hydrocarbons in human lung tissue. Cancer Res 2001;61:6367–71.
35. Lodovici M, Akpan V, Giovannini L, Migliani F, Dolara P. Benzo[a]pyrene diol-epoxide DNA adducts and levels of polycyclic aromatic hydrocarbons in autoptic samples from human lungs. Chem Biol Interact 1998;116:199–212.
36. Tomingas R, Pott F, Dehnen W. Polycyclic aromatic hydrocarbons in human bronchial carcinoma. Cancer Lett 1976;1:189–95.
37. Chapman S. Tobacco: science, policy and public health. BMJ 2005;330:970.2.
38. Nielsen T. Traffic contribution of polycyclic aromatic hydrocarbons in the center of a large city. Atmos Environ 1996;30:3481–90.
39. Hecht SS, Hochalter JB, Carmella SG, Zhang Y, Rauch DM, Fujioka N, et al. Longitudinal study of [D10]phenanthrene metabolism by the diol epoxide pathway in smokers. Biomarkers 2013;18:144–50.
40. Carmella SG, Chen M, Yagi H, Jerina DM, Hecht SS. Analysis of phenanthrols in human urine by gas chromatography-mass spectrometry: potential use in carcinogen metabolite phenotyping. Cancer Epidemiol Biomarkers Prev 2004; 13:2167–74.
41. Hecht SS. Tobacco carcinogens, their biomarkers and tobacco-induced cancer. Nat Rev Cancer 2003;3:733–44.
42. Alexandrov LB, Nik-Zainal S, Wedge DC, Aparicio SAJR, Behjati S, Biankin AV, et al. Signatures of mutational processes in human cancer. Nature 2013;500:415–21.
43. Rizvi NA, Hellmann MD, Snyder A, Kvistborg P, Makarov V, Havel JJ, et al. Cancer immunology. Mutational landscape determines sensitivity to PD-1 blockade in non-small cell lung cancer. Science 2015;348:124–8.
44. Greenhalgh CJ, Karekla E, Miles GJ, Powley IR, Costa C, de Jesus J, et al. Exploration of matrix effects in laser ablation inductively coupled plasma mass spectrometry imaging of cisplatin-treated tumors. Anal Chem 2020;92:9847–55.
45. Bernhard D, Rossmann A, Wick G. Metals in cigarette smoke. IUBMB Life 2005; 57:805–9.
46. Shimizu Y, Nakatsuru Y, Ichinose M, Takahashi Y, Kume H, Mimura J, et al. Benzo[a]pyrene carcinogenicity is lost in mice lacking the aryl hydrocarbon receptor. Proc Natl Acad Sci U S A 2000;97:779–82.
47. Gutiérrez-Vázquez C, Quintana FJ. Regulation of the immune response by the Aryl hydrocarbon receptor. Immunity 2018;48:19–33.
48. Lawrence BP, Roberts AD, Neumiller JJ, Cundiff JA, Woodland DL. Aryl hydrocarbon receptor activation impairs the priming but not the recall of influenza virus-specific CD8+ T cells in the lung. J Immunol 2006;177:5819–28.
49. Wang G-Z, Zhang L, Zhao X-C, Gao S-H, Qu L-W, Yu H, et al. The Aryl hydrocarbon receptor mediates tobacco-induced PD-L1 expression and is associated with response to immunotherapy. Nat Commun 2019;10:1125.
50. Hanagiri T, Sugio K, Mizukami M, Ichiki Y, Sugaya M, Yasuda M, et al. Significance of smoking as a postoperative prognostic factor in patients with non-small cell lung cancer. J Thorac Oncol 2008;3:1127–32.
51. Yuan J-M, Knezevich AD, Wang R, Gao Y-T, Hecht SS, Stepanov I. Urinary levels of the tobacco-specific carcinogen N'-nitrosonornicotine and its glucuronide are strongly associated with esophageal cancer risk in smokers. Carcinogenesis 2011; 32:1366–71.
52. Song D, Guo R, Huang H, Zheng P, Huang H, Oyang Q, et al. 2-Amino-3,8-dimethylimidazo[4,5-]quinoxaline alters autophagosome maturation, cellular lipidomic profiles, and expression of core pluripotent factors. J Agric Food Chem 2019;67:7977–85.
53. Traverso N, Ricciarelli R, Nitti M, Marengo B, Furfaro AL, Pronzato MA, et al. Role of glutathione in cancer progression and chemoresistance. Oxid Med Cell Longev 2013;2013:972913.
54. Kakehashi A, Wei M, Fukushima S, Wanibuchi H. Oxidative stress in the carcinogenicity of chemical carcinogens. Cancers 2013;5:1332–54.
55. Routy J-P, Routy B, Graziani GM, Mehraj V. The kynurenine pathway is a double-edged sword in immune-privileged sites and in cancer: implications for immunotherapy. Int J Tryptophan Res 2016;9:67–77.
56. Grohmann U, Fallarino F, Puccetti P. Tolerance, DCs and tryptophan: much ado about IDO. Trends Immunol 2003;24:242–8.
57. Julliard W, Fechner JH, Mezrich JD. The aryl hydrocarbon receptor meets immunology: friend or foe? A little of both. Front Immunol 2014;5:458.
58. Schäfer SC, Funke-Chambour M, Berezowska S. [Idiopathic pulmonary fibrosis-epidemiology, causes, and clinical course]. Pathologe 2020;41:46–51.
59. Beland FA, Kadlubar FF. Metabolic activation and DNA adducts of aromatic amines and nitroaromatic hydrocarbons. In: Cooper CS, Grover PL, editors. Handbook of experimental pharmacology. Carcinogenesis and mutagenesis. Heidelberg: Springer-Verlag; 1990. p. 267–325.
60. Goniewicz ML, Smith DM, Edwards KC, Blount BC, Caldwell KL, Feng J, et al. Comparison of nicotine and toxicant exposure in users of electronic cigarettes and combustible cigarettes. JAMA Netw Open 2018;1:e185937.
61. Pavanello S, Campisi M, Mastrangelo G, Hoxha M, Bollati V. The effects of everyday-life exposure to polycyclic aromatic hydrocarbons on biological age indicators. Environ Health 2020;19:128.
62. Patel AB, Shaikh S, Jain KR, Desai C, Madamwar D. Polycyclic aromatic hydrocarbons: sources, toxicity, and remediation approaches. Front Microbiol 2020;11:562813.

69

3.4. Derangements of amino acids in cachectic skeletal muscle are caused by mitochondrial dysfunction

The last publication in this thesis, entitled "Derangements of amino acids in cachectic skeletal muscle are caused by mitochondrial dysfunction" [4], focuses on metabolic alterations in skeletal muscle tissues caused by cancer cachexia and is also based on the published SPACiAL pipeline to enable improved spatial metabolomics [2]. This publication highlights the role of mitochondrial dysfunction in the changed amino acid metabolism of cachectic skeletal muscle tissues. This new insight was provided by the multimodal measurement of skeletal muscle tissues by spatial metabolomics, spatial proteomics, and bright field microscopy. We offer the first *in situ* measurement of the cachexia-associated change in the amino acid profile of skeletal muscles and reveal specific amino acids as significantly changed. The altered amino acid profile in cachectic skeletal muscle tissues is significantly associated with changed expressions of mitochondrial proteins and the energy charge of muscle fibers. The presented work serves new insights into the biochemistry of cachexia-associated muscle wasting by illuminating the metabolic fate of amino acids and could be useful for finding drug targets for treating cancer cachexia.

In this publication, I conducted all spatial metabolomics experiments, wrote the original draft of the manuscript, calculated all statistics, and prepared figures. I co-conceived the study design with Axel Walch and Michaela Aichler. Parts of the results of this publication were already included in my master thesis. In particular, the writing of the manuscript, the analyses of patients, annotation of proteins, the spatial analysis of the energy charge, and the major part of the transmission electron microscopy analyses were performed in my time as a doctoral candidate.

Derangements of amino acids in cachectic skeletal muscle are caused by mitochondrial dysfunction

Thomas Kunzke[1], Achim Buck[1], Verena M. Prade[1], Annette Feuchtinger[1], Olga Prokopchuk[2], Marc E. Martignoni[2], Simone Heisz[3,4], Hans Hauner[3,4], Klaus-Peter Janssen[2], Axel Walch[1]* [iD] & Michaela Aichler[1]

[1]*Research Unit Analytical Pathology, Helmholtz Zentrum München, Oberschleißheim, Germany,* [2]*Department of Surgery, Klinikum rechts der Isar, TUM, Munich, Germany,* [3]*Else Kroener-Fresenius-Center for Nutritional Medicine, Klinikum rechts der Isar, TUM, Munich, Germany,* [4]*ZIEL-Institute for Food and Health, Nutritional Medicine Unit, TUM, Freising, Germany*

Abstract

Background Cachexia is the direct cause of at least 20% of cancer-associated deaths. Muscle wasting in skeletal muscle results in weakness, immobility, and death secondary to impaired respiratory muscle function. Muscle proteins are massively degraded in cachexia; nevertheless, the molecular mechanisms related to this process are poorly understood. Previous studies have reported conflicting results regarding the amino acid abundances in cachectic skeletal muscle tissues. There is a clear need to identify the molecular processes of muscle metabolism in the context of cachexia, especially how different types of molecules are involved in the muscle wasting process.

Methods New *in situ*-omics techniques were used to produce a more comprehensive picture of amino acid metabolism in cachectic muscles by determining the quantities of amino acids, proteins, and cellular metabolites. Using matrix-assisted laser desorption/ionization (MALDI) mass spectrometry imaging, we determined the *in situ* concentrations of amino acids and proteins, as well as energy and other cellular metabolites, in skeletal muscle tissues from genetic mouse cancer models (*n* = 21) and from patients with cancer (*n* = 6). Combined results from three individual MALDI mass spectrometry imaging methods were obtained and interpreted. Immunohistochemistry staining for mitochondrial proteins and myosin heavy chain expression, digital image analysis, and transmission electron microscopy complemented the MALDI mass spectrometry imaging results.

Results Metabolic derangements in cachectic mouse muscle tissues were detected, with significantly increased quantities of lysine, arginine, proline, and tyrosine (*P* = 0.0037, *P* = 0.0048, *P* = 0.0430, and *P* = 0.0357, respectively) and significantly reduced quantities of glutamate and aspartate (*P* = 0.0008 and *P* = 0.0124). Human skeletal muscle tissues revealed similar tendencies. A majority of altered amino acids were released by the breakdown of proteins involved in oxidative phosphorylation. Decreased energy charge was observed in cachectic muscle tissues (*P* = 0.0101), which was related to the breakdown of specific proteins. Additionally, expression of the cationic amino acid transporter CAT1 was significantly decreased in the mitochondria of cachectic mouse muscles (*P* = 0.0133); this decrease may play an important role in the alterations of cationic amino acid metabolism and decreased quantity of glutamate observed in cachexia.

Conclusions Our results suggest that mitochondrial dysfunction has a substantial influence on amino acid metabolism in cachectic skeletal muscles, which appears to be triggered by diminished CAT1 expression, as well as the degradation of mitochondrial proteins. These findings provide new insights into the pathobiochemistry of muscle wasting.

Keywords Cancer cachexia; Mitochondrial dysfunctions; Amino acids; MALDI; Mass spectrometry imaging

Introduction

Cachexia, which is often caused by cancer, leads to massive loss of total body mass, generalized inflammation, and pronounced muscle wasting, producing a significant decrease in the quality of life. Loss of skeletal muscle results in weakness, leading to immobility and eventual death secondary to impaired respiratory muscle function.[1] Muscle wasting is thereby one of the most devastating characteristics of cachexia in late-stage cancer, for which no specific treatments are currently available. Several metabolic changes have been associated with loss of muscle mass in cachexia, including decreased protein synthesis, increased protein degradation, and deranged amino acid metabolism.[2]

Until now, researchers have focused on understanding the molecular mechanisms behind protein and amino acid metabolism alterations in cachexia.[3] On the one hand, the activation of the ubiquitin-dependent proteasome pathway seemed to play a major role in protein degradation in cancer cachexia.[4] Specific ubiquitin ligase enzymes (E3) catalyzing the movement of the ubiquitin from the E2 enzyme to the substrate and are strongly up-regulated in an animal model of cachexia.[5] Besides, several proteasome subunits are also up-regulated in a transcriptional manner in cachexia.[6] On the other hand, protein synthesis is influenced, for example, by the activity of mechanistic (a.k.a., mammalian) target of rapamycin complex 1,[7] which is progressively decreased in cachectic mice.[8] All of these molecular processes are associated with a changed amino acid turnover. Meanwhile, only a few studies have reported altered quantities of amino acids in cachectic skeletal muscle,[9–12] and their results have been conflicting. Furthermore, amino acid quantities in the context of protein degradation and synthesis and energy metabolism is a still unexploited topic. Of note, these issues are of utmost importance, as amino acids and proteins are linked and individual amino acids contribute to the energy kinetics of skeletal muscle cells.[13] In addition, a massive amino acid efflux to the circulation can also be occurring by enhanced protein degradation,[2] while a significant part of amino acids is received by the circulation for skeletal muscles.[14]

New in situ "-omics" approaches allow the identification of a broad and comprehensive range of possible alterations in amino acid and protein metabolism to help generate a more global picture of the molecular alterations associated with muscle wasting in cachexia. In the current study, we used matrix-assisted laser desorption/ionization (MALDI) mass spectrometry imaging as a sophisticated label-free, non-targeted, in situ -omics method of examining skeletal muscles from cachectic and non-cachectic mice and patients. This is the first time amino acids, energy and other cellular metabolites, and proteins have been simultaneously examined in situ in the context of cancer cachexia.

Determination of the three classes of molecules enabled the investigation of functional relationships between and within amino acids, energy metabolites, and proteins. It allowed the identification of specific proteins that were potentially degraded and contributing to amino acid release in cachexia. Because cachexia is characterized by increased resting energy expenditure and low energy intake,[1] the interplay between specific amino acids and energy metabolites was examined to detect molecular alterations. The further scope of the following study was the analysis of derangements of amino acids, to identify functional relationships with proteins, and simultaneously examine energy changes in skeletal muscles related to cancer cachexia.

In mice, we found higher quantities of cationic amino acids and lower quantities of glutamate and aspartate in skeletal muscle tissues during cachexia, whereas patient tissues provide first insights in similar molecular changes. Several protein expression changes in the mitochondria of cachectic tissues were associated with alterations in energy and amino acid metabolism. To the best of our knowledge, we herein present the first in situ study describing molecular alterations in cachexia caused by functional changes in the mitochondria of skeletal muscle tissues. Furthermore, we determined that cationic amino acid transporter 1 (CAT1), a mitochondria-associated protein, is involved in this process.

Methods

Collection of tissue samples

This study was approved by the Ethics Committee of the Medical Faculty of the Technical University of Munich (#4916/S), and written consent was obtained from all patients before surgery. The compound mutant mouse line (pVillin-KRAS^{V12G} x Apc^{1638N}), with the inbred C57BL/6N background, was bred at the Zentrum für Präklinische Forschung at Klinikum rechts der Isar, TUM, Munich. The animals were assessed at specific timepoints for the presence of intestinal tumours, as previously described, and their body weights were determined at the time of sacrifice (see Table 1 for baseline characteristics).[15] The non-cachectic group consisted of tumour-free wild-type and single transgenic littermates from the same breedings. Cachectic mice were defined as

Table 1 Baseline characteristics of mouse genetic cancer models

Characteristic	Non-cachectic	Cachectic
Number	10	11
Gender (n)		
Male	9	5
Female	1	6
Age (months)		
Mean	8.7	6.6
Range	4–15	4–10
Weight (g)		
Mean	31.7	26.7
Range	27.4–36.0	21.7–32.0

animals with at least a 10% reduction in body weight, compared with the median weight of the non-cachectic group. All mice were maintained with a 12 hr light–dark cycle and fed a standard diet and water *ad lib*. Overall, 21 mice were analysed, and 11 tumour-bearing mice were classified as cachectic. Ten mice represented the non-cachectic group. Mice were euthanized via cervical dislocation. The quadriceps muscles were subsequently resected and then immediately shock frozen and stored until further use in liquid nitrogen.

Patient tissues (samples from the musculus rectus abdominis) were obtained from patients diagnosed with pancreatic ductal adenocarcinoma (see *Table* 2 for baseline characteristics) during routine surgery. The patients underwent surgery at the Department of Surgery, TUM, from 2008 until 2015. Samples were obtained from 36 patients, 13 of whom exhibited a weight loss of at least 7% within the 6 months before surgery and were thereby defined as cachectic patients. The remaining 23 patients, with a weight loss of less than 5%, were considered non-cachectic. Definition of cachexia was according to an international consensus.[16] Tissues from six patients (three non-cachectic and three cachectic patients; Supporting Information, *Appendix S1* for baseline characteristics) were stored in liquid nitrogen as fresh-frozen samples until MALDI mass spectrometry imaging analysis. Tissues from the remaining 30 patients were fixed in formalin and embedded in paraffin and then used to construct two-tissue microarrays, which were stored at room temperature until immunohistochemistry (IHC) analysis.

Matrix-assisted laser desorption/ionization mass spectrometry imaging

Frozen muscle tissue samples were cryosectioned into 12 μm sections using Microm560 (Microm International, Walldorf,

Germany) and thaw mounted onto indium tin oxide-coated conductive slides (Bruker Daltonics, Bremen, Germany). The slides were pre-treated with 1:1 poly-L-lysine (Sigma-Aldrich, Munich, Germany) and 0.1% Nonidet P-40 (Sigma) before mounting. Briefly, the samples were covered with 10 mg/mL 9-aminoacridine (9AA) matrix (Sigma-Aldrich) in 70% methanol for metabolite analysis or 10 mg/mL 1,5-diaminonaphthalene (DAN) matrix (Sigma-Aldrich) in 70% acetonitrile for amino acid analysis, using a SunCollect sprayer (Sunchrom, Friedrichsdorf, Germany). The following preferences were used for the automatic sprayer (for both 9AA and DAN): vial distance of 0.50 mm for the *X* direction and 2.00 mm for the *Y* direction, 20 mm *Z* position and offset of the spray head, and medium *X/Y* speed. The matrix was deposited in eight layers using variable increasing spray rates, as previously reported by Ly *et al.*.[17] For metabolite analysis, data were acquired in negative ion mode using a Bruker Solarix 7.0 T Fourier-transform ion cyclotron resonance (FTICR) mass spectrometer (Bruker Daltonics) over a mass range of 50–1000 *m/z* and at a lateral resolution of 100 μm. Amino acids were analysed over a mass range of 50–250 *m/z*. Because DAN matrix is not stable in a vacuum, a faster measurement protocol was established by changing the lateral resolution for amino acids to 150 μm. For protein analysis, 10 mg/mL sinapinic acid matrix (Sigma-Aldrich) in 60% acetonitrile and 0.2% trifluoroacetic acid was deposited onto the sections using an ImagePrep automated sprayer (Bruker Daltonics). Linear positive ion mode over a mass range of 2000–25 000 *m/z* was used for protein measurements with the Bruker Ultraflex III MALDI-TOF/TOF MS (Bruker Daltonics). The lateral resolution for examining intact proteins was predefined as 60 μm. The Smartbeam-II Nd:YAG laser (355 nm) fired 300 times for protein ablation with a frequency of 200 Hz and a sample rate of 0.50 GS/s. External calibration was performed with Protein Calibration Standard I (Bruker Daltonics), mixed 1:1 (v/v) with the matrix solution, and spotted onto the slide.

Tissue staining and co-registration

After acquisition of the mass spectrometry data, the matrix was removed with 70% ethanol, and the tissue sections were stained with haematoxylin and eosin. The sections were transferred to dH$_2$O for 1 min and then haematoxylin (Carl Roth, Karlsruhe, Germany) for 1 min; after washing in tap water for approximately 5 min, they were transferred to eosin Y (Sigma-Aldrich) for 1 min. The sections were subsequently dehydrated using an increasing alcohol solution series [70%, 90%, and 100% ethanol (Merck) and isopropanol (Merck); 30 s each], transferred to xylene (Carl Roth) for at least 2 min, coverslipped, scanned with a Mirax desk slide scanner (Zeiss, Göttingen, Germany) using a 20× magnification

Table 2 Clinical characteristics of patients with cancer

Characteristic	Non-cachectic	Cachectic
Number	23	13
Gender (*n*)		
Male	15	4
Female	8	9
Age (years)		
Mean	67	65
Range	45–88	44–83
Weight (kg)		
Mean	77	64
Range	40–106	41–98
Body mass index (kg/m^2)		
Mean	25.6	22.5
Range	16.2–34.2	15.8–28.4
Weight loss (%)		
Mean	1.0	13.3
Range	0–4.8	7.7–25.5

objective, and co-registered with the respective mass spectrometry imaging data using flexImaging v. 4.0 (Bruker Daltonics).

Matrix-assisted laser desorption/ionization mass spectrometry imaging data analysis

flexImaging software was used for normalization against the root mean square (FTICR) or total ion count [time of flight (TOF)] of all data points. "Virtual microdissection" was performed, defining regions of interest (ROIs) of cross-sectioned muscle fibres and excluding non-muscle tissue components. Specification of ROIs and exportation of spectral data for each ROI were similarly performed using flexImaging.

MATLAB script, including the bioinformatics and image processing toolboxes (v.7.10.0, MathWorks, Natick, MA, USA), was used for subsequent FTICR data processing. In this script, flexImaging-exported spectra were processed using the LIMPIC algorithm.[18] This algorithm includes a baseline subtraction (100 data points window size), resampling (0.001 m/z bin width), and smoothing (Kaiser filter with factor 3) to exclude chemical and electronic noise before peak picking. Peak picking itself was performed with a minimum peak width of 5.0E – 4 m/z, a signal-to-noise threshold of 2, and a minimum intensity threshold of 0.01% for the base peak of each spectrum. To enable direct comparisons between peak lists from different patients, peaks were clustered with a specific mass tolerance (5.0E – 8 * $(m/z)^{2.023}$). TOF peak lists were generated using SCiLS Lab (v2019a, Bremen, Germany). Metabolites, amino acids, and proteins were identified by matching accurate mass data with Metlin (http://metlin.scripps.edu/index.php),[19] the Human Metabolome Database (http://www.hmdb.ca),[20] and the MaTisse database,[21] allowing a window of 4 ppm for metabolites or amino acids.

Ion images were exported by flexImaging as single colour visualizations with a black background. The colour was detected entirely by image processing software and was visualized over the corresponding scanned haematoxylin and eosin-stained tissue. Adenosine monophosphate (AMP), adenosine diphosphate (ADP), adenosine triphosphate (ATP), and energy charge visualization was performed by an in-house developed python script based on the previously published MSIdV tool for mass spectrometry imaging.[22] The remaining heatmap visualizations were received from SCiLS Lab.

Transmission electron microscopy

For transmission electron microscopy (TEM) analysis, fresh-frozen tissues were fixed with 2.5% glutaraldehyde in 0.1 M sodium cacodylate buffer, pH 7.4, and TEM fixation buffer (Electron Microscopy Sciences, Hatfield, USA) at 4 °C. The samples were subsequently post-fixed in 2% aqueous osmium tetraoxide 44, dehydrated in increasing concentrations of ethanol (30–100%) and propylene oxide, embedded in Epon (Merck, Darmstadt, Germany), and dried for 24 h at 60 °C. Semithin sections were cut and stained with toluidine blue. Ultrathin sections of 50 nm were collected on 200-mesh copper grids and stained with uranyl acetate and lead citrate before examination by TEM (Zeiss Libra 120 Plus, Carl Zeiss NTS GmbH, Oberkochen, Germany). Images were acquired using a Slow Scan CCD camera and iTEM software (Olympus Soft Imaging Solutions, Münster, Germany). The number of mitochondria was determined by manually counting the mitochondria per field of view in longitudinally sectioned fibres, viewed at 1600× magnification.

Immunohistochemistry staining and digital image analysis

For IHC analyses, parts of the mouse muscle tissues were fixed in 4% (v/v) neutral-buffered formalin and embedded in paraffin by an automatic processor. CAT1 analysis of patient tissues was performed on the formalin-fixed paraffin-embedded tissues. Expression levels of CAT1 and voltage-dependent anion channel (VDAC) were analysed on 3 μm consecutive sections by IHC staining with the CAT1 antibody [14195-1-AP (Proteintech, Manchester, UK), 1:20] and VDAC antibody [#4866 (Cell Signaling Technology, Frankfurt am Main, Germany), 1:100]. For validation purposes of mitochondrial proteins, cytochrome c oxidase subunit (COX) 7C [PA5-51284 (Invitrogen, Carlsbad, CA, USA), 1:10] and cytochrome c [GTX108585 (GeneTex, Inc., Alton Pkwy Irvine, CA, USA), 1:25] stainings were performed on 12 μm cryosectioned mouse skeletal muscle tissues. Used tissues are representing consecutive tissue sections as analysed in MALDI imaging. The automated slide processing system Ventana DISCOVERY XT System (Ventana Medical Systems, Inc., Tucson, AZ, USA) was used in accordance with the manufacturer's instructions. All stained slides were digitalized at 20× objective magnification using the Mirax desk slide scanner. IHC staining results were quantified using the image analysis software Definiens Developer XD2 (Definiens AG, Munich, Germany). This software allows quantification of IHC staining intensities within a user-specified ROI. ROIs were defined in longitudinally sectioned muscle fibres. Algorithms were developed, modified specifically for CAT1, VDAC, COX7C, and cytochrome c, and established in semantic and context-based segmentation processes, which included staining intensity, shape, area, colour features, and neighbourhood. In addition, the algorithms were optimized to consider only mitochondrial staining. The quantified parameters for CAT1, VDAC, COX7C, and cytochrome c were values representing a point on a continuous spectrum of protein expression in relative units.

Immunofluorescence analysis of myosin heavy chain expression

Immunofluorescence analysis of myosin heavy chain (MHC) expression was achieved using primary antibodies against MHCI (BA-F8, 1:50), MHCIIa (SC-71, 1:600), and MHCIIb (BF-F3, 1:100) according to Bergmeister *et al.*.[23] Primary antibodies were purchased from the Developmental Studies Hybridoma Bank (University of Iowa), whereas secondary antibodies (AF633 IgG2b, AF488 IgG1, and AF555 IgM, all 1:250) were purchased from Invitrogen. Slides were digitalized at 20× objective magnification using an Axio Scan.Z1 (Zeiss). For fibre-type analysis, all fibres within an ROI (as described for MALDI mass spectrometry imaging) were characterized. Quantification was performed by digital image analysis in Definiens Developer XD2.

Statistical analysis

To determine significant differences between cachectic and non-cachectic tissues, the rank-based Mann–Whitney U test was used. Further statistical testing for functional relationships between and within metabolites, amino acids, and proteins was investigated using Spearman's rank correlation analysis. Correlation plots and calculations were generated and performed using R (The R Foundation, Vienna, Austria; "corrplot" package). P values equal to or less than 0.05 were considered statistically significant.

Results

Amino acid derangements were detected by in situ metabolomics in cachexia

Sixteen amino acids were detected *in situ* in mouse skeletal muscle tissues. Lysine ($P = 0.0037$), arginine ($P = 0.0048$), tyrosine ($P = 0.0357$), and proline ($P = 0.0430$) were significantly more abundant in cachectic mouse muscle tissues than in non-cachectic mice. Alanine, asparagine, glutamine, leucine/isoleucine, methionine, phenylalanine, threonine, tryptophan, and valine analysis revealed a higher relative mean intensity in cachectic mice than in non-cachectic ones, but the differences were not statistically significant (*Figure* 1A). In contrast, quantities of glutamate ($P = 0.0008$) and aspartate ($P = 0.0124$) were significantly less in cachectic mouse skeletal muscle tissues. All intensities and P values of determined amino acids in non-cachectic and cachectic mice can be obtained from Supporting Information, *Appendix S2*. *Figure* 1B shows the results of false colour visualization of amino acids, demonstrating the differences in skeletal muscle tissues between the cachectic and non-cachectic mice.

Results in skeletal muscle tissues of cachectic patients revealed similar amino acid profiles to those observed in mice (Supporting Information, *Appendix S3*); however, the amino acid differences between cachectic and non-cachectic patients did not reach statistical significance. As the amino acid alterations could be due to protein breakdown processes,[2] our subsequent investigations examined this issue.

Amino acids are linked to protein breakdown processes

To detect possible protein breakdown targets, protein expression was determined by MALDI-TOF and correlated with the quantities of amino acids. A negative correlation between amino acids and proteins suggests the presence of protein breakdown.

We determined the correlations between all detected proteins and the quantities of amino acids. Spearman's rank correlation analysis revealed 15 annotated proteins, which have significant negative correlations with amino acid quantities (Supporting Information, *Appendix S4*). The proteins for which significant correlations were detected included thymosin beta-4, individual proteins for oxidative phosphorylation (OXPHOS), histone H2B, and glutathione S-transferase P. Specifically, thymosin beta-4 (*Figure* 2A) correlated negatively with the quantity of lysine ($P = 0.0090$), arginine ($P = 0.0026$), proline ($P = 0.0049$), and threonine ($P = 0.0431$). Cytochrome c oxidase subunit (COX) 6B1 correlated negatively with lysine ($P = 0.0405$), arginine ($P = 0.0027$), glutamine ($P = 0.0209$), and tryptophan ($P = 0.0368$). *Figure* 2B shows an example of the detected proteins: false colour visualization demonstrated lower expression of COX6B1 in cachectic mouse tissues than in non-cachectic mice. Statistical analysis of the visualization results showed significantly decreased COX6B1 in cachexia (*Figure* 2C; $P = 0.0008$). Supporting Information, *Appendix S5* shows the analyses for three OXPHOS proteins: COX7C, ATPase F6, and cytochrome c. At this, the abundances of COX7C and ATPase F6 were significantly decreased ($P = 0.0127$ and $P = 0.0048$, respectively), determined by MALDI mass spectrometry imaging. Interestingly, a majority of detected proteins that correlated negatively with amino acids were associated with the mitochondria. In addition, validation experiments were performed by IHC stainings and confirmed MALDI mass spectrometry imaging analysis results for COX7C as well as for cytochrome c (Supporting Information, *Appendix S5*). COX7C abundance detected by IHC was also significantly decreased ($P = 0.0159$) in cachectic mouse skeletal muscle tissues in comparison with non-cachectic mice.

At this stage, the combination of two different measurement techniques—high-resolution mass spectrometry by FTICR and analysis of proteins by TOF—enabled the detection of biological relationships and thus, for example, the

Figure 1 *In situ* analysis of amino acids in cachectic mouse skeletal muscle tissues. (A) Quantities of amino acids in skeletal muscles from cachectic and non-cachectic mice. All intensity values were determined by mass spectrometry imaging. Quantities of lysine, arginine, proline, and tyrosine were significantly higher in cachectic mice than in non-cachectic ones. The intensities for alanine, asparagine, glutamine, leucine/isoleucine, methionine, phenylalanine, threonine, tryptophan, and valine also revealed a higher relative mean intensity in cachectic mice than in non-cachectic ones. Glutamate and aspartate intensities were significantly decreased in cachectic mouse muscles. Whiskers of the boxplots illustrate the minimal and maximum intensity values. (B) False colour visualization of amino acids in mouse skeletal muscle tissues. Lysine, arginine, and proline were increased, and glutamate and aspartate were decreased in cachectic mouse muscles, compared with non-cachectic ones. $^{*}P < 0.05$, $^{**}P < 0.01$, and $^{***}P < 0.005$. H&E, haematoxylin and eosin.
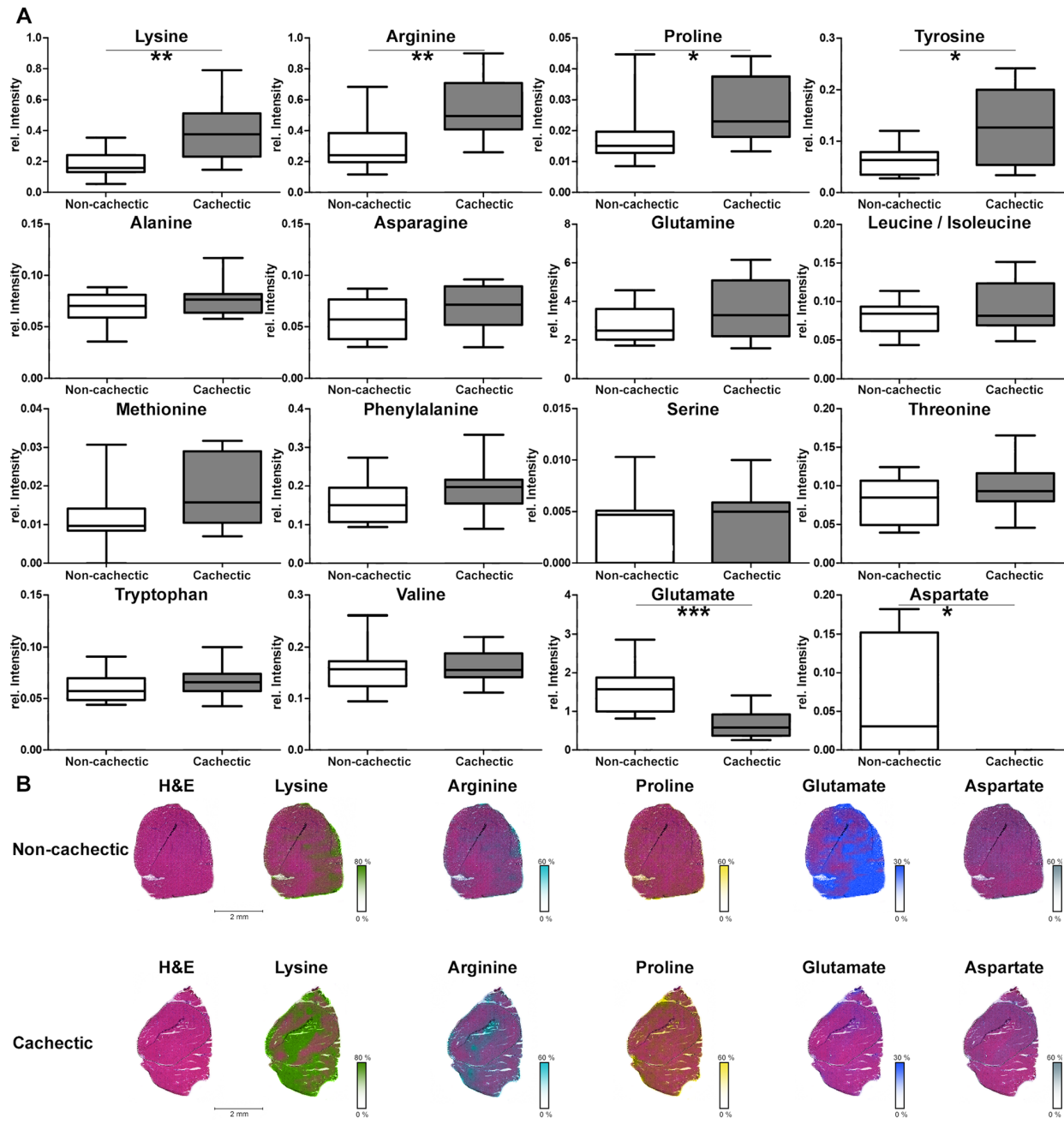
Figure 2 Evaluation of potential protein breakdown targets. (A) Visualization of Spearman's rank correlation analysis results examining the relationships between amino acids and proteins. Square sizes represent the magnitude of the Spearman's rank correlation coefficient. Blue squares indicate positive correlations, and red squares indicate negative correlations. Non-significant correlations ($P > 0.05$) are indicated by empty squares. Many OXPHOS proteins seemed to be degraded. (B) False colour visualization of COX6B1. A reduced quantity of COX6B1 was observed in cachectic mouse tissues, compared with non-cachectic ones. (C) Statistical analysis of the false colour visualization results depicted in (B). COX6B1 intensities were significantly lower in cachectic mouse muscle tissues than in non-cachectic ones ($P = 0.0008$). Boxplot whiskers represent the minimum and maximum intensities. ***$P < 0.005$.
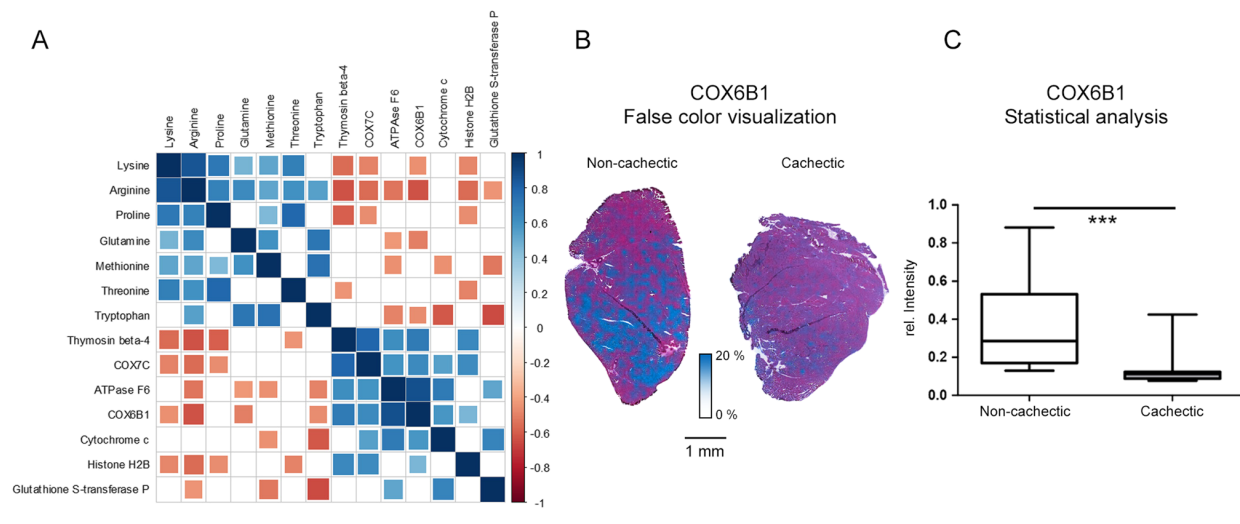
Energy charge is reduced in cachectic muscle tissues

Because the correlation between amino acid and protein data suggested degradation of specific OXPHOS enzymes, we conducted metabolite measurements to examine energy alterations in cachectic mouse skeletal muscle tissues. Because the quadriceps muscle is composed of mixed fibre types, we examined non-cachectic and cachectic mouse skeletal muscle tissues for fibre-type composition. This issue is important for regarding energy aspects, due to the adaption of specific fibre types to oxidative or glycolytic metabolism.[24] No differences could be detected regarding the individual fibre type composition between non-cachectic and cachectic mouse skeletal muscle tissues (Supporting Information, *Appendix S6*).

Adenosine monophosphate, ADP, and ATP concentrations were determined as representatives of the energy state in muscle tissues. To determine the available energy in tissues, the energy charge was calculated from the AMP, ADP, and ATP concentrations, using the formula shown in *Figure* 3A. The energy charge was lower in cachectic mice than in non-

cachectic mice ($P = 0.0101$), indicating that energy stores were reduced in cachectic mouse skeletal muscle tissues. AMP was slightly increased in the cachectic mouse skeletal muscle tissues, when compared with non-cachectic mouse tissues (*Figure* 3B). ADP concentrations were similar in cachectic and non-cachectic mice, and ATP concentration was marginally decreased in cachexia.

Reduced energy in cachectic mouse skeletal muscle tissues could result in changed function of the tricarboxylic acid (TCA) cycle as a compensatory alteration or as a co-influencing factor. In cell metabolomics analysis, the majority of detected TCA cycle molecules did not differ significantly between cachectic and non-cachectic mouse muscle tissues (Supporting Information, *Appendix S7*). However, the quantity of oxaloacetate was significantly decreased ($P = 0.0448$) (*Figure* 3C) and the quantity of malate was significantly increased ($P = 0.0295$) in cachexia. These results indicate that cachexia was not associated with a generalized change in regulation of the TCA cycle, but it did seem to be associated with alterations of the dicarboxylic acid part.

We next used the energy charge results to examine underlying molecular mechanisms. A total of 58 proteins correlated significantly with the calculated energy charge (*Figure* 4). Specifically, COX7C ($P = 0.0257$) and COX6B1 ($P = 0.0052$) were all significantly and positively correlated with the energy charge. Thymosin beta-4 ($P = 0.0054$), histone H2B ($P \leq 0.0001$), and redox Cu/Zn superoxide dismutase ($P = 0.0059$) also correlated positively with the energy charge. Notably, expression of ubiquitin, which is a marker for protein degradation,

Figure 3 Energy changes in cancer cachexia. (A) Heatmap visualization and statistical analysis of the calculated energy charge. Calculation of the energy charge revealed a significantly lower charge in cachectic mice (P = 0.0101). (B) AMP, ADP, and ATP distribution in cachectic and non-cachectic mouse skeletal muscle tissues. No significant differences were detected between cachectic and non-cachectic mouse tissues. (C) Heatmap visualization and statistical analysis of changes in molecules of the tricarboxylic acid cycle. Cachectic mice exhibited significantly higher quantities of malate (P = 0.0295) and lower quantities of oxaloacetate (P = 0.0448) than non-cachectic mice. Whiskers of the boxplots represent the lowest and highest peak intensities in each group. $^*P < 0.05$.

$$\text{Energy charge} = \frac{[\text{ATP}] + \frac{1}{2}[\text{ADP}]}{[\text{ATP}] + [\text{ADP}] + [\text{AMP}]}$$

correlated negatively (P = 0.0009) with the energy charge, as well as with COX7C (P = 0.0216) and other proteins. These proteins may be tagged for degradation.

Five amino acids were also significantly correlated with the energy charge, suggesting a functional relationship. For example, lysine (P = 0.0122) and arginine (P = 0.0086), the quantities of which differed significantly between cachectic and non-cachectic mouse tissues, were correlated negatively with the energy charge (*Figure* 4). Glutamine (P = 0.0108) and leucine/isoleucine (P = 0.0324) were likewise negatively correlated with the energy charge. Glutamate, which was significantly decreased in the cachectic state, correlated positively with the energy charge (P = 0.0437).

Cationic amino acid transporter 1 is changed in cachexia

We next focused on examining changes in CAT1, which was previously identified as an essential factor for L-arginine transport into mitochondria.[25] The potential role of this transport protein in cachexia was supported by our findings of prominent alterations in arginine and lysine, both of which are cationic amino acids.

The quantity of mitochondrial CAT1 in skeletal muscle tissues was lower in cachectic mice than in non-cachectic ones (*Figure* 5A). Using digital image analysis of stained mouse skeletal muscle tissues, significantly less CAT1 was observed in the cachectic state (*Figure* 5B; P = 0.0133). There was a similar tendency towards decreased CAT1 in muscle tissues of cachectic patients, compared with non-cachectic patients, but the difference did not reach statistical significance (P = 0.5498; *Figure* 5C). For comparing an equal group size of patients without gender influence, we also calculated CAT1 expression for female patients alone, which is marginally improving the statistics (P = 0.2261). CAT1 expression was significantly correlated with the quantity of lysine (P = 0.0122; negative correlation), proline (P = 0.0266; negative correlation), and glutamate (P = 0.0106; positive correlation), suggesting an important influence of CAT1 on amino acid quantities in cachectic tissues.

The CAT1 expression results could have been influenced by a change in the number of mitochondria, as fewer mitochondria would lead to reduced quantities of mitochondrial proteins. Therefore, TEM was performed to determine the number and possible morphological alterations of
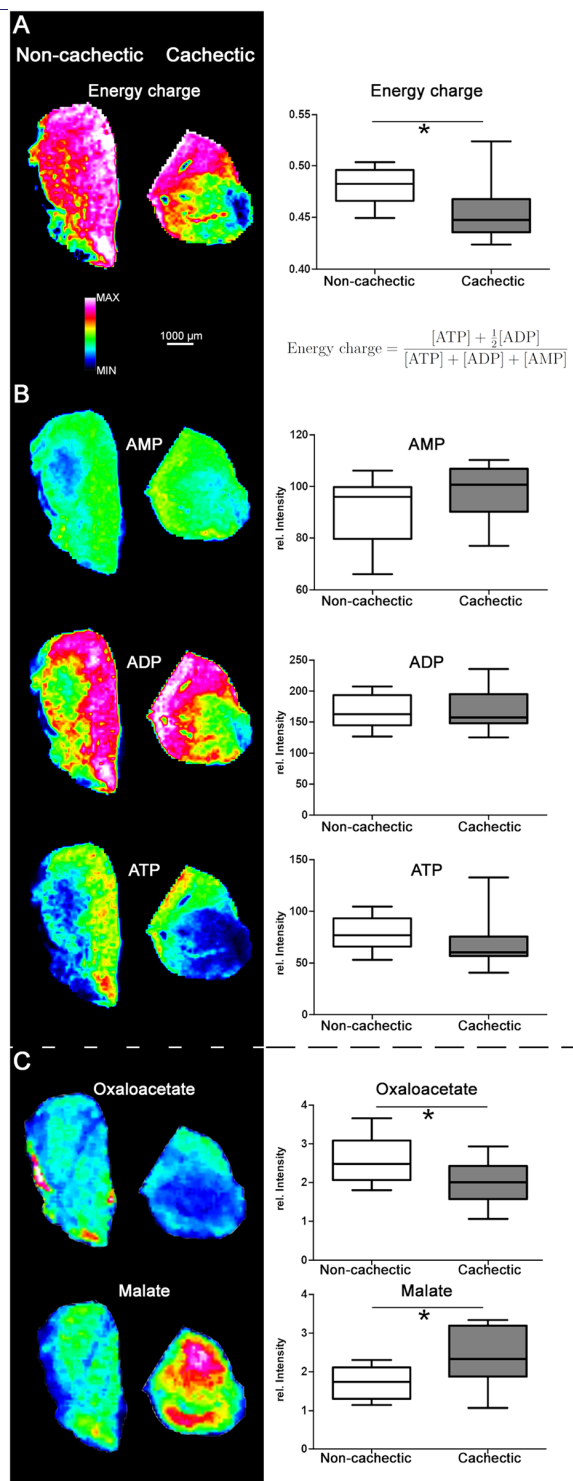
Figure 4 Impact of proteins and amino acids on the energy charge. Correlation plot depicting the results of Spearman's rank analysis examining the associations between amino acid and protein expression and the calculated energy charge. Square size represents the magnitude of the Spearman's rank correlation coefficient. Blue squares indicate positive correlations, and red squares indicate negative correlations. Non-significant correlations ($P > 0.05$) are symbolized by empty squares. Energy charge was significantly correlated with 58 proteins and five amino acids
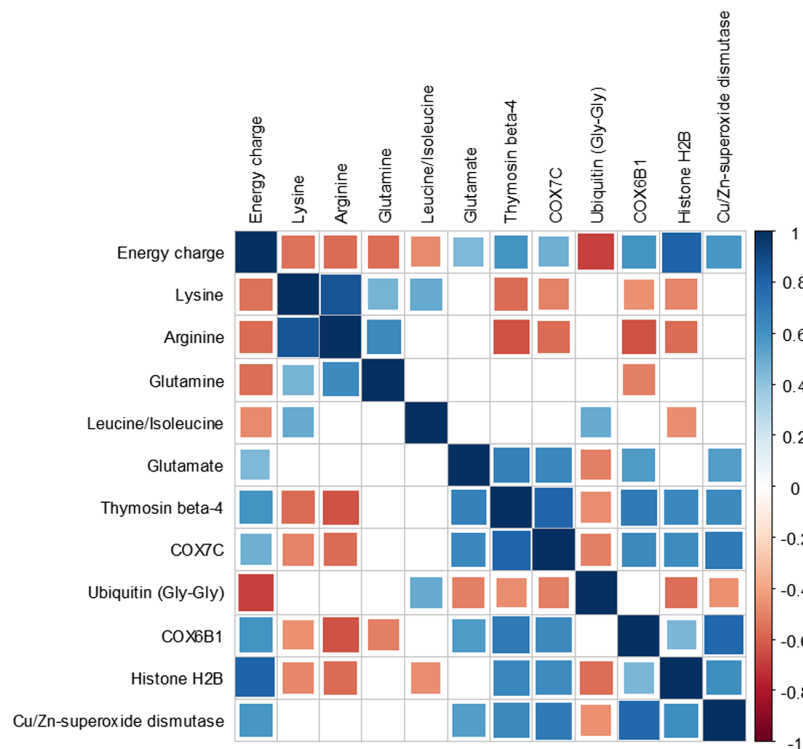
mitochondria in mouse skeletal muscle tissues. No differences in mitochondrial morphology were observed between mitochondria in cachectic and non-cachectic mice; we did not observe electron-lucent areas, swelling, and fragmentation of cristae, which were previously reported in the muscles of mice with cancer cachexia.[26] Similarly, the number of mitochondria was not significantly decreased in the cachectic state (*Figure* 5D and 5E, $P = 0.1051$). Additionally, there were no systematic ultrastructural changes between cachectic and non-cachectic mice.

To provide further evidence of a comparable number of mitochondria in cachectic and non-cachectic mice, VDAC expression was determined by IHC. The quantity of VDAC correlated significantly with the number of mitochondria determined by electron microscopy (*Figure* 5F; $P = 0.0033$) and revealed no significant differences between cachectic and non-cachectic mouse skeletal muscle tissues (*Figure* 5G; $P = 0.5648$). Thus, TEM and VDAC expression confirmed the presence of a similar number of mitochondria in cachectic and non-cachectic mouse skeletal muscle tissues, thereby suggesting a functional—not quantitative—change in mitochondria in cachectic tissues. CAT1 also seemed to be essential for specific aspects of amino acid metabolism in skeletal

muscle cells, with significantly lower expression in cachectic mouse skeletal muscle tissues.

Discussion

In this study, intact skeletal muscle tissues from a murine genetic cancer model were examined for molecular alterations associated with cancer cachexia. For the first time, a combination of three different MALDI mass spectrometry imaging methods was used to explore *in situ* associations between amino acids, proteins, and energy and other cell metabolites in cachectic skeletal muscle tissues. Significant amino acid alterations were detected in cachectic mice, with higher quantities of lysine, arginine, proline, and tyrosine and lower quantities of glutamate and aspartate (*Figure* 1A).

Changes in the quantities of glutamine, isoleucine, leucine, and valine in cachectic skeletal muscle tissues were reported in previous studies.[9–12] However, the specific results were conflicting, as individual studies found lower and/or higher quantities of the same amino acids in cachectic skeletal muscle tissues. Changes of detected abundances could occur because

Figure 5 Changes in CAT1 expression in cachexia. (A) Digital image analysis of the CAT1 immunohistochemistry (IHC) results. Definiens Software Developer XD2 was used to detect the CAT1 expression in all tissue sections. (B) The detected CAT1 abundance was significantly lower in skeletal muscles of cachectic mice than in non-cachectic ones ($P = 0.0133$). Whiskers of the boxplots represent the lowest and highest CAT1 expression in each group. (C) CAT1 expression in skeletal muscle tissues from humans with cancer for all and only female patients. CAT1 was slightly lower in patients with cachexia, compared with non-cachectic patients, but the difference did not reach statistical significance. Horizontal lines represent the mean intensity of each group. (D) Number of mitochondria in mouse skeletal muscle tissues determined by transmission electron microscopy (TEM) at 1600× magnification. The red colour represents the mitochondria. Intact mitochondria were observed in tissues from both cachectic and non-cachectic mice. (E) Boxplots illustrating the number of mitochondria in mouse skeletal muscle tissues. No significant difference was detected between cachectic and non-cachectic mice. (F) Correlation analysis between the number of mitochondria determined by electron microscopy and the intensity of voltage-dependent anion channel (VDAC) staining detected by IHC. The number of mitochondria was significantly correlated with VDAC expression ($P = 0.0033$). (G) Statistical analysis of VDAC staining in muscle tissues from cachectic and non-cachectic mice. No significant difference was detected. $^*P < 0.05$.
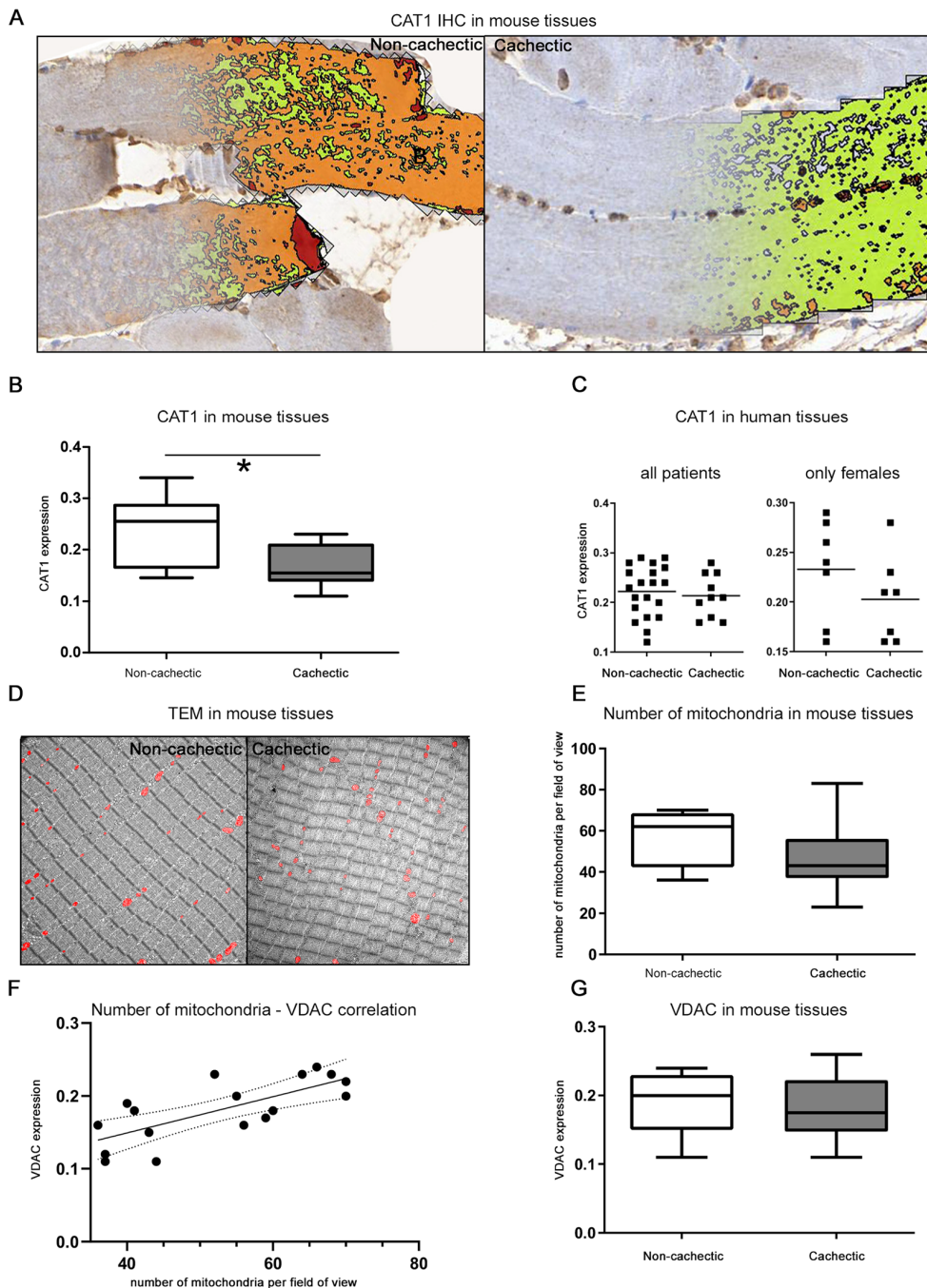
of different analytic platforms, resulting in specific sample preparations, and the individual selected skeletal muscles. Our results in quadriceps muscle tissue and MALDI analysis showed no significant changes towards a higher quantity of all of these amino acids in cachectic skeletal muscle tissues (*Figure* 1A). Furthermore, among all amino acids detected in our study, significant changes were especially noted with cationic amino acids and glutamate. Because lysine, arginine, and glutamate are connected by a biochemical pathway related to mitochondria,[27,28] we focused on mitochondria to understand the detected amino acid alterations. Of note, mitochondrial enzymes catalyze the synthesis of glutamate by transferring the amino group from amino acids such as lysine and arginine to α-ketoglutarate.[27,28] Nonetheless, lysine and arginine must first enter the mitochondria.

CAT1, a transporter molecule in mammalian mitochondria,[25] carries arginine and lysine through membranes.[29] The presence of CAT1 in mitochondria was confirmed by western blot analysis of isolated cardiac mitochondria and by confocal microscopy, and it seemed to be involved in cationic amino acid transport, mitochondrial stress, survival, and diminished reactive oxygen species production.[25] In our study, we detected higher quantities of the cationic amino acids lysine and arginine and a lower quantity of glutamate in the muscles of cachectic mice, compared with non-cachectic ones. We also observed lower expression of CAT1 in cachectic mice. Correlation analysis confirmed significant correlations between CAT1 and lysine, as well as glutamate: low CAT1 expression was associated with more lysine and less glutamate in muscle tissues. These findings may be due to enhanced protein breakdown in cachexia,[30] leading to increased levels of certain amino acids, such as arginine and lysine (*Figure* 6A). Reduced metabolic conversion because of diminished CAT1 expression could also account for the significantly higher quantities of arginine and lysine [*Figure* 6B, (1)]. Of note, our findings are consistent with the results of previous studies, which showed that arginine and lysine were increased in the gastrocnemius of cachectic mice[12] and glutamate was reduced in quadriceps muscles of cachectic C26 hosts.[11] Decreased production of glutamate from arginine and lysine because of reduced transamination reactions could account for the significantly lower quantity of glutamate in cachectic mouse tissues [*Figure* 6B, (2)]. Glutamate production could also be hampered by a low NADH/NAD$^+$ ratio in mitochondria, which would favour oxidative decarboxylation of α-ketoglutarate to succinyl-CoA.[31] An alteration in an electron shuttle system through the inner mitochondrial membrane, for example, could be an explanation for an altered ratio. This may lead to a lower amount of NADH inside mitochondria.

Reduced expression of CAT1 in the muscles of cachectic mice and patients could arise from several mechanisms. For instance, a lower number of mitochondria would reduce mitochondrial CAT1 expression. However, examination of the

tissues with TEM (the gold standard for measuring mitochondrial content[32]) revealed no evidence of a reduced number or altered structural integrity of mitochondria in cachexia (*Figure* 5E). Likewise, examination of mitochondrial content by staining for VDAC (the most abundant protein in the outer membrane of mitochondria[33]) did not show significant differences between cachectic and non-cachectic mice (*Figure* 5G). These results indicate that decreased CAT1 expression is not the result of an altered number of mitochondria; instead, it is due to a specific decrease in expression of the CAT1 protein itself (*Figure* 5B). Thus, decreased mitochondrial CAT1 expression has been described for the first time in cancer cachexia, which may be highly relevant to the amino acid metabolism changes observed in this setting, as discussed earlier.

Manifestations of cachexia can differ according to the type of tumour.[34] In the current study, colorectal and pancreatic cancer revealed similar molecular changes during cachexia. Lysine, arginine, and proline quantities were increased, and glutamate and aspartate were decreased in skeletal muscle tissues of both types of tumours during cachexia. Notably, human material offered only preliminary results in the current study due to the small patient number and further studies, including more patients, are necessary for confirming these molecular alterations. A recent study comparing lung carcinoma and colon adenocarcinoma models under cachectic conditions also found molecular similarities between the two types of malignancies.[35] Despite different food intake in the two models, hypothalamic expression of the orexigenic neuropeptide Y was increased in both tumour types, compared with controls. At this point, our data suggest tumour type-independent molecular alterations, at least for colorectal and pancreatic cancers. Additional studies are necessary to further explore the influence of tumour type on the molecular manifestations of cachexia.

Protein breakdown is highly discussed in the context of cachexia.[2] In the present study, simultaneous examination of proteins and amino acids enabled the identification of proteins that may be selectively degraded in cachectic skeletal muscle tissues. A majority of detected and degraded proteins in this study were OXPHOS proteins, which were negatively correlated with an overabundance of certain amino acids (*Figure* 2A), thereby suggesting the presence of a degradation process. Of note, only small undigested proteins (<25 kDa) are determined by MALDI imaging protein measurement and released amino acids from muscle can not be set into relation with proteins and metabolites in the current study. A recent study of rat gastrocnemius muscles revealed an accumulation of oxidatively modified mitochondrial proteins in cachexia.[36] Oxidative modifications can be repaired enzymatically or lead to protein degradation. Both processes are essential for maintaining homeostasis and survival of cells.[37] Oxidative modifications might also initiate degradation of the OXPHOS proteins

Figure 6 Hypothesis regarding the molecular changes in skeletal muscles during cachexia, focusing on mitochondrial dysfunction. The small red and green arrows indicate molecules for which significant changes were detected in the current study. (A) Proteins in muscle tissues of cachectic mice are degraded and subsequently processed to amino acids. Individual amino acids are then transported into the mitochondria for further metabolism. (B) (1) Lysine (Lys), arginine (Arg), and ornithine (data not shown) are transported via CAT1 into the mitochondria. (2) Specific transaminase proteins metabolize Lys, Arg, ornithine, and other amino acids and produce glutamate. Glutamate is decreased in cachexia because of reduced CAT1 expression. (3) Cytosolic NADH reduces oxaloacetate to malate; it is hypothesized that an increased quantity of cytosolic NADH in cachexia increases the quantity of malate. (4) Malate is exchanged with α-ketoglutarate in the mitochondrial matrix by the malate-α-ketoglutarate transporter.
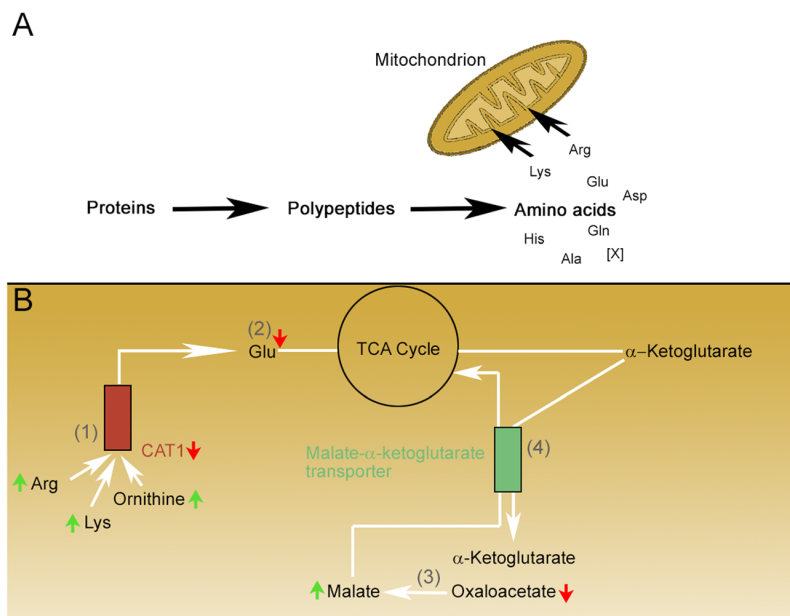
detected in the current study. A previous study found reduced quantity of COX6B1 protein in cachectic mouse tissues, compared with controls,[38] which is consistent with our results (*Figure* 2C). COX6B1 could be altered by oxidative modification and therefore degraded in cachectic skeletal muscle tissues. This degradation could account for the lower quantity of COX6B1 in cachectic skeletal muscle tissues (*Figure* 2C) and the negative correlation between COX6B1 and individual amino acids (*Figure* 2A). Of interest, CAT1 is also involved in reducing oxidative stress.[25] Normal CAT1 expression could help maintain normal protein signatures in mitochondria by preventing oxidative damage and thereby protecting proteins from degradation.

Mitochondria, as well as OXPHOS proteins, are associated with ATP production and, therefore, energy generation in muscle tissues. Given our findings of OXPHOS protein degradation and altered mitochondrial protein signatures during cachexia, we examined the energy status of cachectic skeletal muscle tissues. The energy charge, defined as the mole fraction of ATP plus half the mole fraction of ADP, is linearly related to the amount of temporarily stored metabolically available energy.[39] We found that energy charge was significantly decreased in cachexia. Furthermore, correlation analysis indicated that higher energy charge was associated with a lower quantity of individual amino acids, higher expression

of OXPHOS proteins, and lower expression of ubiquitin. Nonetheless, glutamate correlated positively with the energy charge (*Figure* 4). A reduced rate of ATP synthesis (determined by ^{31}P nuclear magnetic resonance spectroscopy) has been previously described in cancer cachexia.[40] Degradation of mitochondrial OXPHOS proteins could at least partially explain the reduced energy stores in cachectic muscles. As ubiquitin, a marker for protein degradation, can initiate proteasomal degradation,[41] lower ubiquitin tagging could reduce degradation of OXPHOS proteins and the quantity of amino acids but increase the energy charge. The positive correlation between glutamate and energy charge could underlie the anaplerotic processes of glutamate in cancer cachexia.[13]

Reduced energy availability in muscle tissues could lead to higher glycolytic activity, because two NADH and two ATP molecules are produced from one glucose molecule, and the NADH can be utilized for ATP synthesis in mitochondria. However, the inner mitochondrial membrane is impermeable to NADH, so cytosolic NADH must be transported into the mitochondrial matrix by transport systems, such as the malate-aspartate shuttle.[42] High glycolytic activity has been described in cachexia,[12,43] which could lead to high quantities of cytosolic NADH [*Figure* 6B, (3)]. Pin *et al.*[11] formally described an increased reliance on glycolytic metabolism and a

reduced flux of glycolysis-derived pyruvate into the TCA cycle, which might also be followed by reducing energy in cachectic skeletal muscle tissues. Malate dehydrogenase 1 enzyme can utilize NADH to reduce oxaloacetate to malate[44] for transporting electrons from NADH across the inner membrane via the malate-α-ketoglutarate transporter [*Figure* 6B, (4)]. This could account for the low oxaloacetate and high malate quantities found in the current study (*Figure* 3C). High levels of cytosolic NADH may reduce a high amount of oxaloacetate to malate, available for carrying electrons across the inner mitochondrial membrane for ATP synthesis.

To conclude, our data revealed mitochondrial dysfunction in cachectic skeletal muscle tissue, which appeared to have a substantial influence on amino acid metabolism and protein breakdown, based on several lines of evidence. Firstly, we observed significant accumulation of lysine and arginine in cachexia, which can be metabolized in mitochondria to glutamate.[27,28] Secondly, indices of degradation suggested the presence of degradation of mitochondrial OXPHOS proteins. Thirdly, the energy charge was reduced in cachexia, which may be at least partly attributed to mitochondrial dysfunction. Finally, cachectic muscle tissues exhibited significantly reduced expression of the mitochondrial protein CAT1, which may play an important role in the observed molecular changes associated with cachexia.

Acknowledgements

Conflict of interest

None declared.

Funding

Online supplementary material

Additional supporting information may be found online in the Supporting Information section at the end of the article.

Appendix S1. Advanced baseline characteristics for patients, which is separating patient material in individual fixation methods. FFPE tissues were used for immunohistochemical staining, and fresh frozen tissues were used for the determination of amino acids.

Appendix S2. Intensities of amino acids in skeletal muscle tissues of cachectic and non-cachectic mice. *P* values were calculated by Mann–Whitney *U* test.

Appendix S3. *In situ* amino acid quantities in skeletal muscle tissues from cachectic patients with cancer. Changes in lysine, arginine, proline, glutamate, and aspartate with cachexia in humans revealed similarities to the changes observed in cachectic mouse skeletal muscle tissues. The horizontal lines represent the mean intensity of each group.

Appendix S4. *P* values (Spearman's rank correlation analysis) of significant negative correlations between proteins and amino acids. Included proteins were may degraded in skeletal muscle tissues of cachectic mice.

Appendix S5. Analysis of mitochondrial proteins in mouse skeletal muscle tissues (A) Statistical analysis for the OXPHOS-related proteins COX7C, cytochrome c, and ATPase F6 determined by MALDI mass spectrometry imaging. COX7C ($P = 0.0127$) and ATPase F6 ($P = 0.0048$) expression was significantly decreased in cachexia, compared with non-cachectic skeletal muscle tissues. Cytochrome c was also decreased in cachectic mouse skeletal muscle tissues, but the differences did not reach statistical significance ($P = 0.1145$). (B) Immunohistochemistry (IHC) results confirmed changes of mitochondrial proteins detected by MALDI mass spectrometry imaging. Quantification of the IHC, performed by digital image analysis, revealed a lower expression of COX7C in cachectic mouse skeletal muscle tissues ($P = 0.0159$) and a similar change of cytochrome c without reaching significance level ($P = 0.2512$). * $P < 0.05$, ** $P < 0.01$.

Appendix S6. Immunofluorescence analysis of myosin heavy chain (MHC) expressions. (A) Statistical analysis of the expression of myosin heavy chains in cachectic and non-cachectic mouse skeletal muscle tissues. MHC1 expressions were in both comparison groups 0.02%. The Mann–Whitney *U* test was performed for all fibre types and revealed no significant change between non-cachectic and cachectic mouse comparison groups. (B) Exemplary pictures for immunofluorescence stained cross-sectioned mouse skeletal muscle tissues. The left tissue section is representing a non-cachectic mouse,

whereby the right tissue is belonging to a cachectic mouse. Shown are type I (blue), type IIA (green), type IIB (red), and type IIX (unstained) fibres.

Appendix S7. Statistical analysis regarding changes of molecules in the tricarboxylic acid (TCA) cycle. Peak intensity was significantly higher for malate (P = 0.0295) and lower for oxaloacetate (P = 0.0448) in tissues of cachectic mice, compared with non-cachectic ones. Boxplot whiskers represent the lowest and highest peak intensities in each group. * $P < 0.05$.

References

1. Tisdale MJ. Cachexia in cancer patients. *Nat Rev Cancer* 2002;**2**:862–871.

2. Argiles JM, Busquets S, Stemmler B, Lopez-Soriano FJ. Cancer cachexia: understanding the molecular basis. *Nat Rev Cancer* 2014;**14**:754–762.

3. Pisters PW, Pearlstone DB. Protein and amino acid metabolism in cancer cachexia: investigative techniques and therapeutic interventions. *Crit Rev Clin Lab Sci* 1993;**30**:223–272.

4. Khal J, Wyke SM, Russell ST, Hine AV, Tisdale MJ. Expression of the ubiquitin–proteasome pathway and muscle loss in experimental cancer cachexia. *Br J Cancer* 2005;**93**:774–780.

5. Sandri M. Protein breakdown in cancer cachexia. *Semin Cell Dev Biol* 2016;**54**:11–19.

6. Cornwell EW, Mirbod A, Wu CL, Kandarian SC, Jackman RW. C26 cancer-induced muscle wasting is Iκκβ-dependent and NF-κβ-independent. *PLoS ONE* 2014;**9**:e87776.

7. Duval AP, Jeanneret C, Santoro T, Dormond O. mTOR and Tumor Cachexia. *Int J Mol Sci* 2018;**19**.

8. White JP, Baynes JW, Welle SL, Kostek MC, Matesic LE, Sato S, et al. The regulation of skeletal muscle protein turnover during the progression of cancer cachexia in the Apc (Min/+) mouse. *PLoS ONE* 2011;**6**: e24650.

9. Tseng YC, Kulp SK, Lai IL, Hsu EC, He WA, Frankhouser DE, et al. Preclinical investigation of the novel histone deacetylase inhibitor AR-42 in the treatment of cancer-induced cachexia. *J Natl Cancer Inst* 2015;**107**:djv274.

10. QuanJun Y, GenJin Y, LiLi W, Yan H, YongLong H, Jin L, et al. Integrated analysis of serum and intact muscle metabonomics identify metabolic profiles of cancer cachexia in a dynamic mouse model. *RSC Adv* 2015;**5**:92438–92448.

11. Pin F, Barreto R, Couch ME, Bonetto A, O'Connell TM. Cachexia induced by cancer and chemotherapy yield distinct perturbations to energy metabolism. *J Cachexia Sarcopenia Muscle* 2019;**10**:140–154.

12. Der-Torossian H, Wysong A, Shadfar S, Willis MS, McDunn J, Couch ME. Metabolic derangements in the gastrocnemius and the effect of compound A therapy in a murine model of cancer cachexia. *J Cachexia Sarcopenia Muscle* 2013;**4**:145–155.

13. Rutten EP, Engelen MP, Schols AM, Deutz NE. Skeletal muscle glutamate metabolism in health and disease: state of the art. *Curr Opin Clin Nutr Metab Care* 2005;**8**:41–51.

14. Dickinson JM, Rasmussen BB. Amino acid transporters in the regulation of human skeletal muscle protein metabolism. *Curr Opin Clin Nutr Metab Care* 2013;**16**:638–644.

15. Janssen KP, Alberici P, Fsihi H, Gaspar C, Breukel C, Franken P, et al. APC and oncogenic KRAS are synergistic in enhancing Wnt signaling in intestinal tumor formation and progression. *Gastroenterology* 2006; **131**:1096–1109.

16. Fearon K, Strasser F, Anker SD, Bosaeus I, Bruera E, Fainsinger RL, et al. Definition and classification of cancer cachexia: an international consensus. *Lancet Oncol* 2011;**12**:489–495.

17. Ly A, Buck A, Balluff B, Sun N, Gorzolka K, Feuchtinger A, et al. High-mass-resolution MALDI mass spectrometry imaging of metabolites from formalin-fixed paraffin-embedded tissue. *Nat Protoc* 2016; **11**:1428–1443.

18. Mantini D, Petrucci F, Pieragostino D, Del Boccio P, Di Nicola M, Di Ilio C, et al. LIMPIC: a computational method for the separation of protein MALDI-TOF-MS signals from noise. *BMC Bioinformatics* 2007;**8**:101.

19. Guijas C, Montenegro-Burke JR, Domingo-Almenara X, Palermo A, Warth B, Hermann G, et al. METLIN: a technology platform for identifying knowns and unknowns. *Anal Chem* 2018;**90**:3156–3164.

20. Wishart DS, Tzur D, Knox C, Eisner R, Guo AC, Young N, et al. HMDB: the human metabolome database. *Nucleic Acids Res* 2007;**35**:D521–D526.

21. Maier SK, Hahne H, Gholami AM, Balluff B, Meding S, Schoene C, et al. Comprehensive identification of proteins from MALDI imaging. *Mol Cell Proteomics* 2013;**12**: 2901–2910.

22. Hayakawa E, Fujimura Y, Miura D. MSIdV: a versatile tool to visualize biological indices from mass spectrometry imaging data. *Bioinformatics* 2016;**32**:3852–3854.

23. Bergmeister KD, Groger M, Aman M, Willensdorfer A, Manzano-Szalai K, Salminger S, et al. A rapid automated protocol for muscle fiber population analysis in rat muscle cross sections using myosin heavy chain immunohistochemistry. *J Vis Exp* 2017.

24. Schiaffino S, Reggiani C. Fiber types in mammalian skeletal muscles. *Physiol Rev* 2011;**91**:1447–1531.

25. Williams D, Venardos KM, Byrne M, Joshi M, Horlock D, Lam NT, et al. Abnormal mitochondrial ʟ-arginine transport contributes to the pathogenesis of heart failure and rexoygenation injury. *PLoS ONE* 2014;**9**:e104643.

26. Shum AM, Mahendradatta T, Taylor RJ, Painter AB, Moore MM, Tsoli M, et al. Disruption of MEF2C signaling and loss of sarcomeric and mitochondrial integrity in cancer-induced skeletal muscle wasting. *Aging (Albany NY)* 2012;**4**:133–143.

27. Papes F, Surpili MJ, Langone F, Trigo JR, Arruda P. The essential amino acid lysine acts as precursor of glutamate in the mammalian central nervous system. *FEBS Lett* 2001;**488**:34–38.

28. Morris SM Jr. Regulation of enzymes of the urea cycle and arginine metabolism. *Annu Rev Nutr* 2002;**22**:87–105.

29. Hatzoglou M, Fernandez J, Yaman I, Closs E. Regulation of cationic amino acid transport: the story of the CAT-1 transporter. *Annu Rev Nutr* 2004;**24**:377–399.

30. Argiles JM, Lopez-Soriano FJ. The ubiquitin-dependent proteolytic pathway in skeletal muscle: its role in pathological states. *Trends Pharmacol Sci* 1996;**17**:223–226.

31. Frigerio F, Casimir M, Carobbio S, Maechler P. Tissue specificity of mitochondrial glutamate pathways and the control of metabolic homeostasis. *Biochim Biophys Acta* 2008;**1777**:965–972.

32. Larsen S, Nielsen J, Hansen CN, Nielsen LB, Wibrand F, Stride N, et al. Biomarkers of mitochondrial content in skeletal muscle of healthy young human subjects. *J Physiol* 2012;**590**:3349–3360.

33. Kroemer G, Reed JC. Mitochondrial control of cell death. *Nat Med* 2000;**6**:513–519.

34. Tisdale MJ. Mechanisms of cancer cachexia. *Physiol Rev* 2009;**89**:381–410.

35. Dwarkasing JT, Boekschoten MV, Argiles JM, van Dijk M, Busquets S, Penna F, et al. Differences in food intake of tumour-bearing cachectic mice are associated with hypothalamic serotonin signalling. *J Cachexia Sarcopenia Muscle* 2015;**6**:84–94.

36. Padrao AI, Oliveira P, Vitorino R, Colaco B, Pires MJ, Marquez M, et al. Bladder cancer-induced skeletal muscle wasting: disclosing the role of mitochondria plasticity. *Int J Biochem Cell Biol* 2013;**45**: 1399–1409.

37. Bulteau AL, Szweda LI, Friguet B. Mitochondrial protein oxidation and degradation in response to oxidative stress and aging. *Exp Gerontol* 2006;**41**:653–657.

38. Shum AMY, Poljak A, Bentley NL, Turner N, Tan TC, Polly P. Proteomic profiling of skeletal and cardiac muscle in cancer cachexia: alterations in sarcomeric and

mitochondrial protein expression. *Oncotarget* 2018;**9**:22001–22022.

39. Atkinson DE. The energy charge of the adenylate pool as a regulatory parameter. Interaction with feedback modifiers. *Biochemistry* 1968;**7**:4030–4034.

40. Constantinou C, Fontes de Oliveira CC, Mintzopoulos D, Busquets S, He J, Kesarwani M, et al. Nuclear magnetic resonance in conjunction with functional genomics suggests mitochondrial dysfunction in a murine model of cancer cachexia. *Int J Mol Med* 2011;**27**:15–24.

41. Lecker SH, Goldberg AL, Mitch WE. Protein Degradation by the ubiquitin–proteasome pathway in normal and disease states. *J Am Soc Nephrol* 2006;**17**:1807–1819.

42. Kovacevic Z. Possibility for the transfer of reducing equivalents from the cytosol to the mitochondrial compartment in Ehrlich ascites tumor cells by the malate-aspartate shuttle. *Eur J Biochem* 1972;**25**:372–378.

43. Mantovani G. *Cachexia and wasting a modern approach*. Milan: Springer; 2006.

44. Mitchell M, Cashman KS, Gardner DK, Thompson JG, Lane M. Disruption of mitochondrial malate-aspartate shuttle activity in mouse blastocysts impairs viability and fetal growth. *Biol Reprod* 2009;**80**: 295–301.

45. von Haehling S, Morley JE, Coats AJS, Anker SD. Ethical guidelines for publishing in the *Journal of Cachexia, Sarcopenia and Muscle*: update 2017. *J Cachexia Sarcopenia Muscle* 2017;**8**:1081–1083.

4. Discussion and Outlook

This thesis aimed and accomplished to provide new insights into cancer metabolism and address unmet clinical needs in cancer therapy by initially developing [1, 2] and extensively applying [3, 4] an improved spatial metabolomics method. Improved spatial metabolomics was demonstrated to integrate several molecular layers by keeping spatial information intact and to improve the prognostic effect of biomarkers strikingly [1, 2]. The improved spatial metabolomics method provided new insights into the cancer metabolism of patients. It served answers to clinical questions by providing new aspects for targeted anti-HER2 and anti-PD-1/PD-L1 therapies, and revealing potential therapeutic targets in cancer cachexia [1, 2, 3, 4].

The publications entitled "Multimodal analysis of formalin-fixed and paraffin-embedded tissue by MALDI imaging and fluorescence *in situ* hybridization for combined genetic and metabolic analysis" [1] and "*De novo* discovery of metabolic heterogeneity with immunophenotype-guided imaging mass spectrometry" [2] prove the feasibility and the importance of combining different molecular layers for biomarker discovery. On the one hand, the statistical power was significantly improved by combining genetics with metabolomics. This thesis demonstrated that AMP abundance and *HER2/CEP17* gene copy numbers reveal a significant association with patient survival; however, the combination of both strikingly improves the prognostic effect. On the other hand, spatially resolved integration of both modalities, genetics, and metabolomics is for the first time possible by utilizing the newly created SPACiAL imaging pipeline [2]. In contrast, without this new imaging pipeline, integration of the individual imaging modalities would be accomplished by visually overlaying the images generated by each technique. However, simple image overlays hamper quantitative correlations since the images have different coordinate systems and orientations [98]. The SPACiAL imaging pipeline addressed this problem. The thesis presents a more sophisticated multimodal registration method allowing pixel-wise analysis of tissue sections by matching the coordinate systems of each imaging modality.

The significance of the two publications [1, 2] is underlined by a recent study by Lu and colleagues [99]. The authors aimed to compare the relative diagnostic performance of PD-L1 IHC, tumor mutational burden, gene expression profiling, and multiplex

4. Discussion and Outlook

IHC/immunofluorescence assays to assess pretreatment tumor tissue to predict response to anti-PD-1/PD-L1 therapies. The authors conducted a search in PubMed, which leads to the result that multimodality biomarker strategies seem to be associated with improved performance over PD-L1 IHC, tumor mutational burden, or gene expression profiling alone. In addition, the authors assume an improved diagnostic benefit by considering spatial relationships. This thesis describes the same enhancement in performance by using our multimodal biomarker strategy enabled by the improved spatial metabolomics method. The synergism between genetics and metabolomics strikingly improves the prognostic effect in contrast to each modality alone [1]. In addition, the newly created SPACiAL pipeline enables integrating a multitude of imaging modalities and maintaining the spatial relationships between each modality, leading the discovery of superior biomarkers for targeted anti-cancer therapy response prediction [2].

One crucial milestone provided by the SPACiAL pipeline is the feasibility of analyzing the tumor cell specific metabolome of huge patient cohorts. Tumor and tumor stroma-specific regions can be detected by IHC and, therefore, virtual microdissection can be automatically performed on stained areas. Before SPACiAL, tumor and tumor stroma regions were often defined handish and required strong expertise and considerable time. Therefore, the SPACiAL pipeline increases the usability of spatial metabolomics in clinics for decision-making.

An ongoing challenge is finding biomarkers that reflect the exposome of patients [100]. So far, details of the exposome are normally analyzed by questionnaires administered to patients in the clinic [100]. In particular, for lung cancer, information about smoking behavior is important to stratify people into subtypes for risk of lung cancer [100]. Unfortunately, questionnaire responses are biased and error-prone [100]. With the study "Patterns of carbon-bound exogenous compounds in patients with lung cancer and association with disease pathophysiology" [3], this thesis presents an entirely new approach that could replace biomarkers in this context. Instead of finding biomarkers reflecting the exposome, this thesis supposes to measure the lung exposome directly in the patient's lung. For the first time, the *in situ* measurement of the exposome is associated with several tumor biological features. However, obtaining patient biopsies from the lung is still a high-risk procedure that could be reduced by advanced methods in the future.

In contrast to cancer, there are no definitive therapies for cancer cachexia. Highlighting molecular changes in cancer cachexia raises the probability of finding drug targets for enabling definitive therapies. Our study, entitled "Derangements of amino acids in cachectic skeletal muscle are caused by mitochondrial dysfunction" [4], illuminates *in situ* changes of amino acids in cancer cachexia affected skeletal muscle tissues. In particular,

lysine and arginine were revealed to be increased in cachectic skeletal muscle tissues; in contrast, aspartate was decreased. Sadek and colleagues investigated the mechanism of action of inducible nitric oxide synthase (iNOS), one of the main effectors of cachexia [101]. The authors revealed that iNOS knockout mice and mice treated with the clinically tested iNOS inhibitor are protected against muscle wasting in septic and cancer cachexia models. Furthermore, the authors discovered that iNOS initiates muscle wasting by disrupting mitochondrial content, morphology, and energy production processes such as the TCA cycle and inhibits oxidative phosphorylation. The authors confirmed our data that arginine and lysine are increased, and aspartate is decreased in cachectic muscle tissues. Interestingly, the iNOS inhibitor recovers the level of lysine, arginine, and aspartate in muscle tissues. The effector iNOS could play an important role in triggering mitochondrial dysfunction in cancer cachexia and illustrates a promising mechanism as a target for anti-cancer-cachexia therapy.

SPACiAL offers a platform for the integration of multiple spatially resolved tissue data [2]. The presented work in this thesis could potentially be continued by integrating new spatial *omics* technologies as additional molecular layers in the future. Spatial transcriptomics is one promising option since recent technological developments allow to measure RNA expression levels of all or most genes systematically in tissue sections [102]. In more detail, next-generation sequencing (NGS)-based spatial transcriptomics encodes positional information onto transcripts prior to sequencing [102]. Spatially barcoded microarray slides are often needed for NGS-based spatial transcriptomics. Since FT-ICR-based spatial transcriptomics can handle non-conductive slides - e.g., barcoded microarray slides - it could be worth analyzing a tissue previously measured by spatial metabolomics using spatial transcriptomics to enable pixel-accurate integration. The feasibility is underlined by our work, which reveals that the genetic information is still intact after spatial metabolomics [1]. Spatial metabolomics and spatial transcriptomics could be integrated by the SPACiAL pipeline [2].

As a new spatial omics technology, Zhao and colleagues recently introduced spatial genomics, a method for capturing spatially resolved DNA sequences from intact tissue sections [103]. The method uses barcoded bead arrays to capture spatially resolved genome-wide expression, similar to slide-RNA-seq. It would be interesting to also combine spatial genomics with spatial metabolomics. The integration of as many individual molecular layers as possible could lead to a significant step in understanding cancer by creating a comprehensive molecular view.

4. Discussion and Outlook

Improved spatial metabolomics offers a new perspective in the cancer metabolism of patients through the spatially resolved integration of multiple molecular layers. The improved method was proven in this thesis to answer unmet clinical needs in cancer therapy by enabling superior multimodal biomarkers and new knowledge for anti-HER2 and anti-PD-1/PD-L1 treatment and highlights important mechanisms for targeting cancer cachexia. Therefore, this thesis significantly contributes to the applicability of spatial metabolomics in clinical diagnostics and preclinical research. The published studies revealed the potential for spatial metabolomics to assist clinical decision-making.

Bibliography

[1] Huber, K. *et al.* Multimodal analysis of formalin-fixed and paraffin-embedded tissue by MALDI imaging and fluorescence in situ hybridization for combined genetic and metabolic analysis. *Laboratory Investigation* **99**, 1535–1546 (2019).

[2] Prade, V. M. *et al.* De novo discovery of metabolic heterogeneity with immunophenotype-guided imaging mass spectrometry. *Molecular Metabolism* **36**, 100953 (2020).

[3] Kunzke, T. *et al.* Patterns of carbon-bound exogenous compounds in patients with lung cancer and association with disease pathophysiology. *Cancer Research* **81**, 5862–5875 (2021).

[4] Kunzke, T. *et al.* Derangements of amino acids in cachectic skeletal muscle are caused by mitochondrial dysfunction. *Journal of Cachexia, Sarcopenia and Muscle* **11**, 226–240 (2019).

[5] Counihan, J. L., Grossman, E. A. & Nomura, D. K. Cancer metabolism: Current understanding and therapies. *Chemical Reviews* **118**, 6893–6923 (2018).

[6] Wishart, D. S. Is cancer a genetic disease or a metabolic disease? *EBioMedicine* **2**, 478–479 (2015).

[7] Boroughs, L. K. & DeBerardinis, R. J. Metabolic pathways promoting cancer cell survival and growth. *Nature Cell Biology* **17**, 351–359 (2015).

[8] McGuirk, S., Audet-Delage, Y. & St-Pierre, J. Metabolic fitness and plasticity in cancer progression. *Trends in Cancer* **6**, 49–61 (2020).

[9] Wishart, D. S. Metabolomics for investigating physiological and pathophysiological processes. *Physiological Reviews* **99**, 1819–1875 (2019).

[10] Faubert, B., Solmonson, A. & DeBerardinis, R. J. Metabolic reprogramming and cancer progression. *Science* **368**, eaaw5473 (2020).

[11] Hirschey, M. D. *et al.* Dysregulated metabolism contributes to oncogenesis. *Seminars in Cancer Biology* **35**, S129–S150 (2015).

[12] Warburg, O., Wind, F. & Negelein, E. THE METABOLISM OF TUMORS IN THE BODY. *Journal of General Physiology* **8**, 519–530 (1927).

[13] Bernier, M. *et al.* GPR55 receptor antagonist decreases glycolytic activity in PANC-1 pancreatic cancer cell line and tumor xenografts. *International Journal of Cancer* **141**, 2131–2142 (2017).

[14] Hirschhaeuser, F., Sattler, U. G. & Mueller-Klieser, W. Lactate: A metabolic key player in cancer: Figure 1. *Cancer Research* **71**, 6921–6925 (2011).

[15] Chen, Y.-J. *et al.* Differential incorporation of glucose into biomass during warburg metabolism. *Biochemistry* **53**, 4755–4757 (2014).

[16] Fischer, K. *et al.* Inhibitory effect of tumor cell–derived lactic acid on human t cells. *Blood* **109**, 3812–3819 (2007).

[17] Ookhtens, M., Kannan, R., Lyon, I. & Baker, N. Liver and adipose tissue contributions to newly formed fatty acids in an ascites tumor. *American Journal of Physiology-Regulatory, Integrative and Comparative Physiology* **247**, R146–R153 (1984).

[18] Carracedo, A., Cantley, L. C. & Pandolfi, P. P. Cancer metabolism: fatty acid oxidation in the limelight. *Nature Reviews Cancer* **13**, 227–232 (2013).

[19] Vazquez-Martin, A., Colomer, R., Brunet, J. & Menendez, J. Pharmacological blockade of fatty acid synthase (FASN) reverses acquired autoresistance to trastuzumab (herceptin™) by transcriptionally inhibiting 'HER2 super-expression' occurring in high-dose trastuzumab-conditioned SKBR3/tzb100 breast cancer cells. *International Journal of Oncology* (2007).

[20] Kwan, H. Y. *et al.* Dietary lipids and adipocytes: potential therapeutic targets in cancers. *The Journal of Nutritional Biochemistry* **26**, 303–311 (2015).

[21] Schafer, Z. T. *et al.* Antioxidant and oncogene rescue of metabolic defects caused by loss of matrix attachment. *Nature* **461**, 109–113 (2009).

[22] Locasale, J. W. Serine, glycine and one-carbon units: cancer metabolism in full circle. *Nature Reviews Cancer* **13**, 572–583 (2013).

[23] Ding, W. *et al.* s-adenosylmethionine levels govern innate immunity through distinct methylation-dependent pathways. *Cell Metabolism* **22**, 633–645 (2015).

[24] Villa, E., Ali, E., Sahu, U. & Ben-Sahra, I. Cancer cells tune the signaling pathways to empower de novo synthesis of nucleotides. *Cancers* **11**, 688 (2019).

[25] Tong, X., Zhao, F. & Thompson, C. B. The molecular determinants of de novo nucleotide biosynthesis in cancer cells. *Current Opinion in Genetics & Development* **19**, 32–37 (2009).

[26] Lane, A. N. & Fan, T. W.-M. Regulation of mammalian nucleotide metabolism and biosynthesis. *Nucleic Acids Research* **43**, 2466–2485 (2015).

[27] Kollareddy, M. *et al.* Regulation of nucleotide metabolism by mutant p53 contributes to its gain-of-function activities. *Nature Communications* **6** (2015).

[28] Yang, M., Soga, T., Pollard, P. J. & Adam, J. The emerging role of fumarate as an oncometabolite. *Frontiers in Oncology* **2** (2012).

[29] Kim, J. & DeBerardinis, R. J. Mechanisms and implications of metabolic heterogeneity in cancer. *Cell Metabolism* **30**, 434–446 (2019).

[30] Borniger, J. C. *et al.* A role for hypocretin/orexin in metabolic and sleep abnormalities in a mouse model of non-metastatic breast cancer. *Cell Metabolism* **28**, 118–129.e5 (2018).

[31] Baazim, H., Antonio-Herrera, L. & Bergthaler, A. The interplay of immunology and cachexia in infection and cancer. *Nature Reviews Immunology* (2021).

[32] Biswas, A. K. & Acharyya, S. Understanding cachexia in the context of metastatic progression. *Nature Reviews Cancer* **20**, 274–284 (2020).

[33] Argilés, J. M., Stemmler, B., López-Soriano, F. J. & Busquets, S. Inter-tissue communication in cancer cachexia. *Nature Reviews Endocrinology* **15**, 9–20 (2018).

[34] Fearon, K. *et al.* Definition and classification of cancer cachexia: an international consensus. *The Lancet Oncology* **12**, 489–495 (2011).

[35] Roeland, E. J. *et al.* Management of cancer cachexia: ASCO guideline. *Journal of Clinical Oncology* **38**, 2438–2453 (2020).

[36] Siddiqui, J. A., Pothuraju, R., Jain, M., Batra, S. K. & Nasser, M. W. Advances in cancer cachexia: Intersection between affected organs, mediators, and pharmacological interventions. *Biochimica et Biophysica Acta (BBA) - Reviews on Cancer* **1873**, 188359 (2020).

[37] Hopkinson, J. B., Wright, D. N., McDonald, J. W. & Corner, J. L. The prevalence of concern about weight loss and change in eating habits in people with advanced cancer. *Journal of Pain and Symptom Management* **32**, 322–331 (2006).

[38] Grande, A. J. *et al.* Exercise for cancer cachexia in adults. *Cochrane Database of Systematic Reviews* **2021** (2021).

[39] Prado, C. M. *et al.* Central tenet of cancer cachexia therapy: do patients with advanced cancer have exploitable anabolic potential? *The American Journal of Clinical Nutrition* **98**, 1012–1019 (2013).

[40] Prado, C. M. M. *et al.* Skeletal muscle anabolism is a side effect of therapy with the MEK inhibitor: selumetinib in patients with cholangiocarcinoma. *British Journal of Cancer* **106**, 1583–1586 (2012).

[41] Ni, X., Yang, J. & Li, M. Imaging-guided curative surgical resection of pancreatic cancer in a xenograft mouse model. *Cancer Letters* **324**, 179–185 (2012).

[42] Norton, J. A., Moley, J. F., Green, M. V., Carson, R. E. & Morrison, S. D. Parabiotic transfer of cancer anorexia/cachexia in male rats. *Cancer Research* **45**, 5547–5552 (1985).

[43] Arthur, S. T. *et al.* Cachexia among US cancer patients. *Journal of Medical Economics* **19**, 874–880 (2016).

[44] Rohm, M., Zeigerer, A., Machado, J. & Herzig, S. Energy metabolism in cachexia. *EMBO reports* **20** (2019).

[45] Stewart, G. D., Skipworth, R. J. & Fearon, K. C. Cancer cachexia and fatigue. *Clinical Medicine Journal* **6**, 140–143 (2006).

[46] Argilés, J. M., Busquets, S., Stemmler, B. & López-Soriano, F. J. Cancer cachexia: understanding the molecular basis. *Nature Reviews Cancer* **14**, 754–762 (2014).

[47] Porporato, P. E. Understanding cachexia as a cancer metabolism syndrome. *Oncogenesis* **5**, e200–e200 (2016).

[48] Shyh-Chang, N. Metabolic changes during cancer cachexia pathogenesis. In *Translational Research in Breast Cancer*, 233–249 (Springer Singapore, 2017).

[49] Fearon, K. C., Glass, D. J. & Guttridge, D. C. Cancer cachexia: Mediators, signaling, and metabolic pathways. *Cell Metabolism* **16**, 153–166 (2012).

[50] Argilés, J. M., López-Soriano, F. J. & Busquets, S. Mediators of cachexia in cancer patients. *Nutrition* **66**, 11–15 (2019).

[51] Argilés, J. M., Stemmler, B., López-Soriano, F. J. & Busquets, S. Nonmuscle tissues contribution to cancer cachexia. *Mediators of Inflammation* **2015**, 1–9 (2015).

[52] Cui, P. *et al.* Metabolic profiling of tumors, sera, and skeletal muscles from an orthotopic murine model of gastric cancer associated-cachexia. *Journal of Proteome Research* **18**, 1880–1892 (2019).

[53] Martin, A. & Freyssenet, D. Phenotypic features of cancer cachexia-related loss of skeletal muscle mass and function: lessons from human and animal studies. *Journal of Cachexia, Sarcopenia and Muscle* **12**, 252–273 (2021).

[54] Singh, J., Grigor, M. R. & Thompson, M. P. Glucose homeostasis in rats bearing a transplantable sarcoma. *Cancer Research* **40**, 1699–1706 (1980).

[55] Puig-Vilanova, E. *et al.* Oxidative stress, redox signaling pathways, and autophagy in cachectic muscles of male patients with advanced COPD and lung cancer. *Free Radical Biology and Medicine* **79**, 91–108 (2015).

[56] Mendell, J. R. & Engel, W. K. The fine structure of type II muscle fiber atrophy. *Neurology* **21**, 358–358 (1971).

[57] Zhang, Y. *et al.* The autophagic-lysosomal and ubiquitin proteasome systems are simultaneously activated in the skeletal muscle of gastric cancer patients with cachexia. *The American Journal of Clinical Nutrition* **111**, 570–579 (2020).

[58] TZIKA, A. A. *et al.* Skeletal muscle mitochondrial uncoupling in a murine cancer cachexia model. *International Journal of Oncology* **43**, 886–894 (2013).

[59] Poliaková, M., Aebersold, D. M., Zimmer, Y. & Medová, M. The relevance of tyrosine kinase inhibitors for global metabolic pathways in cancer. *Molecular Cancer* **17** (2018).

[60] Griguolo, G., Pascual, T., Dieci, M. V., Guarneri, V. & Prat, A. Interaction of host immunity with HER2-targeted treatment and tumor heterogeneity in HER2-positive breast cancer. *Journal for ImmunoTherapy of Cancer* **7** (2019).

[61] Alvarez-Calderon, F. *et al.* Tyrosine kinase inhibition in leukemia induces an altered metabolic state sensitive to mitochondrial perturbations. *Clinical Cancer Research* **21**, 1360–1372 (2014).

[62] Chen, R. *et al.* Disrupting glutamine metabolic pathways to sensitize gemcitabine-resistant pancreatic cancer. *Scientific Reports* **7** (2017).

[63] Shi, Y. *et al.* Integration of metabolomics and transcriptomics to reveal metabolic characteristics and key targets associated with cisplatin resistance in nonsmall cell lung cancer. *Journal of Proteome Research* **18**, 3259–3267 (2019).

[64] van Gastel, N. *et al.* Induction of a timed metabolic collapse to overcome cancer chemoresistance. *Cell Metabolism* **32**, 391–403.e6 (2020).

[65] Nicolantonio, F. D. *et al.* Precision oncology in metastatic colorectal cancer — from biology to medicine. *Nature Reviews Clinical Oncology* **18**, 506–525 (2021).

[66] Akiyama, T., Sudo, C., Ogawara, H., Toyoshima, K. & Yamamoto, T. The product of the human c-erbB-2 gene: a 185-kilodalton glycoprotein with tyrosine kinase activity. *Science* **232**, 1644–1646 (1986).

[67] Necela, B. M. *et al.* The antineoplastic drug, trastuzumab, dysregulates metabolism in iPSC-derived cardiomyocytes. *Clinical and Translational Medicine* **6** (2017).

[68] Maadi, H., Soheilifar, M. H., Choi, W.-S., Moshtaghian, A. & Wang, Z. Trastuzumab mechanism of action 20 years of research to unravel a dilemma. *Cancers* **13**, 3540 (2021).

[69] Kanehisa, M., Furumichi, M., Sato, Y., Ishiguro-Watanabe, M. & Tanabe, M. KEGG: integrating viruses and cellular organisms. *Nucleic Acids Research* **49**, D545–D551 (2020).

[70] Hudziak, R. M. *et al.* p185her2 monoclonal antibody has antiproliferative effects in vitro and sensitizes human breast tumor cells to tumor necrosis factor. *Molecular and Cellular Biology* **9**, 1165–1172 (1989).

[71] Carter, P. *et al.* Humanization of an anti-p185her2 antibody for human cancer therapy. *Proceedings of the National Academy of Sciences of the United States of America* **89**, 4285–4289 (1992).

[72] Slamon, D. J. *et al.* Use of chemotherapy plus a monoclonal antibody against HER2 for metastatic breast cancer that overexpresses HER2. *The New England Journal of Medicine* **344**, 783–792 (2001).

[73] Bang, Y.-J. *et al.* Trastuzumab in combination with chemotherapy versus chemotherapy alone for treatment of HER2-positive advanced gastric or gastro-oesophageal junction cancer (ToGA): a phase 3, open-label, randomised controlled trial. *The Lancet* **376**, 687–697 (2010).

[74] Krishnamurti, U. & Silverman, J. F. HER2 in breast cancer. *Advances In Anatomic Pathology* **21**, 100–107 (2014).

[75] Zhang, W., Tian, H. & hong Yang, S. The efficacy of neoadjuvant chemotherapy for HER-2-positive locally advanced breast cancer and survival analysis. *Analytical Cellular Pathology* **2017**, 1–5 (2017).

[76] Gomez-Martin, C. *et al.* Level of HER2 gene amplification predicts response and overall survival in HER2-positive advanced gastric cancer treated with trastuzumab. *Journal of Clinical Oncology* **31**, 4445–4452 (2013).

[77] Wang, Y. *et al.* GLUL promotes cell proliferation in breast cancer. *Journal of Cellular Biochemistry* **118**, 2018–2025 (2017).

[78] Miolo, G. *et al.* Pharmacometabolomics study identifies circulating spermidine and tryptophan as potential biomarkers associated with the complete pathological response to trastuzumab-paclitaxel neoadjuvant therapy in HER-2 positive breast cancer. *Oncotarget* **7**, 39809–39822 (2016).

[79] Nakamura, Y., Kawazoe, A., Lordick, F., Janjigian, Y. Y. & Shitara, K. Biomarker-targeted therapies for advanced-stage gastric and gastro-oesophageal junction cancers: an emerging paradigm. *Nature Reviews Clinical Oncology* **18**, 473–487 (2021).

[80] Garassino, M. C. *et al.* Durvalumab as third-line or later treatment for advanced non-small-cell lung cancer (ATLANTIC): an open-label, single-arm, phase 2 study. *The Lancet Oncology* **19**, 521–536 (2018).

[81] Rochfort, S. Metabolomics reviewed: A new omics platform technology for systems biology and implications for natural products research. *Journal of Natural Products* **68**, 1813–1820 (2005).

[82] Maia, M., Figueiredo, A., Cordeiro, C. & Silva, M. S. FT-ICR-MS-based metabolomics: A deep dive into plant metabolism. *Mass Spectrometry Reviews* (2021).

[83] Wishart, D. S. *et al.* HMDB: the human metabolome database. *Nucleic Acids Research* **35**, D521–D526 (2007).

[84] Alexandrov, T. Spatial metabolomics and imaging mass spectrometry in the age of artificial intelligence. *Annual Review of Biomedical Data Science* **3**, 61–87 (2020).

[85] Norris, J. L. & Caprioli, R. M. Analysis of tissue specimens by matrix-assisted laser desorption/ionization imaging mass spectrometry in biological and clinical research. *Chemical Reviews* **113**, 2309–2342 (2013).

[86] Sailwal, M. *et al.* Connecting the dots: Advances in modern metabolomics and its application in yeast system. *Biotechnology Advances* **44**, 107616 (2020).

[87] Fenn, J. B., Mann, M., Meng, C. K., Wong, S. F. & Whitehouse, C. M. Electrospray ionization for mass spectrometry of large biomolecules. *Science* **246**, 64–71 (1989).

[88] Karas, M. & Hillenkamp, F. Laser desorption ionization of proteins with molecular masses exceeding 10,000 daltons. *Analytical Chemistry* **60**, 2299–2301 (1988).

[89] Freiwald, A. & Sauer, S. Phylogenetic classification and identification of bacteria by mass spectrometry. *Nature Protocols* **4**, 732–742 (2009).

[90] Spraker, J. E., Luu, G. T. & Sanchez, L. M. Imaging mass spectrometry for natural products discovery: a review of ionization methods. *Natural Product Reports* **37**, 150–162 (2020).

[91] Janda, M. *et al.* Determination of abundant metabolite matrix adducts illuminates the dark metabolome of MALDI-mass spectrometry imaging datasets. *Analytical Chemistry* **93**, 8399–8407 (2021).

[92] Weaver, E. M. & Hummon, A. B. Imaging mass spectrometry: From tissue sections to cell cultures. *Advanced Drug Delivery Reviews* **65**, 1039–1055 (2013).

[93] Neumann, E. K., Djambazova, K. V., Caprioli, R. M. & Spraggins, J. M. Multimodal imaging mass spectrometry: Next generation molecular mapping in biology and medicine. *Journal of the American Society for Mass Spectrometry* **31**, 2401–2415 (2020).

[94] Aichler, M. & Walch, A. MALDI imaging mass spectrometry: current frontiers and perspectives in pathology research and practice. *Laboratory Investigation* **95**, 422–431 (2015).

[95] Buck, A. *et al.* High-resolution MALDI-FT-ICR MS imaging for the analysis of metabolites from formalin-fixed, paraffin-embedded clinical tissue samples. *The Journal of Pathology* **237**, 123–132 (2015).

[96] Goldman, R. *et al.* Smoking increases carcinogenic polycyclic aromatic hydrocarbons in human lung tissue. *Cancer research* **61**, 6367–6371 (2001).

[97] Lodovici, M., Akpan, V., Giovannini, L., Migliani, F. & Dolara, P. Benzo[a]pyrene diol-epoxide DNA adducts and levels of polycyclic aromatic hydrocarbons in autoptic samples from human lungs. *Chemico-Biological Interactions* **116**, 199–212 (1998).

[98] Castellanos-Garcia, L. J., Sikora, K. N., Doungchawee, J. & Vachet, R. W. LA-ICP-MS and MALDI-MS image registration for correlating nanomaterial biodistributions and their biochemical effects. *The Analyst* (2021).

[99] Lu, S. *et al.* Comparison of biomarker modalities for predicting response to PD-1/PD-l1 checkpoint blockade. *JAMA Oncology* **5**, 1195 (2019).

[100] Vargas, A. J. & Harris, C. C. Biomarker development in the precision medicine era: lung cancer as a case study. *Nature Reviews Cancer* **16**, 525–537 (2016).

[101] Sadek, J. *et al.* Pharmacological or genetic inhibition of iNOS prevents cachexia-mediated muscle wasting and its associated metabolism defects. *EMBO Molecular Medicine* **13** (2021).

[102] Rao, A., Barkley, D., França, G. S. & Yanai, I. Exploring tissue architecture using spatial transcriptomics. *Nature* **596**, 211–220 (2021).

[103] Zhao, T. *et al.* Spatial genomics enables multi-modal study of clonal heterogeneity in tissues. *Nature* **601**, 85–91 (2021).

Appendix

A.1. Conference contributions

Oral presentations:

1. **Kunzke T**, Sun N, Sbiera S, Wild V, Aichler M, Ronchi C, Schlegel N, Rosenwald A, Fassnacht M, Walch A, Kroiss M. High resolution tissue mass spectrometry imaging: a new tool for identification of prognostic markers in adrenocortical carcinoma. (2017) 19th European Congress of Endocrinology, Lisbon, Portugal.

2. Ludwig P*, **Kunzke T***, Rhayem Y, Feuchtinger A, Heinrich D, Woischke C, Williams TA, Kirchner T, Hahner S, Knösel T, Reincke M, Walch A, Beuschlein F. Image Analysis of Morphometric Parameters in Aldosterone-Producing Adenomas. (2017) Progress in Primary Aldosteronism 5, Munich, Germany.

   *) Both authors presented the talk

3. **Kunzke T**, Buck A, Prade VM, Feuchtinger A, Prokopchuk O, Martignoni ME, Heisz S, Hauner H, Janssen KP, Walch A, Aichler M. Derangements of amino acids in cachectic skeletal muscle are caused by mitochondrial dysfunction. (2019) 12th international SCWD Conference On Cachexia, Sarcopenia And Muscle Wasting, Berlin, Germany. **Young Investigators Award Finalist**

Poster presentations:

1. **Kunzke T**, Buck A, Prade VM, Feuchtinger A, Prokopchuk O, Martignoni ME, Heisz S, Hauner H, Janssen KP, Walch A, Aichler M. Derangements of amino acids in cachectic skeletal muscle are caused by mitochondrial dysfunction. (2019) OurCon VII, Saint-Malo, France.

2. **Kunzke T**, Buck A, Prade VM, Feuchtinger A, Prokopchuk O, Martignoni ME, Heisz S, Hauner H, Janssen KP, Walch A, Aichler M. Derangements of amino acids in cachectic skeletal muscle are caused by mitochondrial dysfunction. (2019) 12th international SCWD Conference On Cachexia, Sarcopenia And Muscle Wasting, Berlin, Germany.

A.2. Approval letters from publishers

Figure A.1.   Approval letter for the publication in the Journal *Laboratory Investigation*. The article was reproduced with permission from Springer Nature. [1]

Please note that the remaining first author publications embedded in this dissertation are licensed under the Creative Commons Attribution 4.0 International License (CC BY-NC-ND 4.0 [2], or CC BY-NC 4.0 [4]) and thus do not require any further permission to be used in this cumulative dissertation.

Figure A.2. Approval letter for the publication in the Journal *Cancer Research* [3]

Acknowledgments

First of all, I want to thank my PhD supervisor Prof. Gil Westmeyer for giving me the unique opportunity to work on these exciting and challenging topics during my PhD. I thank him for his help in all matters as well as the opened new perspective on exciting topics.

Furthermore, I would like to thank my mentor, Prof. Axel Walch. I always enjoyed the scientific discussions with him very much. He gave me extraordinary freedom and confidence to develop my ideas, which presented many challenges but ultimately made me a scientist.

I would also like to thank Prof. Bernd Reif, who provided valuable suggestions as a member of my dissertation committee.

In general, I would like to thank my great colleagues with whom I have shared my daily life over the years. You have added a lot to my PhD work, and many have become good friends. Dr. Achim Buck and Dr. Na Sun were essential pioneers in helping me learn the methodology and develop crucial ideas. I owe my bioinformatics progress and endlessly creative scientific exchange to Dr. Verena Marina Prade. Dr. Katharina Huber and Dr. Christian Greunke were important persons not to forget the joy of work and to improve my LaTeX skills. I would also like to thank Dr. Annette Feuchtinger, who always provided me with resources from her bustling Core Facility. Not to forget the participation of Claudia-Mareike Pflüger, Ulrike Buchholz, Elenore Samson, Gabriele Mettenleiter, and Cristina Hübner Freitas in many funny moments and valuable technical support. I would also like to thank the unique Andreas Voss for his technological know-how. I want to thank Dr. Michaela Aichler for electron microscopy and helpful ideas and suggestions. To my fellow PhD students Jun Wang, Qian Wang, Jian Shen, Lisa Kreutzer, and Marco Matzka, I owe a hilarious working atmosphere and a lot of joy in my work. Last but not least, I would like to mention my students, who enriched the daily routine decisively and made a valuable contribution to the work: Fabian Hölzl, Adrian Knoll, and Barbara Stöckl.

Acknowledgments

I want to thank all my great friends for their support in this challenging time. Primarily I want to name here Daniel and Manuel.

Above all, however, I would like to thank my family for supporting me unconditionally throughout my life and during this PhD. My parents, Without you, I would not be the person I am today, and for that, I would like to thank you from the bottom of my heart.